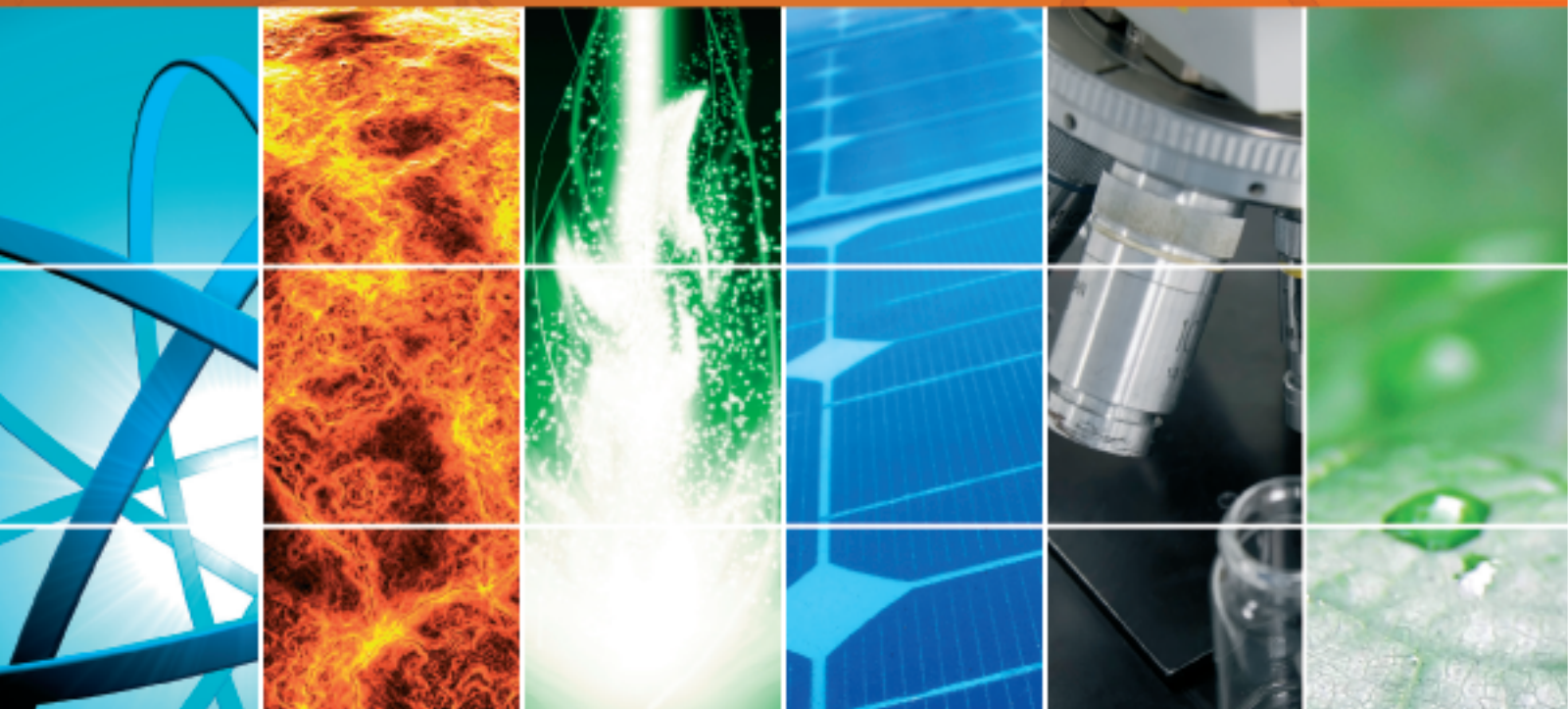


International Journal of Photoenergy

Photocatalysis and Photoelectrochemistry for Solar Fuels

Guest Editors: Zhigang Zou, Jinhua Ye, Michael R. Hoffmann,
and Wenjun Luo





Photocatalysis and Photoelectrochemistry for Solar Fuels

International Journal of Photoenergy

Photocatalysis and Photoelectrochemistry for Solar Fuels

Guest Editors: Zhigang Zou, Jinhua Ye, Michael R. Hoffmann,
and Wenjun Luo



Copyright © 2014 Hindawi Publishing Corporation. All rights reserved.

This is a special issue published in "International Journal of Photoenergy." All articles are open access articles distributed under the Creative Commons Attribution License, which permits unrestricted use, distribution, and reproduction in any medium, provided the original work is properly cited.

Editorial Board

- M. S. A. Abdel-Mottaleb, Egypt
Xavier Allonas, France
Nicolas Alonso-Vante, France
Wayne A. Anderson, USA
Yanhui Ao, China
Raja S. Ashraf, UK
V. Augugliaro, Italy
Detlef W. Bahnemann, Germany
I. R. Bellobono, Italy
Raghu N. Bhattacharya, USA
Pramod H. Borse, India
Alessio Bosio, Italy
Stephan Buecheler, Switzerland
Gion Calzaferri, Switzerland
C. Chen, China
Sung Oh Cho, Republic of Korea
V. Cimrová, Czech Republic
Juan M. Coronado, Spain
Ying Dai, China
D. D. Dionysiou, USA
Pingwu Du, China
M. M. El-Nahass, Egypt
Polycarpos Falaras, Greece
Chris Ferekides, USA
Paolo Fornasiero, Italy
Hermenegildo García, Spain
Germà Garcia-Belmonte, Spain
E. I. Garcia-Lopez, Italy
Beverley Glass, Australia
M. A. Gondal, Saudi Arabia
Jr-Hau He, Taiwan
Shinya Higashimoto, Japan
Cheuk-Lam Ho, Hong Kong
Wing-Kei Ho, Hong Kong
Fuqiang Huang, China
Adel A. Ismail, Egypt
Chun-Sheng Jiang, USA
Misook Kang, Republic of Korea
Shahed Khan, USA
Sun-Jae Kim, Republic of Korea
Jong Hak Kim, Republic of Korea
Sungjee Kim, Republic of Korea
Cooper H. Langford, Canada
Tae-Woo Lee, Republic of Korea
Lecheng Lei, China
Xinjun Li, China
Zhaosheng Li, China
Yuexiang Li, China
Stefan Lis, Poland
Vittorio Loddo, Italy
Gongxuan Lu, China
Dongge Ma, China
N. M. Mahmoodi, Iran
Nai Ki Mak, Hong Kong
Rajaram S. Mane, India
D. Mantzavinos, Greece
Ugo Mazzucato, Italy
Sheng Meng, China
Jacek Miller, Poland
Claudio Minero, Italy
Antoni Morawski, Poland
Franca Morazzoni, Italy
F. Morlet-Savary, France
M. Muneer, India
Kun Na, Republic of Korea
Ebinazar B. Namdas, Australia
Maria Neves, Portugal
Tebello Nyokong, South Africa
Kei Ohkubo, Japan
Haridas Pal, India
Leonidas Palilis, Greece
Leonardo Palmisano, Italy
Ravindra K. Pandey, USA
H. Park, Republic of Korea
Pierre Pichat, France
Gianluca Li Puma, UK
Tijana Rajh, USA
Peter Robertson, UK
Avigdor Scherz, Israel
Elena Selli, Italy
Ganesh D. Sharma, India
Jinn Kong Sheu, Taiwan
Panagiotis Smirniotis, USA
Zofia Stasicka, Poland
Elias Stathatos, Greece
J. Subbiah, Australia
M. Swaminathan, India
Kazuhiro Takanabe, Saudi Arabia
Mohamad-Ali Tehfe, Canada
K. R. Justin Thomas, India
Yang Tian, China
Nikolai V. Tkachenko, Finland
Ahmad Umar, Saudi Arabia
Thomas Unold, Germany
Veronica Vaida, USA
Roel van De Krol, Germany
Mark van Der Auweraer, Belgium
Rienk Van Grondelle, The Netherlands
Wilfried Van Sark, The Netherlands
Sheng Wang, China
Xuxu Wang, China
Mingkui Wang, China
Ezequiel Wolcan, Argentina
Man Shing Wong, Hong Kong
David Worrall, UK
Jeffrey C. S. Wu, Taiwan
Yanfa Yan, USA
Jiannian Yao, China
Minjoong Yoon, Republic of Korea
Jiangbo Yu, USA
Hongtao Yu, USA
Ying Yu, China
Klaas Zachariasse, Germany
Juan Antonio Zapien, Hong Kong
Tianyou Zhai, China
Lizhi Zhang, China
Guijiang Zhou, China
Yong Zhou, China
Rui Zhu, China

Contents

Photocatalysis and Photoelectrochemistry for Solar Fuels, Zhigang Zou, Jinhua Ye, Michael R. Hoffmann, and Wenjun Luo

Volume 2014, Article ID 894396, 2 pages

Surfactant-Free Synthesis of Single Crystalline SnS₂ and Effect of Surface Atomic Structure on the Photocatalytic Property, Zhigang Zou, Jinhua Ye, Michael R. Hoffmann, and Wenjun Luo

Volume 2014, Article ID 894396, 2 pages

Structure, Optical Properties, and Photocatalytic Activity towards H₂ Generation and CO₂ Reduction of GaN Nanowires via Vapor-Liquid-Solid Process, Hong Pang, Lequan Liu, Shuxin Ouyang, Hua Xu, Yunxiang Li, and Defa Wang

Volume 2014, Article ID 894396, 6 pages

Preparation of Cerium Modified Titanium Dioxide Nanoparticles and Investigation of Their Visible Light Photocatalytic Performance, Jinfeng Liu, Haiyan Li, Qiuye Li, Xiaodong Wang, Min Zhang, and Jianjun Yang

Volume 2014, Article ID 695679, 9 pages

Bottom-Up Enhancement of g-C₃N₄ Photocatalytic H₂ Evolution Utilising Disordering Intermolecular Interactions of Precursor, Xue Lu Wang, Wen Qi Fang, Yu Hang Li, Pengfei Liu, Haimin Zhang, Yun Wang, Porun Liu, Yefeng Yao, Huijun Zhao, and Hua Gui Yang

Volume 2014, Article ID 149520, 8 pages

Visible-Light Degradation of Dyes and Phenols over Mesoporous Titania Prepared by Using Anthocyanin from Red Radish as Template, Zhiying Yan, Wenjuan Gong, Yongjuan Chen, Deliang Duan, Junjie Li, Wei Wang, and Jiaqiang Wang

Volume 2014, Article ID 968298, 10 pages

Band-Gap Engineering of NaNbO₃ for Photocatalytic H₂ Evolution with Visible Light, Peng Li, Hideki Abe, and Jinhua Ye

Volume 2014, Article ID 380421, 6 pages

Sensitization of Perovskite Strontium Stannate SrSnO₃ towards Visible-Light Absorption by Doping, Hungru Chen and Naoto Umezawa

Volume 2014, Article ID 643532, 3 pages

Development of Thin Film Amorphous Silicon Tandem Junction Based Photocathodes Providing High Open-Circuit Voltages for Hydrogen Production, F. Urbain, K. Wilken, V. Smirnov, O. Astakhov, A. Lambert, J.-P. Becker, U. Rau, J. Ziegler, B. Kaiser, W. Jaegermann, and F. Finger

Volume 2014, Article ID 249317, 10 pages

Editorial

Photocatalysis and Photoelectrochemistry for Solar Fuels

Zhigang Zou,¹ Jinhua Ye,² Michael R. Hoffmann,³ and Wenjun Luo¹

¹Department of Physics, Ecomaterials and Renewable Energy Research Center (ERERC), Nanjing University, Nanjing 210093, China

²International Center for Materials Nanoarchitectonics (MANA), National Institute for Materials Science (NIMS), Tsukuba 3050044, Japan

³Linde-Robinson Laboratories, California Institute of Technology, Pasadena, CA 91125, USA

Correspondence should be addressed to Zhigang Zou; zgrou@nju.edu.cn

Received 21 October 2014; Accepted 21 October 2014; Published 1 December 2014

Copyright © 2014 Zhigang Zou et al. This is an open access article distributed under the Creative Commons Attribution License, which permits unrestricted use, distribution, and reproduction in any medium, provided the original work is properly cited.

The Sun generates enough energy to power the Earth. However, solar energy should be stored into chemical energy to be conveniently used due to its low energy density and discontinuous radiation. In the last several years, photocatalysis and photoelectrochemistry for solar fuels have reattracted more and more governments' and people's interest from all over the world and become a very hot topic. If we utilize the abundant solar energy to convert CO₂ into hydrocarbon fuels especially, it would address the problems of global climate change and solar energy storage at the same time. Recently, different new materials and ideas have been proposed and steady scientific progress has been done. However, it is still a key challenge to explore visible-light responsive materials with high photocatalytic activities. The special issue contains eight papers, where 6 papers are related to visible-light activity and 2 papers are related to UV activity.

In a paper entitled "*Development of thin film amorphous silicon tandem junction based photocathodes providing high open-circuit voltages for hydrogen production*" by F. Urbain et al., they prepare the a-Si:H/a-Si:H based photocathodes, which exhibit a high photocurrent onset potential of 1.76 V versus the reversible hydrogen electrode (RHE) and a photocurrent of 5.3 mA/cm² at 0 V versus RHE. They provide an efficient and low-cost route to solar hydrogen production.

In a paper entitled "*Bottom-up enhancement of g-C₃N₄ photocatalytic H₂ evolution utilising disordering intermolecular interactions of precursor*" by X. L. Wang et al., they develop a bottom-up strategy to synthesize g-C₃N₄ photocatalysts with improved optical property and chemical structure through using disordered dicyandiamide (D-DCDA) as reaction precursor. The carbon nitride sample condensed

by D-DCDA indicates higher photocatalytic activity for hydrogen evolution due to looser structure and more effective light harvesting and charge separation efficiency.

In a paper entitled "*Structure, optical properties, and photocatalytic activities towards H₂ generation and CO₂ reduction of GaN nanowires via vapor-liquid-solid process*" by H. Pang et al., they synthesize high quality single crystalline GaN nanowires with large aspect ratio on n-type Si (111) substrate via the Au-catalyzed vapor-liquid-solid process. Photocatalytic H₂ evolution and CO₂ reduction over the as-prepared GaN nanowires are also investigated. Their results suggest that the GaN nanowires greatly enhanced capability compared to the GaN powders.

In a paper entitled "*Band-gap engineering of NaNbO₃ for photocatalytic H₂ evolution with visible light*" by P. Li et al., they shift the photoabsorption edge of NaNbO₃ to the visible-light region by La and Co codoping. Moreover, H₂ is successfully generated over the doped NaNbO₃ samples under visible-light irradiation. Density-functional theory calculations show that Co-induced impurity states are formed in the band gap of NaNbO₃, which is considered to be the origin of visible-light absorption upon the doped NaNbO₃ sample.

In a paper entitled "*Sensitization of perovskite strontium stannate SrSnO₃ towards visible-light absorption by doping*" by H. Chen and N. Umezawa, they calculate electronic structures of SrSnO₃ after Cr³⁺, Fe³⁺, and Rh³⁺ and anions N³⁻, N²⁻, and S²⁻ doping. Among all considered cation dopants, Rh³⁺ gives rise to the deep in gap states. The transition from Rh³⁺ to SrSnO₃ conduction band is 0.89 eV lower than the band gap.

In a paper entitled “*Surfactant-free synthesis of single crystalline SnS₂ and effect of surface atomic structure on the photocatalytic property*” by M. Li et al., they prepare sheet like tin disulfide SnS₂ single crystal exposed with well-defined {001} facets and flowerlike SnS₂ mainly exposed with {010} facets through a surfactant-free solvothermal process. The sheet like SnS₂ showed a much higher photocatalytic activity in degradation of methyl orange than flowerlike SnS₂. Theoretical and experimental results reveal that the band structure derived from the surface atomic structure played a more important role than the surface energy in the photocatalytic property.

In a paper entitled “*Preparation of cerium modified titanium dioxide nanoparticles and investigation of their visible light photocatalytic performance*” by J. Liu et al., they prepare CeO_x/TiO₂ by the hydrothermal-calcination method. The Ce ions have the two valence states, Ce³⁺ and Ce⁴⁺, which can act as the electron acceptor to improve the separation efficiency of the photogenerated electron-hole pairs.

In a paper entitled “*Visible-light degradation of dyes and phenols over mesoporous titania prepared by using anthocyanin from red radish as template*” by Z. Yan et al., they prepare highly crystalline mesoporous titania by using a natural pigment from red radish as template. The prepared mesoporous titania photocatalyst exhibited significant activity under visible-light irradiation for the degradation of dyes and phenols due to its red shift of band-gap-absorption onset and visible-light response as a result of the incorporation of surface carbon species.

Acknowledgment

We would like to thank all of the authors and the reviewers for their contributions to this special issue.

Zhigang Zou
Jinhua Ye
Michael R. Hoffmann
Wenjun Luo

Research Article

Surfactant-Free Synthesis of Single Crystalline SnS₂ and Effect of Surface Atomic Structure on the Photocatalytic Property

Mengyi Li,¹ Enzuo Liu,^{1,2} Huilin Hu,¹ Shuxin Ouyang,^{1,2} Hua Xu,^{1,2} and Defa Wang^{1,2}

¹ TU-NIMS Joint Research Center and Tianjin Key Laboratory of Composite and Functional Materials, School of Materials Science and Engineering, Tianjin University, 92 Weijin Road, Nankai District, Tianjin 300072, China

² Collaborative Innovation Center of Chemical Science and Engineering, 92 Weijin Road, Nankai District, Tianjin 300072, China

Correspondence should be addressed to Defa Wang; defawang@tju.edu.cn

Received 14 July 2014; Accepted 8 September 2014; Published 1 December 2014

Academic Editor: Wenjun Luo

Copyright © 2014 Mengyi Li et al. This is an open access article distributed under the Creative Commons Attribution License, which permits unrestricted use, distribution, and reproduction in any medium, provided the original work is properly cited.

Sheetlike tin disulfide (SnS₂) single crystal exposed with well-defined {001} facets and flowerlike SnS₂ mainly exposed with {010} facets were prepared through a surfactant-free solvothermal process. Photocatalytic degradation of methyl orange (MO) under visible light irradiation indicated that the sheetlike SnS₂ showed a much higher activity than flowerlike SnS₂. Theoretical and experimental results revealed that the band structure derived from the surface atomic structure played a more important role than the surface energy in the photocatalytic property. The present work has provided a deep insight into the important role of the surface energy and band structure, both of which are derived from the surface atomic structure, in the photocatalytic activity.

1. Introduction

As an ideal green chemistry technology, semiconductor photocatalysis has been attracting extensive attention owing to its potential application in environment purification. The photocatalytic activity of a semiconductor is influenced by many factors, among which the surface atomic structure plays an important role. Generally speaking, the high energy facets that contain abundant unsaturated coordination atoms exhibit high reactivity [1–5]. For example, Yang et al. have found that the high energy {001} facets of anatase TiO₂ are much more reactive than the thermodynamically more stable low energy {010} facets [6]. Xi and Ye demonstrated that the well-defined BiVO₄ nanoplates with exposed {001} facets exhibited greatly enhanced activity for photocatalytic degradation of organic contaminants and for photocatalytic O₂ generation [7]. On the other hand, Pan et al. demonstrated that TiO₂ single crystal exposed with more {010} facets exhibited superior electronic band structure over that of TiO₂ exposed with more {001} facets, resulting in a higher photocatalytic activity [8]. Apparently, both the surface atomic geometry (atomic arrangement and coordination) and surface electronic structure play the crucial role in the photocatalytic activity of a semiconductor material.

Semiconducting metal sulfides are of an important kind of photocatalytic and photovoltaic materials. Among them, tin disulfide (SnS₂) has attracted considerable attention for applications in a variety of fields such as gas sensing [9], anode materials [10], and solar cell [11]. In addition to its low price, nontoxicity, and chemical stability in acidic or neutral solutions, hexagonal SnS₂ possesses a narrow band gap of 2.2–2.5 eV and has the potential to be a good visible-light photocatalyst [12–14]. Featured as a hexagonal CdI₂-type crystal structure consisting of S–Sn–S triple layer, in which the atomic layers are held together by weak van der Waals interactions, SnS₂ can be easily cleaved, allowing the formation of different morphologies [15]. To date, various SnS₂ morphologies, such as graphene-like [13], sphere-like [16], flower-like [17], nanotubes [18], nanoplates [19], nanobelts [20], and nanowires [21] structures, have been successfully fabricated by chemical bath, template methods, thermal decomposition, or hydrothermal methods and so on.

Herein we report for the first time a simple surfactant-free method for the preparation of sheetlike SnS₂ with exposed {001} facets and flowerlike SnS₂ with exposed {010} facets. Photocatalytic degradation of methyl orange (MO) under visible light irradiation indicated that the sheetlike SnS₂ showed a much higher activity than flowerlike SnS₂. Theoretical and

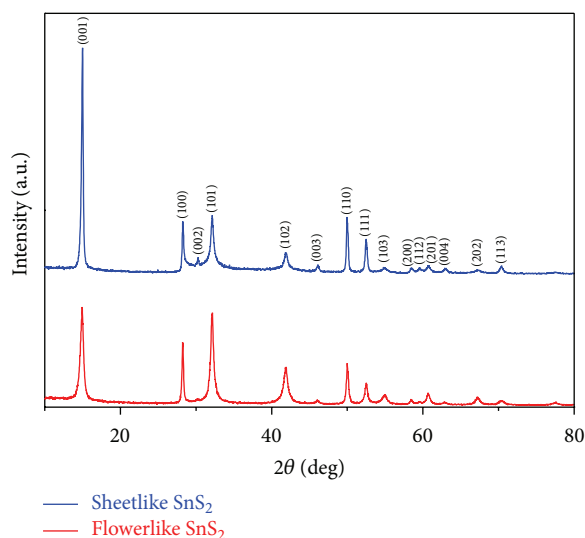


FIGURE 1: XRD patterns of the SnS_2 samples.

experimental results revealed that the band structure derived from the surface atomic structure played a more important role than the surface energy in the photocatalytic property.

2. Experimental

2.1. Photocatalyst Preparation. All reagents including tin chloride pentahydrate ($\text{SnCl}_4 \cdot 5\text{H}_2\text{O}$), concentrated hydrochloric acid, absolute alcohol, acetic acid, and thioacetamide (TAA) were analytical grade and used directly as received without further purification.

SnS_2 was prepared from $\text{SnCl}_4 \cdot 5\text{H}_2\text{O}$ (J&K) and TAA (J&K) via a solvothermal route. In a typical preparation, 5.0 mmol of $\text{SnCl}_4 \cdot 5\text{H}_2\text{O}$ was dissolved in 3 mL of concentrated hydrochloric acid (38%, w/w) in a 100 mL beaker. Then, 70 mL of deionized water and 12.5 mmol of TAA were added in sequence. After stirring, the reactants were transferred into a Teflon-line stainless steel autoclave of 100 mL capacity. The autoclave was sealed and heated at 180°C for 12 h and then cooled down to room temperature naturally. A yellow precipitate was collected and washed with deionized water and absolute ethanol for several times to remove the impurities. Finally, the sample was dried in vacuum at 60°C for 12 h to get the sheetlike SnS_2 . To synthesize the flowerlike SnS_2 , 5.0 mmol of $\text{SnCl}_4 \cdot 5\text{H}_2\text{O}$ was dissolved in 3 mL of acetic acid in a 100 mL beaker, and 70 mL of ethanol and 12.5 mmol of TAA were added in sequence. The following process was the same as that for sheetlike SnS_2 fabrication.

2.2. Characterization. Crystal structures of the as-prepared samples were determined by an X-ray diffractometer (XRD: D8 Advanced, Bruker, Germany) using $\text{Cu-K}\alpha$ radiation ($\lambda = 1.54178 \text{ \AA}$) at a scanning rate of $0.02^\circ \text{ s}^{-1}$. X-ray photoelectron spectroscopy (XPS) was performed on Thermo ESCALAB250 using monochromatized $\text{Al K}\alpha$ radiation as the exciting source, where the binding energies were calibrated by referencing the C 1s peak (284.6 eV). UV-vis diffuse reflectance

spectra were measured at room temperature in the range of 220–800 nm on a UV-vis spectrophotometer (UV-vis DRS UV-2700, Shimadzu, Japan) by using BaSO_4 as reference and were converted to absorbance spectra by the Kubelka-Munk method. The Brunauer-Emmett-Teller (BET) surface areas were measured by a surface area analyzer (BET-BJH AsiQcovoo 2–4, Quantachrom, USA). Microstructures of the samples were observed on a scanning electron microscope (SEM S4800, Hitachi, Japan) and a transmission electron microscope (TEM Technai G2 F20, FEI, Netherlands).

2.3. Photocatalytic Activity Evaluation. Photocatalytic activity was evaluated by performing methyl orange (MO) degradation as follows: 40 mg of the catalyst was suspended in 100 mL of aqueous solution (10 mg/L) in a Pyrex reactor. Before irradiation, the suspension was stirred in the dark for about 2 h to ensure an adsorption-desorption equilibrium. Then the reaction was initiated by irradiating with a 300 W Xenon lamp located 15 cm away from the solution. A cutoff filter (L42, Hoya, Japan) was equipped to remove UV light. At a certain given time interval, 3 mL of reaction solution was sampled and separated by filter. The absorption spectrum of the filtrate was measured by UV-vis spectrophotometer.

2.4. Theoretical Calculations. Electronic structures and surface atomic structures of the two SnS_2 samples were investigated via the projector augmented wave (PAW) formalism of density functional theory as implemented in the Vienna Ab initio Simulation Package (VASP) [22]. The exchange-correlation function is approximated with the local density approximation (LDA). The energy cutoff for plane-wave expansion of the PAW's is 400 eV. As will be discussed below, {001} and {010} surfaces are modeled by periodically repeated slabs containing 6 and 7 SnS_2 layers, respectively, and separated by a vacuum region of more than 15 \AA . The thickness of the slabs is determined when the energy of increased SnS_2 molecules with the thickness increasing approaches the energy of bulk SnS_2 . We use a two-dimensional unit cell containing 1 and 4 SnS_2 per SnS_2 layer. The Brillouin zone is sampled using Monkhorst-Pack scheme [23] with $15 \times 15 \times 1$ and $5 \times 7 \times 1$ K-point grid for {001} and {010} surfaces, respectively. For geometry optimization, all the internal coordinates are relaxed until the Hellmann-Feynman forces are less than 0.01 eV/ \AA .

3. Results and Discussion

XRD patterns of the as-prepared SnS_2 samples are shown in Figure 1. We can see that all the peaks in the XRD patterns can be readily indexed to hexagonal SnS_2 with lattice constants $a = 0.3648 \text{ nm}$ and $c = 0.5899 \text{ nm}$, which are in good agreement with the reported values (JCPDS file number 65-7657). No other impurity peaks were detected. Further analysis revealed that, for the sheetlike sample, the (001) diffraction peak showed the strongest intensity, indicating that the (001) orientation is predominant. For the flowerlike sample, the (001) diffraction peak remarkably decreased while the (101) peak relatively increased.

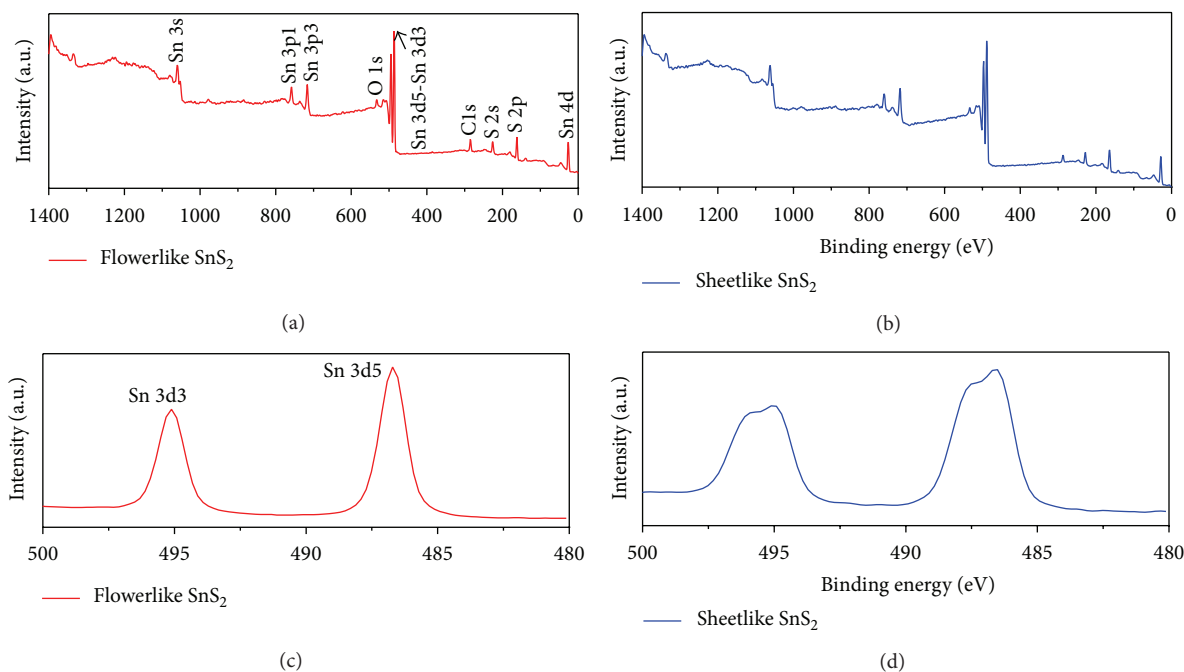


FIGURE 2: Wide range XPS survey profiles of the flowerlike SnS_2 (a) and sheetlike SnS_2 (b) and high-resolution spectra of Sn 3d in flowerlike SnS_2 (c) and sheetlike SnS_2 (d).

Meanwhile, the surface electronic states and the chemical composition of samples were detected by XPS. The survey spectra showed the presence of Sn, C, S, and O in both the sheetlike and flowerlike samples (see Figures 2(a) and 2(b)). The two strong peaks around 486.5 and 495 eV displayed in Figures 2(c) and 2(d) can be attributed to Sn $3d_{3/2}$ and $3d_{5/2}$, respectively, which are in good accordance with the characteristic peak of Sn(IV) [24]. No Sn^{2+} peak (binding energy at round 485.8 eV) was detected in the Sn 3d spectrum, indicating the formation of pure SnS_2 .

The size and morphology of the obtained samples were observed by SEM, TEM, and HRTEM. Figure 3(a) presents a typical SEM image of the sheetlike SnS_2 , which are 80–100 nm in width and 20–30 nm in thickness. TEM observation (Figure 3(b)) further confirmed the structural feature of the well-defined hexagonal plate, which was also verified by HRTEM (Figure 3(c)) analysis and the fast Fourier transformation pattern (FFT, Figure 3(c) inset). It indicates that the surface of nanosheet is mainly composed of {001} facet, being in good agreement with the XRD analysis. Figures 3(d) and 3(e) show the SEM and TEM images of flowerlike SnS_2 , respectively. We can see that each individual flower consists of a large number of nanosheets. Each individual leaf was well crystallized into the single crystalline, the characteristic of which was confirmed by HRTEM (Figure 3(f)) image and the FFT pattern (Figure 3(f) inset). The diffraction spots of the FFT pattern can be indexed as {002} and {100} planes, confirming that the main exposed facets of flowerlike SnS_2 are {010}.

It is known that, for a given crystal, each facet owns a unique surface atomic arrangement and thus a unique electronic configuration [25]. Therefore, a single crystal

exposed with different crystal facets will exhibit different electronic structures. To study the electronic band structures of SnS_2 samples, we measured both the UV-vis absorption spectra and the valence band XPS spectra. From the UV-vis diffuse reflectance spectra as shown in Figure 4(a) we obtained that the main absorption edges of sheetlike SnS_2 and flowerlike SnS_2 are nearly 550 nm and 600 nm, respectively. Correspondingly, the band gaps are calculated to be ~ 2.25 eV for sheetlike SnS_2 and ~ 2.05 eV for flowerlike SnS_2 , as shown by the plots of transformed Kubelka-Munk function versus the energy of photon (Figure 4(a), inset), being consistent with that of a previous study [26]. The valence band XPS spectra (Figure 4(b)) show that the VB edge of sheetlike SnS_2 is almost the same as that of flowerlike SnS_2 , implying that the different band gap energies of sheetlike and flowerlike SnS_2 are due to the different conduction band edges of these two SnS_2 samples: the CB edge of sheetlike SnS_2 is higher than that of flowerlike SnS_2 .

Based on the above experimental results, we can draw a scheme of the band structures of sheetlike SnS_2 and flowerlike SnS_2 as shown in Figure 5. Due to their different band structures, especially the conduction band edges, the sheetlike SnS_2 and flowerlike SnS_2 are expected to exhibit different photocatalytic properties.

Photocatalytic activity of the SnS_2 samples was evaluated by performing methyl orange (MO) degradation under visible light irradiation ($\lambda > 420$ nm). The characteristic absorption of MO at $\lambda = 464$ nm was used to monitor the photocatalytic degradation process. It is interesting to note from Figure 6 that although the specific surface area of flowerlike SnS_2 ($32.4 \text{ m}^2 \text{ g}^{-1}$) is nearly twice greater than that of the sheetlike SnS_2 ($17.5 \text{ m}^2 \text{ g}^{-1}$), its activity for MO degradation is

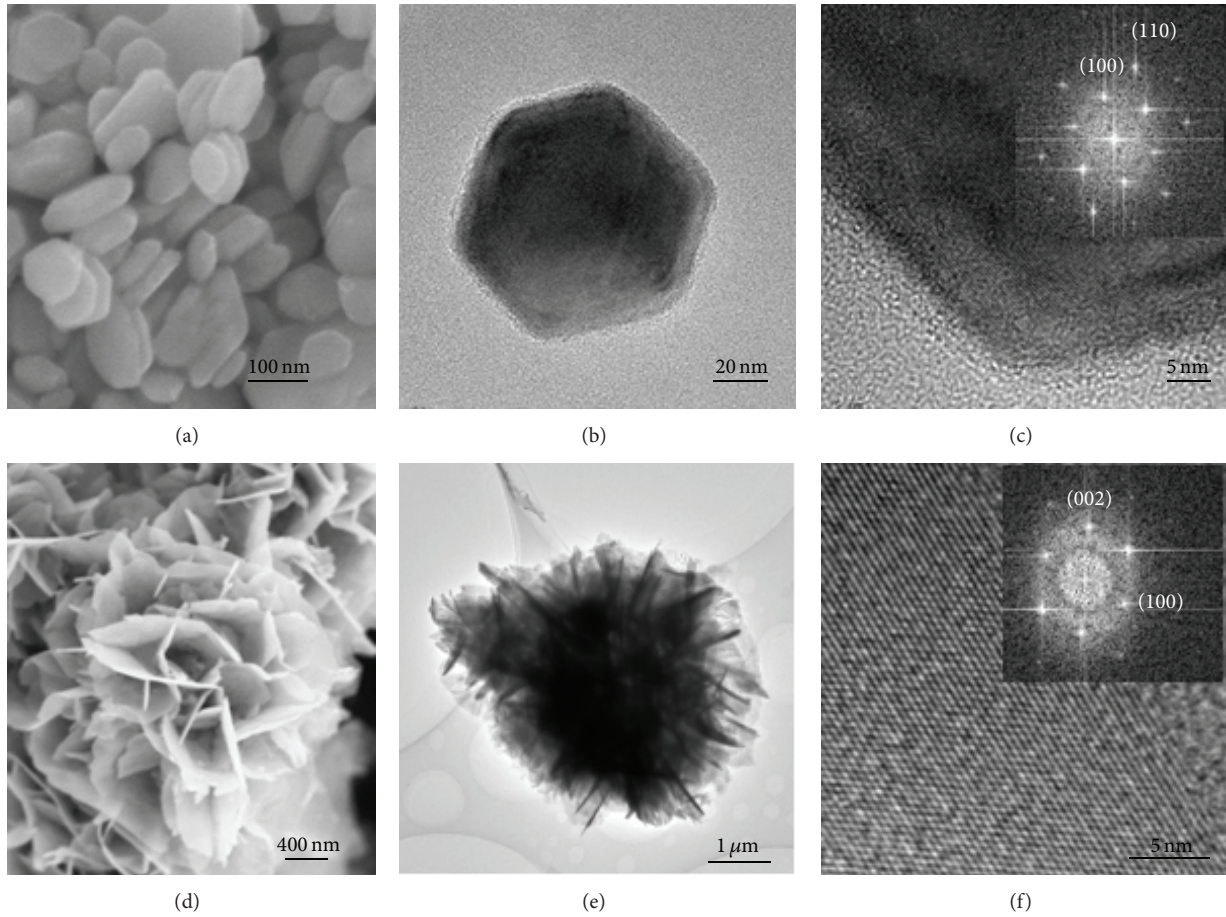


FIGURE 3: SEM, TEM, and HRTEM images of the sheetlike SnS_2 ((a)–(c)) and flowerlike SnS_2 ((d)–(f)). The inset in (c) and (f) is the fast Fourier transform patterns corresponding to the respective HRTEM images.

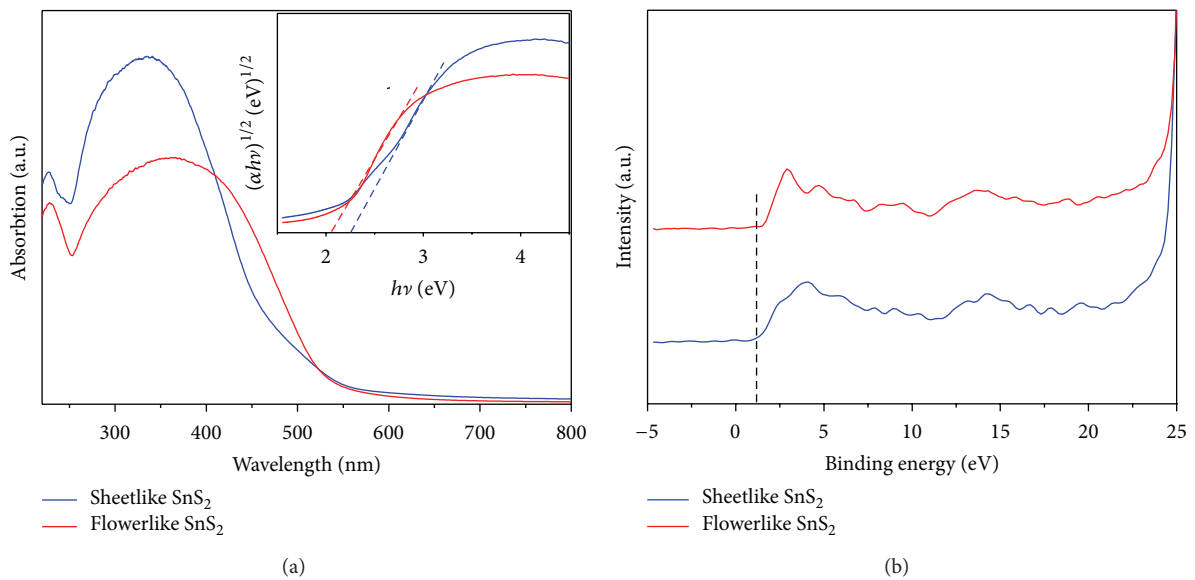


FIGURE 4: (a) UV-visible absorption spectra and corresponding plots of transformed Kubelka-Munk function versus the energy of photon (inset); (b) Valence-band XPS spectra of the two SnS_2 samples.

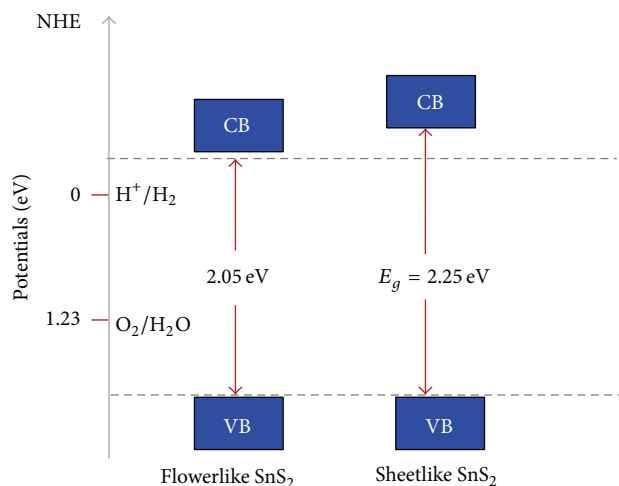


FIGURE 5: Schematic illustration of the electronic band structures of sheetlike and flowerlike SnS_2 samples.

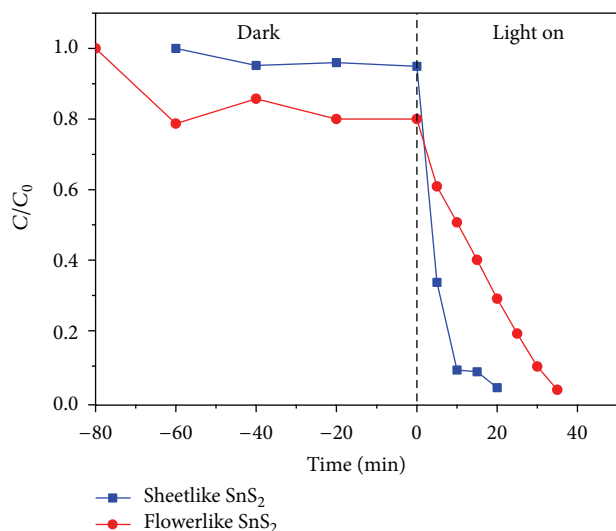


FIGURE 6: Variation of the MO concentration shows the photocatalytic degradation process over two photocatalysts (0.04 g) during dark and upon visible light irradiation ($\lambda > 420 \text{ nm}$).

substantially lower than that of the sheetlike one. The kinetics of the degradation were fitted to a pseudo first-order reaction: $\ln(C_0/C) = kt$, where k is the apparent rate constant [27]. The apparent rate constant of sheetlike SnS_2 (0.157 min^{-1}) is 2.6 times higher than that of flowerlike SnS_2 ($k = 0.06 \text{ min}^{-1}$). It suggests that the photocatalytic activity of SnS_2 is more directly related to its surface structure rather than its specific surface area. Since the SnS_2 of different morphologies possess different predominant facets, the surface atomic structure and thus electronic structure are supposed to play a more deciding role in the different activities.

In order to get further theoretical insight into the mechanism of how the surface atomic structure results in different photocatalytic activities of SnS_2 , we calculated the electronic structure and surface stability of sheetlike SnS_2 {001} (S001) and flowerlike SnS_2 {010} (S010) facets through the density

functional theory (DFT). In the slab models as illustrated in Figure 7(a), the {010} surface with different determinations is considered. The result shows that, compared to the {010} surface, the {001} surface owns lower surface energy (see Figure S1 in supporting information, available online at <http://dx.doi.org/10.1155/2014/394146>), meaning that the {001} facet is more stable than the {010} surface. As shown in Figure 7(b), energy band of S001, the conduction band minimum (CBM) of SnS_2 is located at M point of the Brillouin zone and the valence band maximum (VBM) is situated in the region between the K point and the Γ point. This means that SnS_2 is an indirect-gap semiconductor material. In Figures 7(b)–7(d), conduction band edges of S001 and S010 (S010_s and S010_{sn}) are about 1.2 eV, 1.15 eV, and 1.17 eV, respectively, suggesting that the CBM of S001 is more negative than that of S010, being consistent with the previous experimental result (Figure 4(b)). The more negative CBM suggests the stronger reduction ability of photogenerated electrons, resulting in the higher photocatalytic activity of the sheetlike SnS_2 . Previous study on different structures of TiO_2 has shown a similar result that a higher conduction band edge can generate more reductive electrons to generate the superoxide radicals $\cdot\text{O}_2^-$ to take part in the photocatalytic reaction [5]. Moreover, Figure 7(b) shows that the conduction band of S001 is very abrupt, indicating enhanced mobility of the electrons and hence a possible advantage for restraining recombination of the charge carriers [28, 29]. In contrast, the conduction band of S010 as shown in Figures 7(c) and 7(d) is very flat, which means electrons are easily localized and their mobility is low. It is well known that the increased charge carrier mobility is favorable for a better photocatalytic activity. Therefore, the superior photocatalytic activity of sheetlike SnS_2 could be ascribed to the favorable energy band structure over that of flowerlike SnS_2 in terms of both the thermal dynamics and kinetics of photocatalytic reaction.

4. Conclusions

Sheetlike SnS_2 single crystal exposed with well-defined {001} facets and flowerlike SnS_2 mainly exposed with {010} facets were prepared through a surfactant-free solvothermal process. Theoretical calculation showed that the surface energy of {010} facets was higher than that of {001} facets. However, the photocatalytic activity of flowerlike SnS_2 was much lower than that of sheetlike SnS_2 . XPS measurement and first-principle calculation revealed that the different surface atomic structures resulted in different electronic structures; that is, while the valence band maximum of two kinds of samples remained the same, the conduction band minimum of sheetlike SnS_2 was more negative than that of flowerlike SnS_2 . The higher conduction band minimum leads to a stronger oxidative ability, and thus a better photocatalytic activity for degradation of MO. Moreover, the higher mobility of the electrons in the more abrupt conduction band of sheetlike SnS_2 also leads to a remarkable enhancement of photocatalytic activity. The present work has provided a deep insight into the role of the surface energy and band structure, both of which are derived from the surface atomic structure, in the photocatalytic activity.

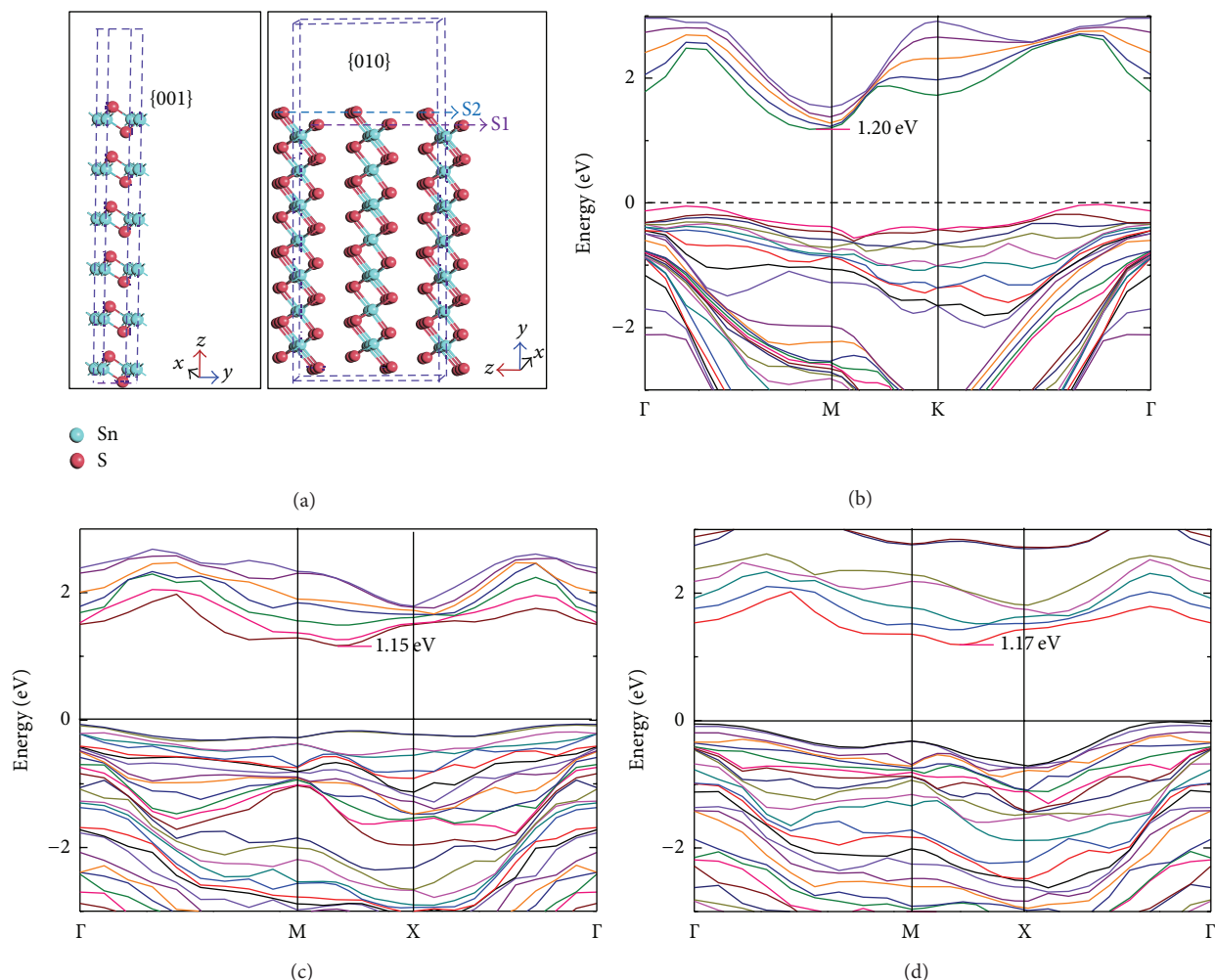


FIGURE 7: (a) Slab models of SnS_2 {001} and {010} surfaces; ((b)–(d)) electronic structures of S001 , S010_s and S010_{sn} , respectively.

Conflict of Interests

The authors declare that there is no conflict of interests regarding the publication of this paper.

Acknowledgments

This work was supported by the National Basic Research Program of China (973 Program, Contract no. 2014CB239301). Mengyi Li is grateful to Professor Jinhua Ye (NIMS) for hosting her internship visit to NIMS. Gratitude is also to Professor Hua Tong for valuable discussions. Mr. Wei Han (Tianjin Univ.) and Dr. Kun Chang (NIMS) are appreciated for their assistance in materials synthesis and photocatalytic activity evaluation. Calculations were carried out at the Shanghai Supercomputer Center.

References

- [1] A. Fujishima and K. Honda, "Photolysis-decomposition of water at the surface of an irradiated semiconductor," *Nature*, vol. 238, no. 1, pp. 37–38, 1972.
- [2] F. Seker, K. Meeker, T. F. Kuech, and A. B. Ellis, "Surface chemistry of prototypical bulk II-VI and II Vsemiconductors and implications for chemical sensing," *Chemical Reviews*, vol. 100, no. 7, pp. 2505–2536, 2000.
- [3] S. Liu, J. Yu, and M. Jaroniec, "Anatase TiO_2 with dominant high energy 001 facets: synthesis, properties, and applications," *Chemistry of Materials*, vol. 23, no. 10, Article ID 40854093, pp. 4085–4093, 2011.
- [4] S. H. Kang, S.-H. Choi, M.-S. Kang et al., "Nanorod-based dye-sensitized solar cells with improved charge collection efficiency," *Advanced Materials*, vol. 20, no. 1, pp. 54–58, 2008.
- [5] H. Xu, P. Reunchan, S. Ouyang et al., "Anatase TiO_2 single crystals exposed with high-reactive 111 facets toward efficient H_2 evolution," *Chemistry of Materials*, vol. 25, no. 3, pp. 405–411, 2013.
- [6] H. G. Yang, C. H. Sun, S. Z. Qiao et al., "Anatase TiO_2 single crystals with a large percentage of reactive facets," *Nature*, vol. 453, no. 7195, pp. 638–641, 2008.
- [7] G. Xi and J. H. Ye, "Synthesis of bismuth vanadate nanoplates with exposed 001 facets and enhanced visible light photocatalytic properties," *Chemical Communications*, vol. 46, no. 11, pp. 1893–1895, 2010.

- [8] J. Pan, G. Liu, G. Q. Lu, and H. M. Cheng, "On the true photoreactivity order of {001}, {010}, and {101} facets of anatase TiO₂ crystals," *Angewandte Chemie*, vol. 50, no. 9, pp. 2133–2137, 2011.
- [9] W. D. Shi, L. H. Huo, H. S. Wang, H. J. Zhang, and P. H. Wei, "Hydrothermal growth and gas sensing property of flower-shaped SnS₂ nanostructures," *Nanotechnology*, vol. 17, no. 12, pp. 2918–2924, 2006.
- [10] K. Chang, Z. Wang, G. Huang, H. Li, W. Chen, and J. Y. Lee, "Few-layer SnS₂/graphene hybrid with exceptional electrochemical performance as lithium-ion battery anode," *Journal of Power Sources*, vol. 201, pp. 259–266, 2012.
- [11] F. R. Tan, S. C. Qu, and X. B. Zeng, "Preparation of SnS₂ colloidal quantum dots and their application in organic/inorganic hybrid solar cells," *Nanoscale Research Letters*, vol. 6, no. 1, pp. 298–291, 2011.
- [12] Y. Sun, H. Cheng, S. Gao et al., "Atomically thick bismuth selenide freestanding single layers achieving enhanced thermoelectric energy harvesting," *Journal of the American Chemical Society*, vol. 134, no. 50, pp. 20294–20297, 2012.
- [13] H. Zhong, G. Yang, H. Song et al., "Vertically aligned graphene-like SnS₂ ultrathin nanosheet arrays: Excellent energy storage, catalysis, photoconduction, and field-emitting performances," *Journal of Physical Chemistry C*, vol. 116, no. 16, pp. 9319–9326, 2012.
- [14] J. F. Cao, Z. Xie, X. B. Duan et al., "Visible-light driven photocatalytic and photoelectrochemical properties of porous SnS_x (x = 1, 2) architectures," *CrystEngComm*, vol. 14, no. 9, pp. 3163–3168, 2012.
- [15] H. J. Chang, E. In, K. J. Kong, J. O. Lee, Y. M. Choi, and B. H. Ryu, "First-principles studies of SnS₂ nanotubes a potential semiconductor nanowire," *Journal of Physical Chemistry B*, vol. 109, no. 1, pp. 30–32, 2005.
- [16] J. Xia, G. C. Li, Y. C. Mao, Y. Y. Li, P. K. Shen, and L. P. Chen, "Hydrothermal growth of SnS₂ hollow spheres and their electrochemical properties," *CrystEngComm*, vol. 14, no. 13, pp. 4279–4283, 2012.
- [17] J. Ma, D. Lei, X. Duan et al., "Designable fabrication of flower-like SnS₂ aggregates with excellent performance in lithium-ion batteries," *RSC Advances*, vol. 2, no. 9, pp. 3615–3617, 2012.
- [18] A. Yella, E. Mugnaioli, M. Panthöfer, H. A. Therese, U. Kolb, and W. Tremel, "Bismuth-catalyzed growth of SnS₂ nanotubes and their stability," *Angewandte Chemie—International Edition*, vol. 48, no. 35, pp. 6426–6430, 2009.
- [19] J. W. Seo, J. T. Jang, S. W. Park, C. Kim, B. Park, and J. Cheon, "Two-dimensional SnS₂ nanoplates with extraordinary high discharge capacity for lithium ion batteries," *Advanced Materials*, vol. 20, no. 22, pp. 4269–4273, 2008.
- [20] Y. Ji, H. Zhang, X. Ma, J. Xu, and D. Yang, "Single-crystalline SnS₂ nano-belts fabricated by a novel hydrothermal method," *Journal of Physics Condensed Matter*, vol. 15, no. 44, pp. L661–L665, 2003.
- [21] Y.-T. Lin, J.-B. Shi, Y.-C. Chen, C.-J. Chen, and P.-F. Wu, "Synthesis and characterization of tin disulfide (SnS₂) nanowires," *Nanoscale Research Letters*, vol. 4, no. 7, pp. 694–698, 2009.
- [22] M. Fuchs and M. Scheffler, "Ab initio pseudopotentials for electronic structure calculations of poly-atomic systems using density-functional theory," *Computer Physics Communications*, vol. 119, no. 1, pp. 67–98, 1999.
- [23] M. Bockstedte, A. Kley, J. Neugebauer, and M. Scheffler, "Density-functional theory calculations for poly-atomic systems: electronic structure, static and elastic properties and ab initio molecular dynamics," *Computer Physics Communications*, vol. 107, no. 1–3, pp. 187–222, 1997.
- [24] Y. C. Zhang, Z. N. Du, K. W. Li, and M. Zhang, "Size-controlled hydrothermal synthesis of SnS₂ nanoparticles with high performance in visible light-driven photocatalytic degradation of aqueous methyl orange," *Separation and Purification Technology*, vol. 81, no. 1, pp. 101–107, 2011.
- [25] J. Pan, X. Wu, L. Wang, G. Liu, G. Q. Lu, and H.-M. Cheng, "Synthesis of anatase TiO₂ rods with dominant reactive 010 facets for the photoreduction of CO₂ to CH₄ and use in dye-sensitized solar cells," *Chemical Communications*, vol. 47, no. 29, pp. 8361–8363, 2011.
- [26] M. A. Butler, "Photoelectrolysis and physical properties of the semiconducting electrode WO₂," *Journal of Applied Physics*, vol. 48, no. 5, pp. 1914–1920, 1977.
- [27] S. C. Yan, Z. S. Li, and Z. G. Zou, "Photodegradation of rhodamine B and methyl orange over boron-doped g-C₃N₄ under visible light irradiation," *Langmuir*, vol. 26, no. 6, pp. 3894–3901, 2010.
- [28] S. X. Ouyang, H. T. Zhang, D. F. Li, T. Yu, J. H. Ye, and Z. G. Zou, "Electronic structure and photocatalytic characterization of a novel photocatalyst AgAlO₂," *Journal of Physical Chemistry B*, vol. 110, no. 24, pp. 11677–11682, 2006.
- [29] S. X. Ouyang, Z. S. Li, Z. Ouyang, T. Yu, J. H. Ye, and Z. G. Zou, "Correlation of crystal structures, electronic structures, and photocatalytic properties in a series of Ag-based oxides: AgAlO₂, AgCrO₂, and Ag₂CrO₄," *Journal of Physical Chemistry C*, vol. 112, no. 8, pp. 3134–3141, 2008.

Research Article

Structure, Optical Properties, and Photocatalytic Activity towards H₂ Generation and CO₂ Reduction of GaN Nanowires via Vapor-Liquid-Solid Process

Hong Pang,¹ Lequan Liu,^{2,3} Shuxin Ouyang,^{1,4} Hua Xu,^{1,4} Yunxiang Li,¹ and Defa Wang^{1,4}

¹ TU-NIMS Joint Research Center and Tianjin Key Laboratory of Composite and Functional Materials, School of Materials Science and Engineering, Tianjin University, 92 Weijin Road, Nankai District, Tianjin 300072, China

² Environmental Remediation Materials Unit, National Institute for Materials Science (NIMS), 1-1 Namiki, Tsukuba, Ibaraki 305-0044, Japan

³ International Center for Materials Nanoarchitectonics (WPI-MANA), National Institute for Materials Science (NIMS), 1-1 Namiki, Tsukuba, Ibaraki 305-0044, Japan

⁴ Collaborative Innovation Center of Chemical Science and Engineering (Tianjin), 92 Weijin Road, Nankai District, Tianjin 300072, China

Correspondence should be addressed to Defa Wang; defawang@tju.edu.cn

Received 14 July 2014; Accepted 8 September 2014; Published 1 December 2014

Academic Editor: Wenjun Luo

Copyright © 2014 Hong Pang et al. This is an open access article distributed under the Creative Commons Attribution License, which permits unrestricted use, distribution, and reproduction in any medium, provided the original work is properly cited.

High quality single crystalline GaN nanowires with large aspect ratio (>100) are synthesized on n-type Si (111) substrate via Au-catalyzed vapor-liquid-solid process. Morphology, crystal structure, and optical property of the as-synthesized GaN nanowires are characterized by means of X-ray diffraction, scanning/transmission electron microscopy, UV-vis diffuse reflection spectroscopy, and room temperature photoluminescence. The results indicate that the as-prepared GaN nanowires with a large aspect ratio are well crystallized in the hexagonal wurtzite structure, and a slight blue shift appears in both the absorption edge and emission peak probably due to the quantization effect. Photocatalytic H₂ evolution over the as-prepared GaN nanowires is performed with the incorporation of Pt or Rh as the cocatalyst, exhibiting greatly enhanced capability compared to the GaN powder tested under the same conditions. Moreover, photocatalytic CO₂ reduction over the GaN nanowires is also successfully realized using Pt or Rh as the cocatalyst, depending on which the products show a strong selectivity inherently related to the reductive electrons transferred by cocatalyst.

1. Introduction

In view of the globally concerned energy shortage and environment pollution issues, photocatalysis using semiconductor and solar energy has been regarded as an ideal green chemistry technology [1–3]. While TiO₂-based photocatalysts were most popularly studied in last four decades [4], a huge number of new semiconducting materials have also been developed for photocatalytic applications. For example, a direct III–V group semiconductor GaN has been attracting extensive attention due to the following facts [5–8]: the band structure of GaN can encompass several possible redox

potentials; in addition, the high stability of GaN makes it work well under various harsh conditions.

One-dimensional (1D) nanomaterials have been paid much attention in photocatalytic field owing to their advantageous properties compared to the particulate materials [9]. On one hand, the surface-to-volume ratio can be enhanced due to the large surface area exposed on the nanowires, which in turn can act as the active sites for physical and chemical processes. On the other hand, 1D nanostructures provide the possibility of guiding the charge carriers transport in restricted pathways by limiting the transport in the transverse direction. By modifying the nanostructures with cocatalysts

as the reactive sites, the charge carriers, especially electrons, are prone to accumulate at the reduction sites, thus enhancing the separation of the photogenerated electrons and holes [10]. For above reasons, a lot of researches have focused on photocatalytic water splitting over GaN nanowires and great progresses have been achieved in recent years [11, 12]. For the synthesis of substrate-supported GaN nanostructures, the plasma-assisted molecular beam epitaxy (MBE) [13] and metal-organic chemical vapor deposition (MOCVD) [14] are widely used. However, the high cost and low production efficiency have limited their practical application.

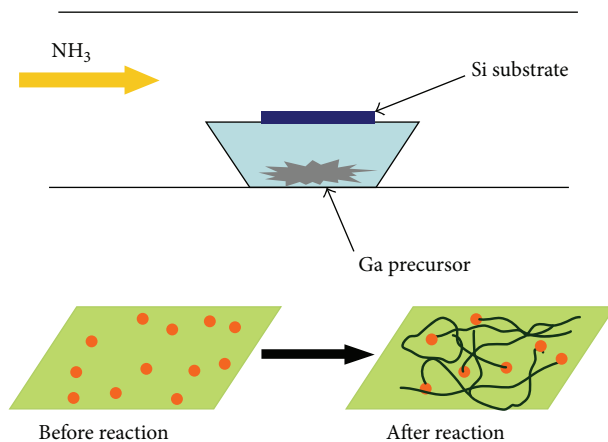
In this paper, we report a simple and cheap chemical vapor deposition (CVD) method to prepare GaN nanowires in a tube furnace at ambient pressure. The growth of GaN nanowires by Au-catalyzed CVD process is based on the vapor-liquid-solid (VLS) mechanism [15]. Photocatalytic activities of GaN nanowires for H_2 evolution and CO_2 reduction are performed and the effect of noble metal cocatalyst (e.g., Pt and Rh) on the photocatalytic activity is also clarified.

2. Materials and Methods

2.1. Fabrication of GaN Nanowires. GaN nanowires were grown via a two-step process. Pieces of $2 \times 2 \text{ cm}^2$ n-type Si (111) substrates (Sinopharm Chemical Reagent Co., Ltd) were ultrasonically cleaned in acetone and alcohol for 30 min each before rinsing with deionized water. Using an ion sputtering coater (SCB-12, KYKY Technology Development Ltd., China), a very thin gold film was coated on the substrates to catalyze the GaN nanowires growth. The Ga precursor, Ga_2O_3 , was used as received without any further treatment.

As illustrated in Scheme 1, GaN nanowires were grown by means of chemical vapor deposition in a horizontal quartz tube furnace ($\Phi 60 \times 1000 \text{ mm}$, GSL-1200X, Hefei Kejing Materials Technology CO., LTD, China). The Si substrate was loaded into a polycrystalline alumina crucible, upright on the Ga source, and then the crucible was put into the middle of the quartz tube. Both the Ga precursor and the substrate were heated to 1000°C for 1 h and flowed with 60 mL/min NH_3 and then the reactor was naturally cooled down to the room temperature under flow of the carrier gas.

2.2. Materials Characterization. The morphology and microstructure of the as-synthesized sample were observed on a field-emission scanning electron microscope (FE-SEM; S4800, JOEL, Japan, operated at 5 kV) equipped with an EDAX (Genesis XM2) attachment and a high-resolution transmission electron microscope (HRTEM; JEM-2100F, JEOL, Japan). Crystal structure was measured on an X-ray diffractometer (XRD; Bruker D8, operated at 40 kV , 40 mA) using $Cu \text{ K}\alpha$ radiation ($\lambda = 1.54 \text{ \AA}$). UV-vis diffuse reflectance spectra were measured at room temperature in the range of $220\text{--}800 \text{ nm}$ on a UV-vis spectrophotometer (UV-2700; Shimadzu, Japan) and converted to absorbance by the Kubelka-Munk method. Photoluminescence (PL) spectra were acquired on a spectrofluorometer (Fluorolog-3 system, Horiba Jobin Yvon) with an excitation wavelength of 320 nm .



SCHEME 1: CVD reaction setup and growth mechanism for GaN nanowires by the vapor-liquid-solid process.

2.3. Photocatalytic Performance. Photocatalytic water splitting was carried out in a quartz glass cell (220 mL) connected to a glass-closed gas circulation and evacuation system. A 300 W UV-enhanced Xenon lamp was used as the light source. To improve the photocatalytic activity, 0.5 wt\% Rh and 0.5 wt\% Pt were preloaded on the surface of GaN nanowires by the in situ photodeposition method: under light irradiation, an equivalent molar amount of Na_3RhCl_6 or H_2PtCl_6 in solution (50 mL water + 10 mL methanol) was reduced to metallic state and deposited onto catalyst surface, forming the Rh or Pt-loaded catalyst.

Before reaction, the cell containing the reactant solution was well evacuated and then $\sim 2.5 \text{ kPa}$ of argon gas was introduced as carrier gas. With increase of irradiation time, the gases evolved photocatalytically were mixed and circulated by an online electromagnetic circulation pump. The gases evolved were in situ analyzed with an online TCD gas chromatograph (Shimadzu GC-8AIT, argon carrier).

Photocatalytic CO_2 reduction was carried out in a quartz glass reactor, in which the GaN nanostructured film on the Si substrate with an area of $2 \times 1 \text{ cm}^2$ was placed, and 3 mL of deionized water was injected. The 300 W UV-enhanced Xe lamp was used as the light source. The reactor was connected to a closed gas circulation and evacuation system. After evacuating the online system, high purity of CO_2 was purged into the reactor until a pressure of 80 kPa was achieved. The products from CO_2 reduction were detected by an online gas chromatograph (GC-14B, Shimadzu).

3. Results and Discussion

GaN nanowires grown on Si substrates are seemingly yellowish. By tuning the important growth parameters such as the starting materials, growth temperature, and the rate of NH_3 flow, a variety of GaN nanowires with different morphologies can be selectively prepared. Shown in Figure 1(a) is a typical FE-SEM image of GaN nanowires with lengths from several tens to hundreds micrometers and quite uniform diameter of *ca.* 80 nm in average. Apparently, the aspect ratio of

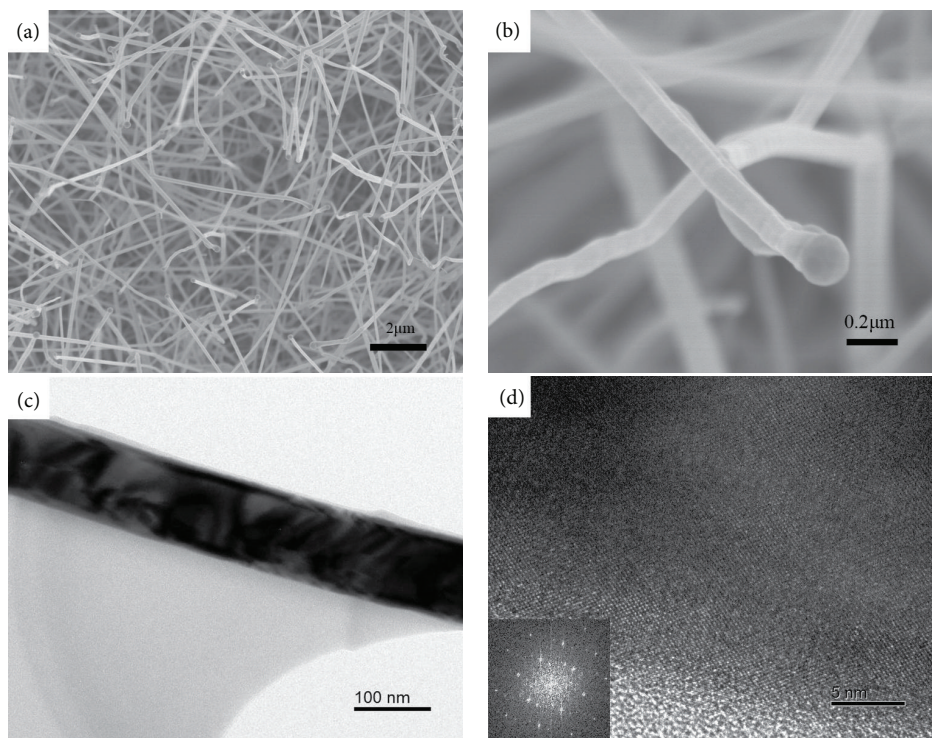


FIGURE 1: (a) Low magnification SEM image; (b) high magnification SEM image of the GaN nanowires synthesized via a vapor-liquid-solid process; (c) conventional low magnification TEM image; and (d) HRTEM image of a GaN nanowire (inset: FFT diffraction pattern of the corresponding HRTEM).

the as-grown GaN nanowires is extremely large (>100). Close examination reveals that over 95% of the products are nanowires, of which the side surface is smooth and straight. From the enlarged SEM image (Figure 1(b)) we can see clearly the droplet of Au nanoparticles on the apex of each nanowire, indicating the vapor-liquid-solid (VLS) mechanism for growth of GaN nanowires.

Figure 1(c) shows a typical TEM image, from which the smooth side surface can be clearly seen. Shown in Figure 1(d) are the HRTEM image and its corresponding fast Fourier transform (FFT) pattern (inset). No defects were observed from the HRTEM image, confirming the good crystallinity of the GaN nanowires, whereas the regular FFT patterns reveal the single crystalline nature of the nanowires.

Figure 2 shows the XRD pattern of GaN nanowires grown on the Si substrates. All peaks except those from Si substrate ($2\theta = 28.6^\circ$) and Au catalyst ($2\theta = 38.5^\circ$) can be precisely indexed as the wurtzite GaN structure (JCPDS card, number 74-0243). The refined crystal parameters $a = b = 3.189 \text{ \AA}$ and $c = 5.166 \text{ \AA}$ are in good agreement with previously reported standard values, implying the good crystallinity of as-grown GaN nanowires. In fact, the sharp diffraction peak shown in the XRD pattern (see Figure 2) also confirms that the GaN nanowires are well crystallized. It should be noted that no characteristic peaks corresponding to impurities such as GaON [16] and the starting materials were present in the XRD patterns, further demonstrating the high purity of the GaN nanowires.

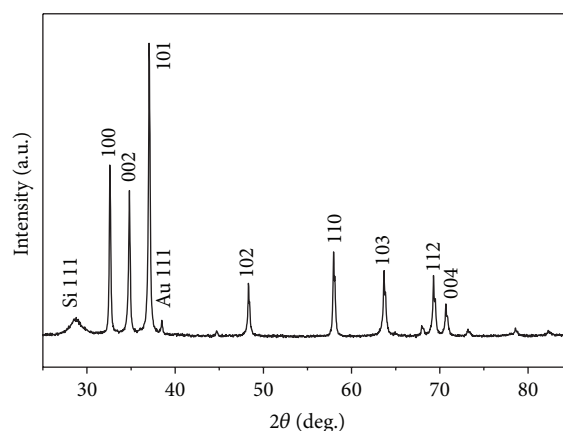


FIGURE 2: XRD pattern and indices of the GaN nanowires grown on Si substrate by Au-catalyzed vapor-liquid-solid reaction. All peaks except those from Si ($2\theta = 28.6^\circ$) and Au ($2\theta = 38.5^\circ$) can be indexed as the wurtzite GaN structure.

UV-vis diffuse reflectance spectrum (DRS) and room temperature photoluminescence (PL) spectrum of the as-prepared GaN nanowires were measured and the results are shown in Figure 3. From the UV-vis DRS spectrum, we can see a steep absorption edge located at *ca.* 355 nm, which is slightly shorter than that of the bulk GaN [17], probably due to the quantum confinement effect in nanomaterials. It should be pointed out that, in addition to the main absorption edge,

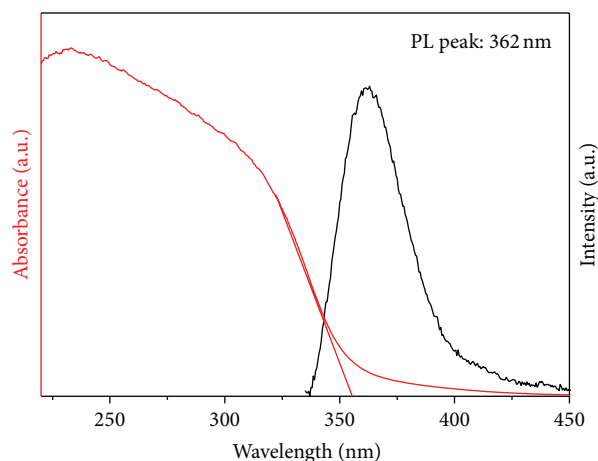


FIGURE 3: UV-visible diffuse reflectance spectrum (red) and room temperature photoluminescence spectrum (black) of the as-grown GaN nanowires on Si substrate.

the long tail can also be observed in visible region. Highly likely, the long absorption tail resulted from the Si substrate and/or the possible plasmonic effect of Au nanoparticles.

The room temperature photoluminescence (PL) is usually adopted to get the radiation-emission-related information such as the crystal defects and impurity levels in semiconductors. As shown in Figure 3, the emission peak centered at 362 nm in the PL spectrum is in good consistency with the standard peak [18] position of wurtzite GaN. Moreover, the sharp and smooth PL peak indicate the high crystalline quality of the as-prepared GaN nanowires.

Previous study has shown that GaN is a promising candidate to split water into H_2 since its conduction band edge of GaN is more negative than the H^+/H_2 reduction potential [19]. For the as-prepared GaN nanowires, photocatalytic H_2 evolution was performed in presence of methanol (50 mL H_2O , 10 mL CH_3OH) as the hole scavenger. In this reaction, 0.5 wt% Pt was in situ photodeposited as cocatalyst on the surface of GaN nanowires. As a comparison, GaN powders were also prepared by CVD method for photocatalytic H_2 evolution under the same conditions as mentioned above. Figure 4 shows the time courses of H_2 evolution on 0.5 wt% Pt/GaN-NWs and 0.5 wt% Pt/GaN-powder, respectively. With increase of irradiation time, H_2 evolution increased almost linearly. The rate of H_2 evolution over 5 h reaction with 0.5 wt% Pt/GaN-NWs was $6582 \mu\text{mol}\cdot\text{h}^{-1}\cdot\text{g}^{-1}$, while that with 0.5 wt% Pt/GaN-powder was only about $25 \mu\text{mol}\cdot\text{h}^{-1}\cdot\text{g}^{-1}$. Clearly, the 1-D GaN nanowires are much more advantageous over the GaN powders for photocatalytic H_2 evolution.

It is well known that the cocatalysts play a significant role in photocatalytic water splitting [20]. The interfacial charge transfer from the flat band of GaN to the Femi level of Pt can drive the water splitting more efficiently [21]. In this work, we also investigated the effect of another metal cocatalyst Rh, which has been proven to promote H_2 evolution in the Rh/ Cr_2O_3 core-shell structure. As shown in Figure 5, when the same amount of Pt and Rh was loaded, respectively, on the surface of as-prepared GaN nanowires with the same

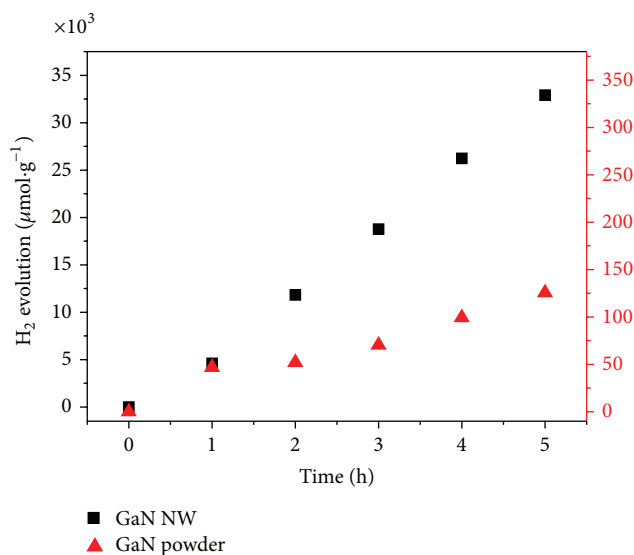


FIGURE 4: Photocatalytic H_2 generation over the 0.5 wt% Pt-loaded GaN nanowires and 0.5 wt% Pt-loaded GaN powder under a 300 W UV-enhanced Xenon lamp irradiation.

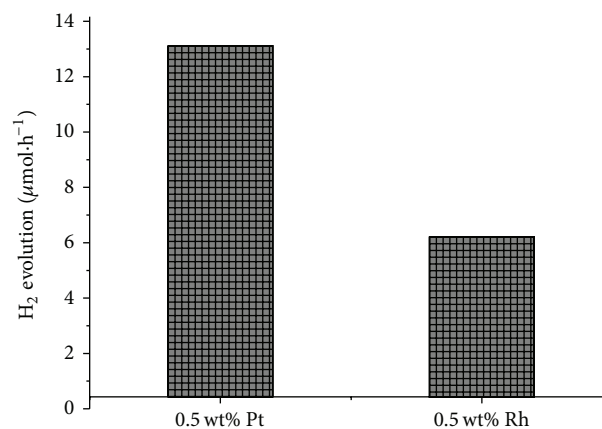


FIGURE 5: Photocatalytic H_2 generation from aqueous methanol solution over 0.5 wt% Pt/GaN-NWs and 0.5 wt% Rh/GaN-NWs under UV-enhanced irradiation. Reaction time: 1 h.

irradiation area ($\sim 2 \times 1\text{cm}^2$), an obvious difference was found in H_2 generation under the same conditions: Pt was a more effective cocatalyst than Rh for H_2 evolution. It should be pointed out that the structural stability of GaN nanowires has been confirmed since no difference was detected on the XRD patterns of the samples before and after the photocatalytic reaction.

The photocatalytic reduction of atmospheric CO_2 into hydrocarbon fuels is also one of the main targets for conversion of solar energy into chemical energy [22]. Herein, CO_2 reduction on Rh/GaN-NWs and on Pt/GaN-NWs was also conducted. Figure 6 shows the production of CH_4 and CO under UV-enhanced Xe lamp irradiation for 13.5 h. It was found that CH_4 and CO were the main products of CO_2 conversion, and the cocatalyst played a significant role in the selectivity of products. For Pt-loaded GaN nanowires,

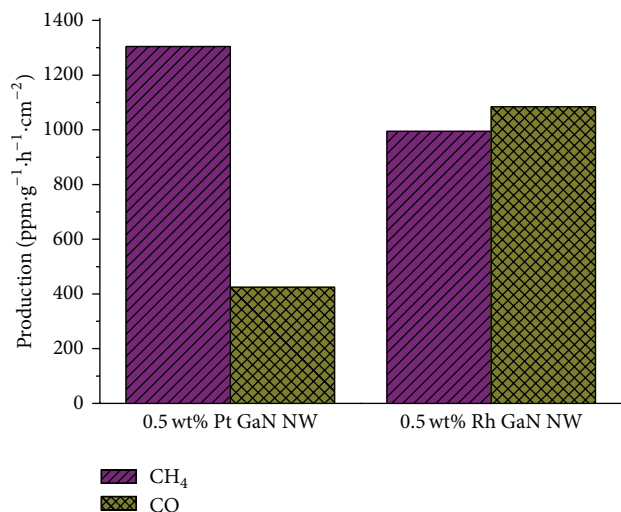


FIGURE 6: Photocatalytic CO₂ reduction tests over 0.5 wt% Pt/GaN NWs and 0.5 wt% Rh/GaN NWs under UV-enhanced irradiation.

CH₄ was the main product with an average conversion rate of 1304.8 ppm·h⁻¹·g⁻¹·cm⁻², which was in a strong contrast to an average rate of 424.8 ppm·h⁻¹·g⁻¹·cm⁻² for CO. For Rh-loaded GaN nanowires, both CO and CH₄ were the main products with a rate of 1084.6 ppm·h⁻¹·g⁻¹·cm⁻² and 994 ppm·h⁻¹·g⁻¹·cm⁻², respectively. The abovementioned results implied that the cocatalysts played a crucial role in the final product of photoreduction reaction. The photocatalytic CO₂ reduction involves a series of multielectrons reaction. Carbon monoxide (CO) is the most common product in photoreduction reactions since this step only needs two electrons and protons and single electron transfer to CO₂ occurs at $-0.53V_{\text{NHE}}$. However, to reform CH₄ with CO₂, six more electrons and same amounts of protons are required with the redox potential at $-0.24V_{\text{NHE}}$ [23]. The noble metal, Pt, with larger work function and lower Fermi level than Rh, facilitates trapping the generated electrons more readily from the conduction band of GaN [20, 24]. Therefore, higher photocatalytic conversion of CO₂ to CH₄ is observed when loaded with Pt.

4. Conclusion

High quality single crystalline GaN nanowires are successfully synthesized through a vapor-liquid-solid process. Compared to the powder GaN samples also prepared by CVD method, GaN nanowires show significantly enhanced photocatalytic activities both for H₂ evolution from water splitting and for CO₂ reduction. Two noble metals Pt and Rh were photodeposited on the surface of GaN nanowires as cocatalysts in above reactions. It has been found that, for H₂ evolution, Pt/GaN nanowires show a higher photocatalytic activity than Rh/GaN nanowires, whereas, for CO₂ reduction, the cocatalyst plays an important role in controlling the multielectron reaction, that is, the final product selectivity: Pt/GaN was beneficial to reduce CO₂ to CH₄ while Rh/GaN produced nearly equal amount of CO and CH₄.

Conflict of Interests

The authors declare that there is no conflict of interests regarding the publication of this paper.

Acknowledgments

This work was supported by the Tianjin Natural Science Foundation (Contract no. 13JCYBJC16600) and the National Basic Research Program of China (973 Program, Contract no. 2014CB239301). Ms. Hong Pang is grateful to Professor Jinhua Ye (NIMS) for hosting her internship visit to NIMS. Gratitude is also due to Professor Hua Tong and Dr. Hailin Qiu for valuable discussions. Dr. Wenjun Yan and Dr. Peng Li are appreciated for assistance in sample preparation and photocatalytic evaluation.

References

- [1] H. Tong, S. Ouyang, Y. Bi, N. Umezawa, M. Oshikiri, and J. Ye, "Nano-photocatalytic materials: possibilities and challenges," *Advanced Materials*, vol. 24, no. 2, pp. 229–251, 2012.
- [2] A. Fujishima and K. Honda, "Electrochemical photolysis of water at a semiconductor electrode," *Nature*, vol. 238, no. 5358, pp. 37–38, 1972.
- [3] H. Xu, S. Ouyang, P. Li, T. Kako, and J. Ye, "High-active anatase TiO₂ nanosheets exposed with 95% 100 facets toward efficient H₂ evolution and CO₂ photoreduction," *ACS Applied Materials & Interfaces*, vol. 5, no. 4, pp. 1348–1354, 2013.
- [4] H. Xu, S. Ouyang, L. Liu et al., "Recent advances in TiO₂-based photocatalysis," *Journal of Materials Chemistry A*, vol. 2, no. 32, pp. 12642–12661, 2014.
- [5] H. S. Jung, Y. J. Hong, Y. Li, J. Cho, Y.-J. Kim, and G.-C. Yi, "Photocatalysis using GaN nanowires," *ACS Nano*, vol. 2, no. 4, pp. 637–642, 2008.
- [6] D. Wang, A. Pierre, M. G. Kibria et al., "Wafer-level photocatalytic water splitting on gan nanowire arrays grown by molecular beam epitaxy," *Nano Letters*, vol. 11, no. 6, pp. 2353–2357, 2011.
- [7] K. Maeda, K. Teramura, N. Saito, Y. Inoue, and K. Domen, "Photocatalytic overall water splitting on Gallium nitride powder," *Bulletin of the Chemical Society of Japan*, vol. 80, no. 5, pp. 1004–1010, 2007.
- [8] N. Arai, N. Saito, H. Nishiyama et al., "Effects of divalent metal ion (Mg²⁺, Zn²⁺ and Be²⁺) doping on photocatalytic activity of ruthenium oxide-loaded gallium nitride for water splitting," *Catalysis Today*, vol. 129, no. 3-4, pp. 407–413, 2007.
- [9] P. Yang, R. Yan, and M. Fardy, "Semiconductor nanowire: whats Next?" *Nano Letters*, vol. 10, no. 5, pp. 1529–1536, 2010.
- [10] P. Roy, D. Kim, K. Lee, E. Spiecker, and P. Schmuki, "TiO₂ nanotubes and their application in dye-sensitized solar cells," *Nanoscale*, vol. 2, no. 1, pp. 45–59, 2010.
- [11] M. G. Kibria, H. P. T. Nguyen, K. Cui et al., "One-step overall water splitting under visible light using multiband InGaN/GaN nanowire heterostructures," *ACS Nano*, vol. 7, no. 9, pp. 7886–7893, 2013.
- [12] M. G. Kibria, S. Zhao, F. A. Chowdhury et al., "Tuning the surface Fermi level on p-type gallium nitride nanowires for efficient overall water splitting," *Nature Communications*, vol. 5, article 3825, 2014.

- [13] B. Heying, R. Averbeck, L. F. Chen, E. Haus, H. Riechert, and J. S. Speck, "Control of GaN surface morphologies using plasma-assisted molecular beam epitaxy," *Journal of Applied Physics*, vol. 88, no. 4, pp. 1855–1860, 2000.
- [14] T. Kuykendall, P. Pauzauskie, S. Lee, Y. Zhang, J. Goldberger, and P. Yang, "Metalorganic chemical vapor deposition route to GaN nanowires with triangular cross sections," *Nano Letters*, vol. 3, no. 8, pp. 1063–1066, 2003.
- [15] X. Duan and C. M. Lieber, "Laser-assisted catalytic growth of single crystal GaN nanowires," *Journal of the American Chemical Society*, vol. 122, no. 1, pp. 188–189, 2000.
- [16] M. Kerlau, O. Merdrignac-Conanec, P. Reichel, N. Bârsan, and U. Weimar, "Preparation and characterization of gallium (oxy)nitride powders. Preliminary investigation as new gas sensor materials," *Sensors and Actuators, B: Chemical*, vol. 115, no. 1, pp. 4–11, 2006.
- [17] G. Yu, G. Wang, H. Ishikawa et al., "Optical properties of wurtzite structure GaN on sapphire around fundamental absorption edge (0.78–4.77 eV) by spectroscopic ellipsometry and the optical transmission method," *Applied Physics Letters*, vol. 70, no. 24, pp. 3209–3211, 1997.
- [18] A. H. Chin, T. S. Ahn, H. Li et al., "Photoluminescence of GaN nanowires of different crystallographic orientations," *Nano Letters*, vol. 7, no. 3, pp. 626–631, 2007.
- [19] P. G. Moses and C. G. van de Walle, "Band bowing and band alignment in InGaN alloys," *Applied Physics Letters*, vol. 96, no. 2, Article ID 021908, 2010.
- [20] J. Yang, D. Wang, H. Han, and C. Li, "Roles of cocatalysts in photocatalysis and photoelectrocatalysis," *Accounts of Chemical Research*, vol. 46, no. 8, pp. 1900–1909, 2013.
- [21] M. Yoshida, A. Yamakata, K. Takanabe, J. Kubota, M. Osawa, and K. Domen, "ATR-SEIRAS investigation of the fermi level of Pt cocatalyst on a GaN photocatalyst for hydrogen evolution under irradiation," *Journal of the American Chemical Society*, vol. 131, no. 37, pp. 13218–13219, 2009.
- [22] S. Yotsuhashi, M. Deguchi, Y. Zenitani et al., "CO₂ conversion with light and water by GaN photoelectrode," *Japanese Journal of Applied Physics*, vol. 51, no. 2S, Article ID 02BP07, 2012.
- [23] W.-N. Wang, J. Soulis, Y. Jeffrey Yang, and P. Biswas, "Comparison of CO₂ photoreduction systems: a review," *Aerosol and Air Quality Research*, vol. 14, no. 2, pp. 533–549, 2014.
- [24] S. Halas and T. Durakiewicz, "Work functions of elements expressed in terms of the Fermi energy and the density of free electrons," *Journal of Physics: Condensed Matter*, vol. 10, no. 48, pp. 10815–10826, 1998.

Research Article

Preparation of Cerium Modified Titanium Dioxide Nanoparticles and Investigation of Their Visible Light Photocatalytic Performance

Jinfeng Liu, Haiyan Li, Qiuye Li, Xiaodong Wang, Min Zhang, and Jianjun Yang

Key Laboratory for Special Functional Materials, Henan University, Kaifeng 475004, China

Correspondence should be addressed to Qiuye Li; qiuyeli@henu.edu.cn and Jianjun Yang; yangjianjun@henu.edu.cn

Received 4 July 2014; Revised 21 August 2014; Accepted 8 September 2014; Published 1 December 2014

Academic Editor: Wenjun Luo

Copyright © 2014 Jinfeng Liu et al. This is an open access article distributed under the Creative Commons Attribution License, which permits unrestricted use, distribution, and reproduction in any medium, provided the original work is properly cited.

Mesoporous $\text{CeO}_x/\text{TiO}_2$ nanoparticles have been successfully synthesized using titanate nanotubes as precursor through the hydrothermal-calcination method. The as-prepared materials were characterized by means of X-ray diffraction (XRD), X-ray photoelectron spectroscopy (XPS), transmission electron microscope (TEM), UV-vis diffuse reflectance spectra and nitrogen adsorption-desorption isotherm analysis. All the obtained $\text{CeO}_x/\text{TiO}_2$ materials exhibit anatase phase. Ce element existed in two valance states of Ce^{3+} and Ce^{4+} . Introduction of Ce species can effectively extend the spectral response from UV to visible light region. N_2 adsorption-desorption analysis revealed that all the samples belong to mesoporous structure and have large BET surface area compared with P25. The $\text{CeO}_x/\text{TiO}_2$ nanoparticles showed excellent photocatalytic activity in the degradation of MB under visible light irradiation.

1. Introduction

TiO_2 -based materials have been investigated intensively because of their outstanding physical and chemical properties and have been widely used in solar cells, gas sensors, photocatalysis, and other environmentally related applications [1–6]. However, the low utilization of the sunlight by titanium dioxide limits its practical application. Foreign ions doping is considered to be an effective approach to extend the light response to the visible light region of titanium dioxide [7–10]. Among these foreign ions, ceria (CeO_2), as an active system in the photodegradation of several molecules [11–13], has been intensively concerned. The redox shift between CeO_2 and Ce_2O_3 can provide high capacity to store/release oxygen, which plays the role as an oxygen reservoir to exhibit excellent characteristics in transferring electrons. What's more, it also can shift the adsorption band toward to visible light range. Xiao et al. reported that mesoporous cerium doped TiO_2 nanofibers exhibited the highest photocatalytic activity under visible irradiation compared with the undoped

TiO_2 nanofiber and the commercial Degussa P25 [14]. Xu et al. have reported that cerium doped titania could photocatalytically degrade formaldehyde under visible light [15]. Li et al. synthesized the ordered mesoporous CeO_2 doped TiO_2 photocatalyst by an evaporation-induced self-assembly method; their results showed that doping CeO_2 species into TiO_2 framework not only improves the thermal stability of the ordered mesoporous structure but also effectively extends the photoresponse of TiO_2 to the visible light region [16]. Nakamura et al. found that the Ti(IV)-O-Ce(III) bimetallic assemblies on mesoporous silica were an efficient visible light photocatalyst for the photooxidation of 2-propanol [17].

Nanotubes titanate acid (NTA) attracted much attention due to their many excellent properties, such as large BET surface area, strong adsorption capability, ion-exchange capacity, and one-dimensional structure. Recently, Viana et al. synthesized nanotubes titanate acid decorated with CeO_2 nanoparticles, and they reported that absorption region red-shifted apparently after decorating, and these composites can photodegrade the reactive blue 19 textile dye to a

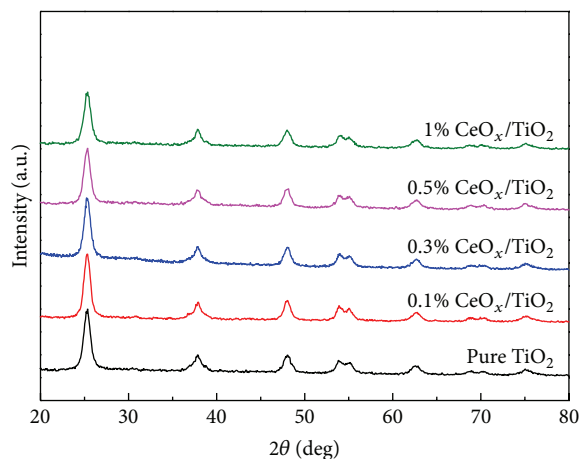


FIGURE 1: XRD patterns of $x\%$ $\text{CeO}_x/\text{TiO}_2$ nanoparticles obtained from NTA.

certain extent [18]. One of the main researches of our group focuses on the titanate nanotubes and their derivatives. Their morphology, structure, light absorption, thermal stability, formation mechanism, and photoelectrochemical and photocatalytic properties were investigated systematically through decades [19–22]. We found that the crystallinity of NTA was very poor and the photocatalytic activity was not good. However, the crystallinity and photocatalytic performance can be improved largely after thermal dehydration and structure reassemblage of NTA.

In this work, $x\%$ $\text{CeO}_x/\text{TiO}_2$ was prepared using NTA as the Ti precursor by the hydrothermal-calcination method. The doped Ce existed in the two valence states of Ce^{3+} and Ce^{4+} , which can act as the electron acceptor to improve the separation efficiency of the photogenerated electron-hole pairs. Moreover, the absorption of the visible light extended more apparently than that of the reference TiO_2 . The photodegradation yield of MB on $\text{CeO}_x/\text{TiO}_2$ was much higher than the commercial P25. The relationship between the morphology, structure, light absorption, and the photocatalytic performance was investigated in detail.

2. Experimental

2.1. Preparation of $\text{CeO}_x/\text{TiO}_2$. The titania precursor of nanotubular titanic acid (NTA) was prepared according to our previous reports [23]. A proper amount of $\text{Ce}(\text{NO}_3)_3$ and 1 g of NTA were dissolved in 60 mL of deionized water and mixed by stirring. Then the resultant mixed suspension was transferred to the autoclave reactor and kept at 120°C for 4 h. The resultant mixture was transferred to a round bottom flask to evaporate water by a vacuum distillation and then the production was calcined at 400°C for 2 h. And as a result, the $\text{CeO}_x/\text{TiO}_2$ was obtained. The atomic ratio of Ce and Ti was designed as 0.1%, 0.3%, 0.5%, and 1%, and the samples were denoted as $x\%$ $\text{CeO}_x/\text{TiO}_2$.

2.2. Characterization. The phase structure of various $\text{CeO}_x/\text{TiO}_2$ samples was analyzed by X-ray diffraction (XRD,

Philips X'Pert Pro X-ray diffractometer; Cu-K α radiation, $\lambda = 0.15$ nm). The X-ray photoelectron spectroscopic (XPS) measurement was carried out using ESCALAB210 with dual anode Mg X-ray source. All spectra were calibrated to the binding energy of the adventitious C 1s peak at 285 eV. All samples were observed using a transmission electron microscopy (TEM, JEOL JEM-2100, accelerating voltage 200 kV). UV-vis diffuse reflectance spectra (DRS) were obtained on a Shimadzu U-3010 spectrometer, using BaSO_4 as a reference. The Brunauer-Emmett-Teller (BET) surface areas and average pore volumes were measured by automatic surface area and porosity analyzer (QUADRASORB SI).

2.3. Photocatalytic Reaction. The photocatalytic activity of each sample was evaluated in terms of the degradation of MB (10 mg/L). 0.1 g of photocatalyst was added into a 100 mL quartz photochemical reactor containing 100 mL of MB (10 mg/L) aqueous solution. The mixture was stirred for 1.5 h in dark to reach the adsorption-desorption equilibrium. A 300 W Xe lamp equipped with a UV cut-off filter ($\lambda > 420$ nm) was used as a visible light source. At given time intervals, the analytical samples were taken from the mixture and immediately centrifuged and then filtered to remove the particles. The concentration of MB was analyzed by checking the absorbance at 664 nm with a UV-vis spectrophotometer (UV-2500, Shimadzu, Japan). The photocatalytic behavior of Degussa P25 was also measured in the same conditions as a reference. The 4-chlorophenol (4-CP, 12 mg/L) was also selected as the colorless model pollutant to further evaluate the photocatalytic activity.

3. Results and Discussions

The XRD patterns of the series of $\text{CeO}_x/\text{TiO}_2$ samples with different content of Ce are shown in Figure 1. All of these $\text{CeO}_x/\text{TiO}_2$ samples show the typical anatase crystal phase; the typical diffraction peaks at 25.3° , 37.8° , 48.0° , 53.9° , 55.0° , and 62.7° corresponded to the (101), (104), (200), (105), (211), and (204) plane facet, respectively. Our previous

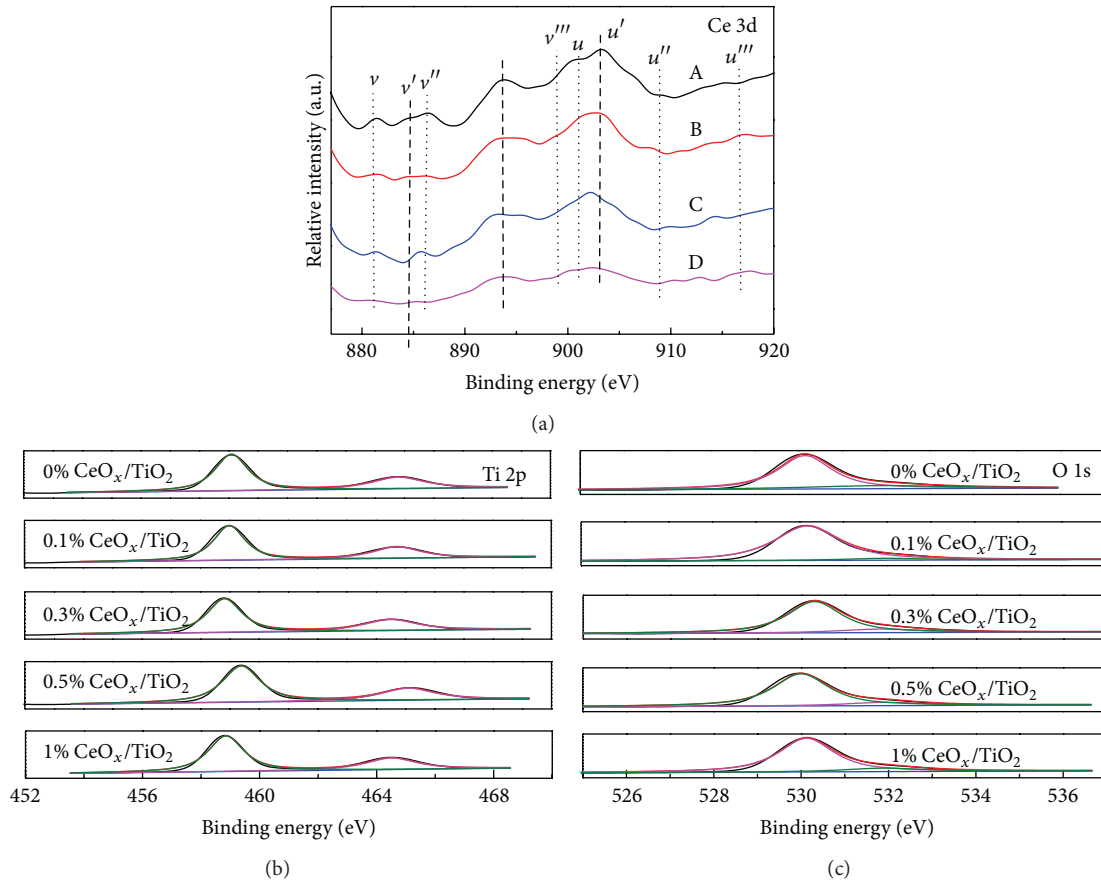


FIGURE 2: XPS spectra of $x\%$ $\text{CeO}_x/\text{TiO}_2$ nanoparticles (a) Ce 3d: (A) 1% $\text{CeO}_x/\text{TiO}_2$, (B) 0.5% $\text{CeO}_x/\text{TiO}_2$, (C) 0.3% $\text{CeO}_x/\text{TiO}_2$, and (D) 0.1% $\text{CeO}_x/\text{TiO}_2$; (b) Ti 2p; (c) O 1s.

work has reported that NTA belongs to an orthorhombic crystallinity [21]. From the above XRD results, we knew that NTA had been transformed to anatase TiO_2 completely through the hydrothermal-calcination process. The anatase peaks position of all samples undergoes almost no significant changes; this may be because the ionic radii of $\text{Ce}^{3+}/\text{Ce}^{4+}$ (1.03/1.02 Å) are much bigger than that of Ti^{4+} (0.68 Å), so it is difficult for Ce^{3+} or Ce^{4+} to replace Ti^{4+} in the crystal lattice [14]. Thus, we inferred that cerium species should be in the form of cerium oxide modified on the surface of TiO_2 . However, the intensive peaks of all kinds of cerium species ($\text{CeO}_2/\text{Ce}_2\text{O}_3$) cannot be identified in XRD patterns. This should be due to the small content of cerium oxide species to be detected. Through calculation by the Scherrer formula, the particle sizes of $\text{CeO}_x/\text{TiO}_2$ are ca. 8–12 nm and there is no apparent difference between the samples with different content of Ce.

XPS analysis was conducted to understand the surface chemical state of Ce and Ti in the $\text{CeO}_x/\text{TiO}_2$ nanoparticles. The spectra of Ce 3d are shown in Figure 2(a). The spectra of Ce 3d are rather complex because of the hybridization of Ce 3d and Ti 2p orbitals and splitting of the peaks [24]. The labels v and u indicate Ce $3d_{5/2}$ and $3d_{3/2}$, respectively. According

to the previous reports, u'''/v''' doublet is due to the primary photoemission from $\text{Ce}^{4+}-\text{O}_2$, and v/u and v''/u'' doublets are resulting from the transfer of one or two electrons from a filled O 2p orbital to an empty Ce 4f orbital. v'/u' doublet is due to photoemission from Ce^{3+} cations [25, 26]. The broad peak around 894.4 eV also indicates the presence of Ce^{3+} [24]. Therefore, the mixture of $\text{Ce}^{3+}/\text{Ce}^{4+}$ oxidation states exists on the surface of TiO_2 nanoparticles, which exhibited excellent characteristics in transferring charge carriers. The binding energies of $\text{Ti}2p_{1/2}$ and $2p_{3/2}$ in $\text{CeO}_x/\text{TiO}_2$ are shown in Figure 2(b). All binding energy values are about 464.4 eV and 485.8 eV, indicating that the cations exist in the form of Ti^{4+} [27]. With the increasing of Ce content, the Ti 2p binding energies do not change much. The binding energy of Ti^{3+} is lower than that of Ti^{4+} about 1.8 eV [28], which is not observed in the Ti 2p XPS spectra of the $\text{CeO}_x/\text{TiO}_2$ nanoparticles. The XPS spectra of O 1s are shown in Figure 2(c). The two peak values indicate that at least two kinds of oxygen species are present at the surface. The stronger peak about 529.6 eV is a characteristic peak of the metal oxide (Ti-O), while the wide peak about 532 eV can attribute to surface hydroxyl groups (Ti-OH) [29, 30]. The cerium content obtained by EDX in $\text{CeO}_x/\text{TiO}_2$ nanoparticles is

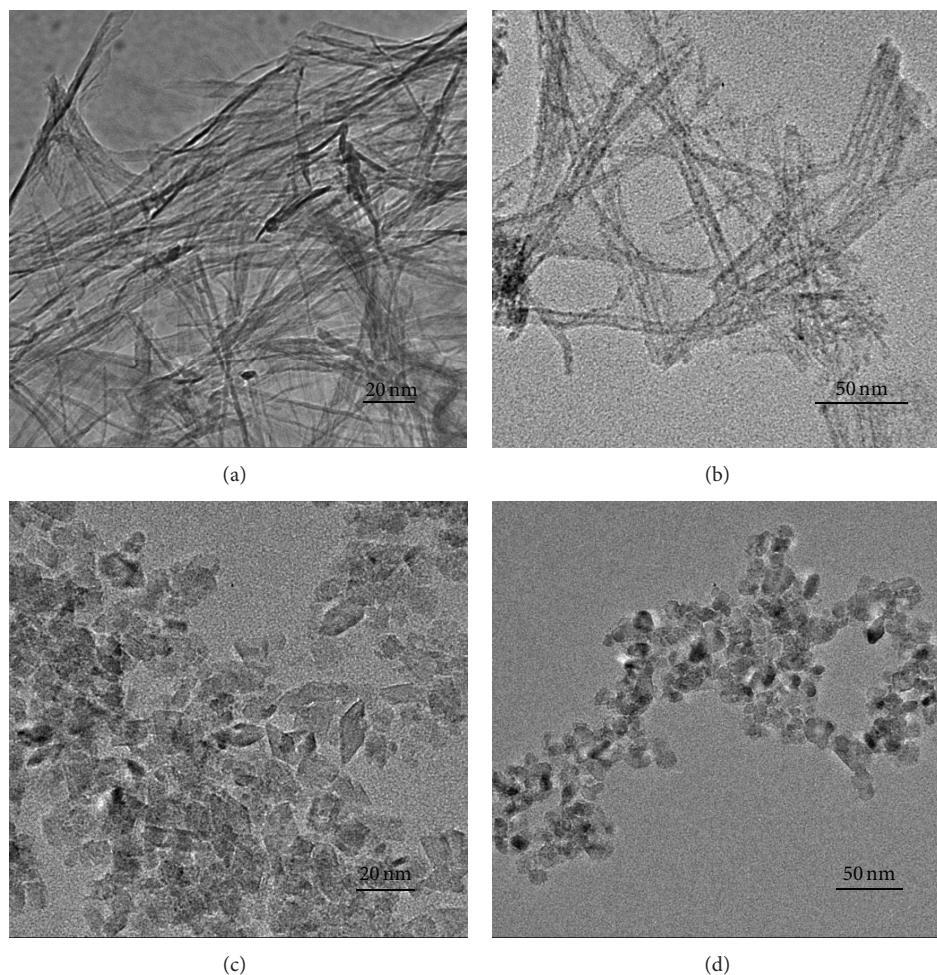


FIGURE 3: TEM images of (a) NTA; (b) NTA ion-exchanged with $\text{Ce}(\text{NO}_3)_3$; (c) 0.1% $\text{CeO}_x/\text{TiO}_2$ nanoparticles after hydrothermal method; (d) 0.1% $\text{CeO}_x/\text{TiO}_2$ nanoparticles after calcination.

listed in Table 1. With the increasing of the theory content, the actual measured content increased, and theoretical content is greater than the actual measured content; this may be due to the loss during the experiment.

The structural and morphological study was completed with the help of transmission electron microscopy technique. As shown in Figure 3, NTA displays uniform nanotube structure, the diameters of NTA are about 6–10 nm, and the surface of the nanotubes was much more smooth. Figure 3(b) indicated that the nanotubular morphology was kept after NTA was ion-exchanged with $\text{Ce}(\text{NO}_3)_3$, but some small particles were modified on the surface of NTA. After hydrothermal process, the nanotubular morphology transformed to octahedron, as shown in Figure 3(c). And the particle sizes increase and the octahedron changed to irregular particles after calcination at 400°C for 2 h. The formation process of $\text{CeO}_x/\text{TiO}_2$ nanoparticles from NTA was illustrated iconically in Figure 4.

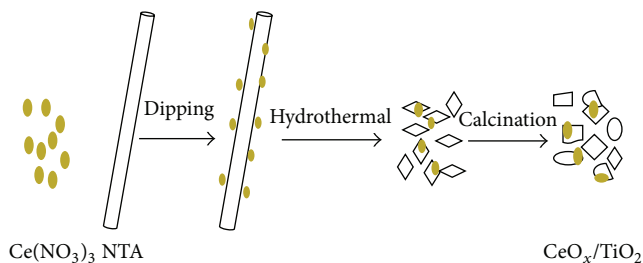
The UV-vis DRS of the as-prepared $\text{CeO}_x/\text{TiO}_2$ nanoparticles and the Degussa P25 reference are shown in Figure 5(a). By the increasing content of ceria, the UV-vis DRS of

the $\text{CeO}_x/\text{TiO}_2$ nanoparticles are significantly shifted toward visible light as compared with that of P25. We have obtained a similar result with several researches. They reported that there would have a continuous increase of absorption in the visible region (going from ca. 380 to 500 nm) with increasing ceria content of the material [12, 31, 32]. Seen from our experimental results, the absorbance edge of the $\text{CeO}_x/\text{TiO}_2$ is shifted to high wavelength when the molar ratio of Ce/Ti is increased from 0 wt% to 1 wt%, which drives an apparent modification of the band gap. The band gap energy (E_g) was calculated from the UV absorption spectra taking into account that $\alpha(E) \propto (E - E_g)^{m/2}$, where $\alpha(E)$ is the absorption coefficient for a photon of energy E and $m = 1$ for an indirect transition between bands [33]. The band gap energy is presented in Figure 5(b). This indicated that the hydrothermal-calcination method can effectively improve the optical properties.

The pore structure and surface areas of all samples are investigated by N_2 adsorption-desorption isotherm. As can be seen from Figure 6(a), all of these samples show isotherms of type IV, indicating the mesoporous structure of samples.

TABLE 1: Effect of surface area, pore diameter, pore volume and cerium atom content of $\text{CeO}_x/\text{TiO}_2$ nanoparticles.

Sample	BET surface area (m^2/g)	Pore diameter (nm)	Pore volume (cm^3/g)	Cerium atom content (%)
P25	54.89	15.22	0.27	—
0.1% $\text{CeO}_x/\text{TiO}_2$	120.92	3.88	0.31	0.11%
0.3% $\text{CeO}_x/\text{TiO}_2$	133.86	3.88	0.33	0.17%
0.5% $\text{CeO}_x/\text{TiO}_2$	139.35	3.90	0.38	0.39%
1% $\text{CeO}_x/\text{TiO}_2$	137.22	3.88	0.34	0.77%

FIGURE 4: Formation schematic diagram of $\text{CeO}_x/\text{TiO}_2$ nanoparticles.

The corresponding hysteresis loops are type H3 at a high relative pressure range of 0.75–1.0, suggesting the presence of slit-like pores [34, 35]. The generation of hysteresis loops is from the aggregation of the sheet-like TiO_2 nanoparticles. This result is also consistent with TEM images. In Figure 6(b), the pore distribution of 0.1% to 1% $\text{CeO}_x/\text{TiO}_2$ is in the range of 2–6 nm. The detailed BET surface area and pore volume for these samples are shown in Table 1. The series of $\text{CeO}_x/\text{TiO}_2$ nanoparticles prepared by NTA as precursor have large surface areas, which range from 120 to 137 $\text{m}^2 \text{g}^{-1}$, while P25 only has 54 $\text{m}^2 \text{g}^{-1}$. These large surface areas could provide much more adsorption sites for pollutant molecules, which is advantageous for improving the photocatalytic activity of the samples.

Photodegradation of MB was used as the probe reaction to evaluate the photocatalytic activity of samples under visible light irradiation (Figure 7(a)). All the $\text{CeO}_x/\text{TiO}_2$ samples showed relatively higher activities as compared with P25. The reason for this result may have three points as follows. The first one is that the samples prepared by NTA as precursor have relative larger BET surface area. This can have much more adsorption sites for MB on the sample surface. The second is CeO_x , which enhanced the visible absorption of the samples. And the last one is Ce element existing as a mixture of $\text{Ce}^{3+}/\text{Ce}^{4+}$ oxidation states, which can act as the electron acceptor for the photogenerated charge carriers, thereby improving the separation efficiency of the electron-hole pair. In particular, 0.1% $\text{CeO}_x/\text{TiO}_2$ exhibits the best photocatalytic activity, having a photodegradation yield of ca. 68% for MB dye. The stability of 0.1% $\text{CeO}_x/\text{TiO}_2$ on the photodegradation reaction was investigated. As shown in Figure 7(b), the degradation yield of MB on 0.1% $\text{CeO}_x/\text{TiO}_2$ had no significant difference in the consecutive three cycles. Therefore, 0.1% $\text{CeO}_x/\text{TiO}_2$ showed a very good stability in the degradation of MB.

With the increase of the doping amount with Ce, the photodegradation yield of MB decreased. In order to clarify the reasons for this result, the active species in photodegradation process of MB were detected. Methanol and silver nitrate solution were added into MB dyes solution to capture electrons and holes, respectively. As can be seen from Figure 7(c), the degradation yield of MB decreased to a certain extent when the electrons or holes were captured. And more significant change of activity decreased largely when the electrons were eliminated. So we speculated that both electrons and holes are involved in the photocatalytic degradation of MB dyes, and the contributions of electrons are larger than that of holes.

Based on the above experimental results, a possible mechanism for MB degradation on $\text{CeO}_x/\text{TiO}_2$ samples was proposed in Figure 8. Under visible light irradiation, the electrons can be excited from the valence band (VB) of Ce modified titania samples into conduction band (CB) and holes are left in the valence band. Ce element existed as a mixture of $\text{Ce}^{3+}/\text{Ce}^{4+}$ oxidation states. The Ce^{4+} can act as the electron acceptor for the photogenerated charge carriers. So, the separation efficiency of the electron-hole pair can be improved. For the pure titania, both electrons and holes participate in photodegradation of MB organic pollutants. The excited electrons react with the adsorbed oxygen to form oxidizing species. MB was mineralized into carbon dioxide and water by the oxidizing species as well as holes. While part of the excited electrons would be trapped by Ce 4f orbitals, and cannot participate in the photocatalytic reaction. And the others not trapped by Ce and the holes would participate in the photocatalytic reaction (as shown in Figure 8); we come to the conclusion that the electrons play a predominance role in the progress of photodegradation of MB organic pollutants. So the electrons trapped by Ce 4f orbitals decrease the photocatalytic activity.

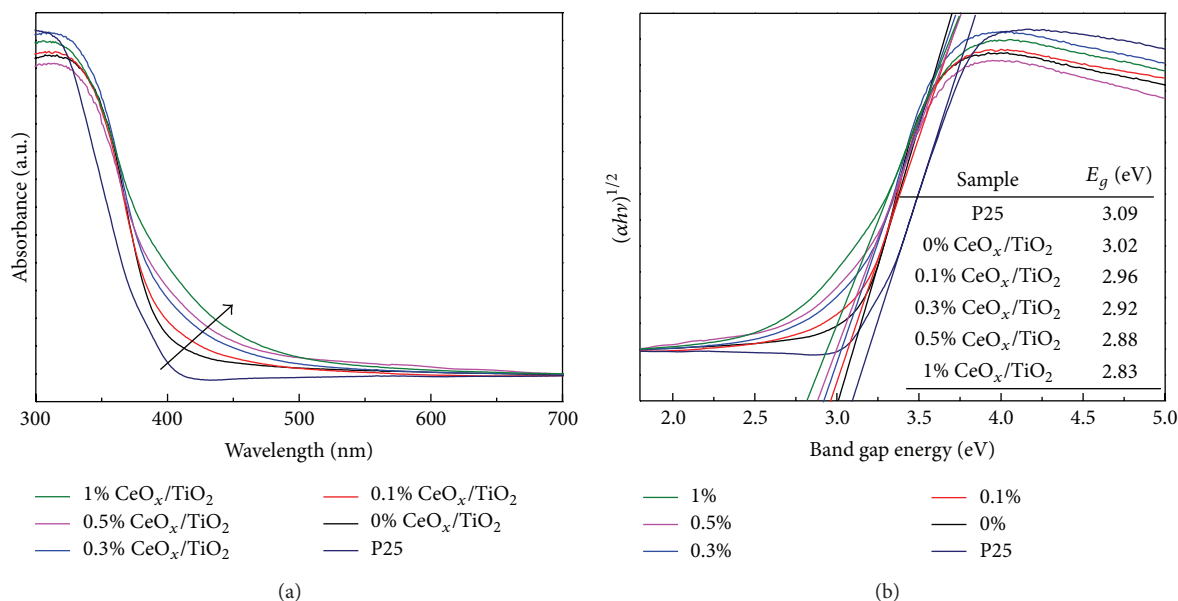


FIGURE 5: (a) UV-vis DRS of P25 and the $x\%$ $\text{CeO}_x/\text{TiO}_2$ nanoparticles; (b) the plot of band gap energy and $(\alpha h\nu)^{1/2}$ of P25 and $\text{CeO}_x/\text{TiO}_2$ nanoparticles.

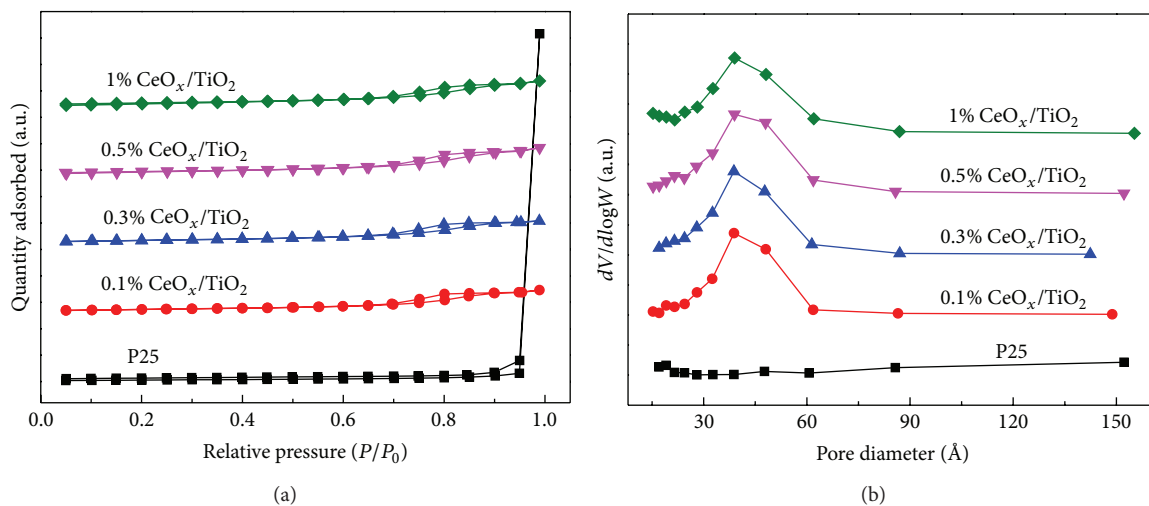


FIGURE 6: (a) Nitrogen adsorption-desorption isotherms of P25 and $x\%$ $\text{CeO}_x/\text{TiO}_2$ nanoparticles; (b) BJH pore-size distributions of P25 and $x\%$ $\text{CeO}_x/\text{TiO}_2$ nanoparticles.

Besides MB, the colorless 4-chlorophenol (4-CP) was also selected as a model pollutant. The results were shown in Figure 7(d). Compared with P25, 0.1% $\text{CeO}_x/\text{TiO}_2$ showed much higher photocatalytic activity after irradiating for 6 h. The photodegradation yield of 4-CP on 0.1% $\text{CeO}_x/\text{TiO}_2$ reached ca. 79%, while the degradation yield on P25 was only 40%.

4. Conclusions

Mesostructured $\text{CeO}_x/\text{TiO}_2$ nanoparticles with different Ce contents have been successfully synthesized using titanate nanotubes as precursor by hydrothermal-calcination

method. Fine-crystallized $\text{CeO}_x/\text{TiO}_2$ could be obtained and crystal size was about 8–12 nm. And the Ce did not incorporate into the lattice of TiO_2 , which just existed as the cerium oxide modified on the surface of TiO_2 . XPS results indicated that Ce species were in the form of Ce^{3+} and Ce^{4+} . TEM images presented that the NTA nanotubes have transformed to TiO_2 nanoparticles completely. Introduction of Ce species can effectively extend the spectral response from UV to visible area of TiO_2 . N_2 adsorption-desorption analysis revealed that all the samples belonged to mesoporous structure and had large surface area. All the $\text{CeO}_x/\text{TiO}_2$ nanoparticles showed much higher photocatalytic activity compared with P25 in the degradation of MB aqueous

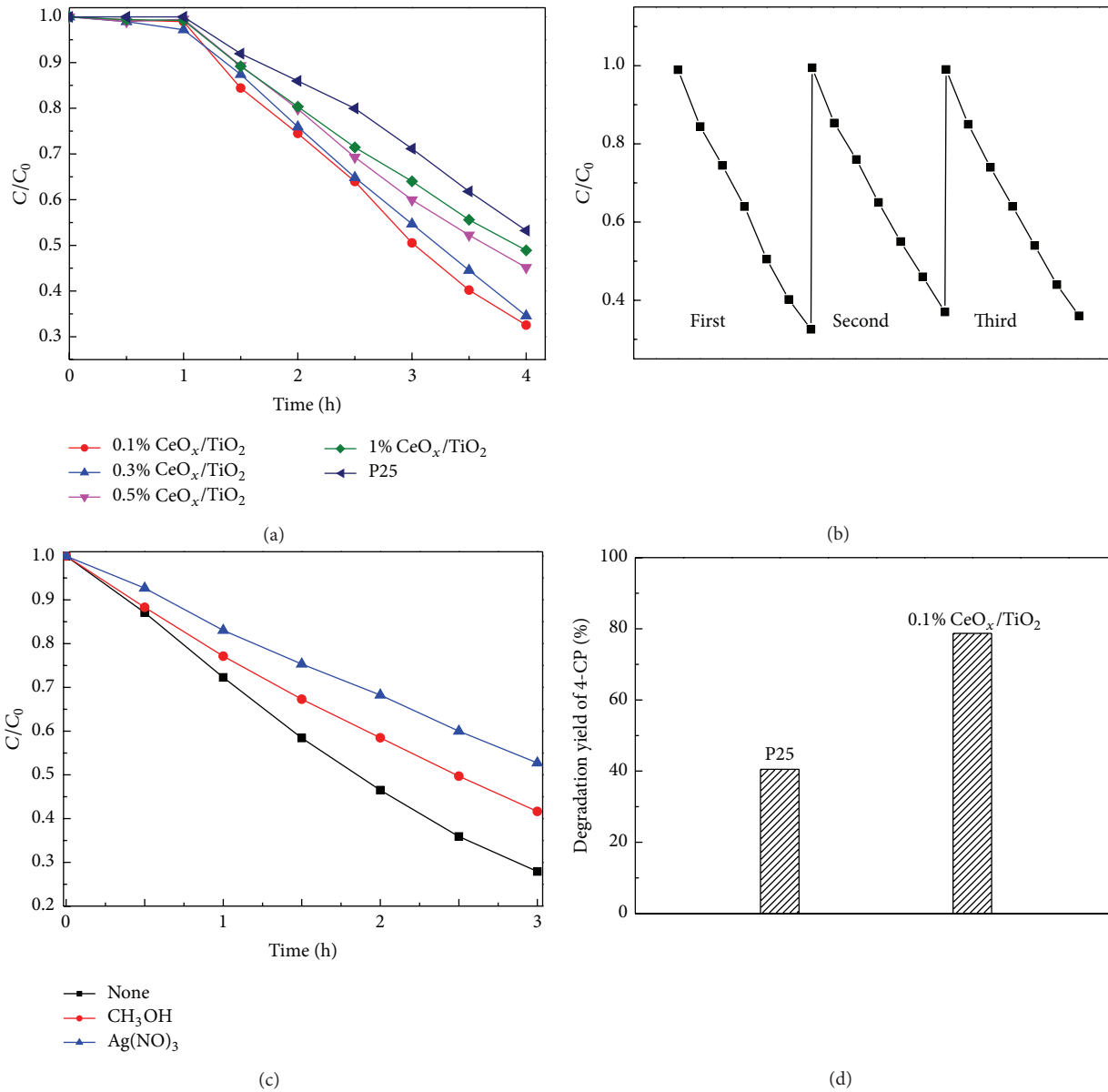


FIGURE 7: Photocatalytic activity for MB (a) and stability (b) of P25 and $x\% CeO_x/TiO_2$ nanoparticles; (c) detection of the active species of electrons and holes; (d) photocatalytic degradation yield of 4-CP on P25 and 0.1% CeO_x/TiO_2 nanoparticles.

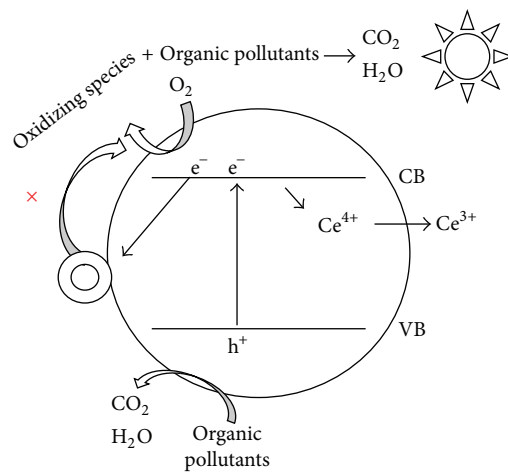


FIGURE 8: The proposed photocatalytic mechanism of CeO_x/TiO_2 nanoparticles for the degradation of MB under visible light.

solution under the visible irradiation, especially for the 0.1% CeO_x/TiO₂ samples. As the Ce content increases, the degradation yield of MB decreased gradually, which should be due to the capture of electrons by Ce⁴⁺.

Conflict of Interests

The authors declare that there is no conflict of interests regarding the publication of this paper.

Acknowledgments

The authors gratefully acknowledge the support of the National Natural Science Foundation of China (nos. 21103042, 21471047, 20973054, and 21203054), Program for Changjiang Scholars and Innovation Research Team in University (no. PCS IRT1126), and the Specialized Research Fund for the Doctoral Program of Higher Education (no. 20114103120001).

References

- [1] J. Zhang, Z. Zhao, X. Wang et al., "Increasing the oxygen vacancy density on the TiO₂ surface by La-doping for dye-sensitized solar cells," *The Journal of Physical Chemistry C*, vol. 114, no. 43, pp. 18396–18400, 2010.
- [2] W. Tu, Y. Zhou, Q. Liu et al., "An in situ simultaneous reduction-hydrolysis technique for fabrication of TiO₂-graphene 2D sandwich-like hybrid nanosheets: graphene-promoted selectivity of photocatalytic-driven hydrogenation and coupling of CO₂ into methane and ethane," *Advanced Functional Materials*, vol. 23, no. 14, pp. 1743–1749, 2013.
- [3] T. L. Thompson and J. T. Yates Jr., "Surface science studies of the photoactivation of TiO₂—new photochemical processes," *Chemical Reviews*, vol. 106, no. 10, pp. 4428–4453, 2006.
- [4] X. Chen and S. S. Mao, "Titanium dioxide nanomaterials: synthesis, properties, modifications and applications," *Chemical Reviews*, vol. 107, no. 7, pp. 2891–2959, 2007.
- [5] G. Dagan and M. Tomkiewicz, "Titanium dioxide aerogels for photocatalytic decontamination of aquatic environments," *Journal of Physical Chemistry*, vol. 97, no. 49, pp. 12651–12655, 1993.
- [6] Z. G. Zou, J. H. Ye, K. Sayama, and H. Arakawa, "Direct splitting of water under visible light irradiation with an oxide semiconductor photocatalyst," *Nature*, vol. 414, no. 6864, pp. 625–627, 2001.
- [7] Y. Cao, T. He, L. Zhao, E. Wang, and W. Yang, "Structure and phase transition behavior of Sn⁴⁺-doped TiO₂ nanoparticles," *Journal of Physical Chemistry C*, vol. 113, no. 42, pp. 18121–18124, 2009.
- [8] J. Zhu, W. Zheng, B. He, J. Zhang, and M. Anpo, "Characterization of Fe-TiO₂ photocatalysts synthesized by hydrothermal method and their photocatalytic reactivity for photodegradation of XRG dye diluted in water," *Journal of Molecular Catalysis A: Chemical*, vol. 216, no. 1, pp. 35–43, 2004.
- [9] M. A. Debeila, N. J. Coville, M. S. Scurrill, and G. R. Hearne, "The effect of calcination temperature on the adsorption of nitric oxide on Au-TiO₂: drifts studies," *Applied Catalysis A: General*, vol. 291, no. 1-2, pp. 98–115, 2005.
- [10] W. Ren, Z. Ai, F. Jia, L. Zhang, X. Fan, and Z. Zou, "Low temperature preparation and visible light photocatalytic activity of mesoporous carbon-doped crystalline TiO₂," *Applied Catalysis B: Environmental*, vol. 69, no. 3-4, pp. 138–144, 2007.
- [11] M. D. Hernández-Alonso, A. B. Hungria, A. Martínez-Arias et al., "Confinement effects in quasi-stoichiometric CeO₂ nanoparticles," *Physical Chemistry Chemical Physics*, vol. 6, no. 13, pp. 3524–3529, 2004.
- [12] P. Ji, J. Zhang, F. Chen, and M. Anpo, "Study of adsorption and degradation of acid orange 7 on the surface of CeO₂ under visible light irradiation," *Applied Catalysis B: Environmental*, vol. 85, no. 3-4, pp. 148–154, 2009.
- [13] M. D. Hernández-Alonso, A. B. Hungria, A. Martínez-Arias et al., "EPR study of the photoassisted formation of radicals on CeO₂ nanoparticles employed for toluene photooxidation," *Applied Catalysis B: Environmental*, vol. 50, no. 3, pp. 167–175, 2004.
- [14] G. Xiao, X. Huang, X. P. Liao, and B. Shi, "One-pot facile synthesis of cerium-doped TiO₂ mesoporous nanofibers using collagen fiber as the biotemplate and its application in visible light photocatalysis," *Journal of Physical Chemistry C*, vol. 117, no. 19, pp. 9739–9746, 2013.
- [15] Y. H. Xu, H. R. Chen, Z. X. Zeng, and B. Lei, "Investigation on mechanism of photocatalytic activity enhancement of nanometer cerium-doped titania," *Applied Surface Science*, vol. 252, no. 24, pp. 8565–8570, 2006.
- [16] G. Li, D. Zhang, and J. C. Yu, "Thermally stable ordered mesoporous CeO₂/TiO₂ visible-light photocatalysts," *Physical Chemistry Chemical Physics*, vol. 11, no. 19, pp. 3775–3782, 2009.
- [17] R. Nakamura, A. Okamoto, H. Osawa, H. Irie, and K. Hashimoto, "Design of all-inorganic molecular-based photocatalysts sensitive to visible light: Ti(IV)-O-Ce(III) bimetallic assemblies on mesoporous silica," *Journal of the American Chemical Society*, vol. 129, no. 31, pp. 9596–9597, 2007.
- [18] B. C. Viana, O. P. Ferreira, A. G. Souza Filho et al., "Decorating titanate nanotubes with CeO₂ nanoparticles," *The Journal of Physical Chemistry C*, vol. 113, no. 47, pp. 20234–20239, 2009.
- [19] Q. Li, R. Li, Y. Xing, L. Zong, and J. Yang, "Incorporation of Sn²⁺ into titanic acid nanotubes and investigation of their visible-light-responsive photocatalytic activity," *Science of Advanced Materials*, vol. 5, no. 3, pp. 227–232, 2013.
- [20] Y. Xing, R. Li, Q. Li, and J. Yang, "A new method of preparation of AgBr/TiO₂ composites and investigation of their photocatalytic activity," *Journal of Nanoparticle Research*, vol. 14, no. 12, article 1284, 2012.
- [21] J. Yang, Z. Jin, X. Wang et al., "Study on composition, structure and formation process of nanotube Na₂Ti₂O₄(OH)₂," *Journal of the Chemical Society. Dalton Transactions*, no. 20, pp. 3898–3901, 2003.
- [22] Q. Y. Li, L. L. Zong, Y. Y. Xing, X. Wang, L. Yu, and J. Yang, "Preparation of g-C₃N₄/TiO₂ nanocomposites and investigation of their photocatalytic activity," *Science of Advanced Materials*, vol. 5, no. 9, pp. 1316–1322, 2013.
- [23] M. Zhang, Z. Jin, J. Zhang et al., "Effect of annealing temperature on morphology, structure and photocatalytic behavior of nanotubed H₂Ti₂O₄(OH)₂," *Journal of Molecular Catalysis A: Chemical*, vol. 217, no. 1-2, pp. 203–210, 2004.
- [24] M. Nasir, Z. Xi, M. Xing et al., "Study of synergistic effect of Ce- and S-codoping on the enhancement of visible-light photocatalytic activity of TiO₂," *The Journal of Physical Chemistry C*, vol. 117, no. 18, pp. 9520–9528, 2013.

- [25] H. Liu, M. Wang, Y. Wang, Y. Liang, W. Cao, and Y. Su, "Ionic liquid-templated synthesis of mesoporous CeO₂-TiO₂ nanoparticles and their enhanced photocatalytic activities under UV or visible light," *Journal of Photochemistry and Photobiology A: Chemistry*, vol. 223, no. 2-3, pp. 157-164, 2011.
- [26] B. M. Reddy, A. K. Khan, Y. Yamada, T. Kobayashi, S. Loidant, and J.-C. Volta, "Structural characterization of CeO₂-TiO₂ and V₂O₅/CeO₂-TiO₂ catalysts by Raman and XPS techniques," *The Journal of Physical Chemistry B*, vol. 107, no. 22, pp. 5162-5167, 2003.
- [27] X. Gao, Y. Jiang, Y. Zhong, Z. Luo, and K. Cen, "The activity and characterization of CeO₂-TiO₂ catalysts prepared by the sol-gel method for selective catalytic reduction of NO with NH₃," *Journal of Hazardous Materials*, vol. 174, no. 1-3, pp. 734-739, 2010.
- [28] N. J. Price, J. B. Reitz, R. J. Madix, and E. I. Solomon, "A synchrotron XPS study of the vanadia-titania system as a model for monolayer oxide catalysts," *Journal of Electron Spectroscopy and Related Phenomena*, vol. 98-99, pp. 257-266, 1999.
- [29] J. Fang, X. Bi, D. Si, Z. Jiang, and W. Huang, "Spectroscopic studies of interfacial structures of CeO₂-TiO₂ mixed oxides," *Applied Surface Science*, vol. 253, no. 22, pp. 8952-8961, 2007.
- [30] S. K. Parayil, H. S. Kibombo, C. M. Wu et al., "Synthesis-dependent oxidation state of platinum on TiO₂ and their influences on the solar simulated photocatalytic hydrogen production from water," *Journal of Physical Chemistry C*, vol. 117, no. 33, pp. 16850-16862, 2013.
- [31] S. V. N. T. Kuchibhatla, A. S. Karakoti, D. R. Baer et al., "Influence of aging and environment on nanoparticle chemistry: implication to confinement effects in nanoceria," *The Journal of Physical Chemistry C*, vol. 116, no. 26, pp. 14108-14114, 2012.
- [32] M. Palumbo, G. Giorgi, L. Chiodo, A. Rubio, and K. Yamashita, "The nature of radiative transitions in TiO₂-based nanosheets," *The Journal of Physical Chemistry C*, vol. 116, no. 34, pp. 18495-18503, 2012.
- [33] A. E. Jiménez González and S. Gelover Santiago, "Structural and optoelectronic characterization of TiO₂ films prepared using the sol-gel technique," *Semiconductor Science and Technology*, vol. 22, no. 7, pp. 709-716, 2007.
- [34] K. Lv, Q. Xiang, and J. Yu, "Effect of calcination temperature on morphology and photocatalytic activity of anatase TiO₂ nanosheets with exposed 001 facets," *Applied Catalysis B: Environmental*, vol. 104, no. 3-4, pp. 275-281, 2011.
- [35] L. C. Liu, Z. Y. Ji, W. X. Zou et al., "In situ loading transition metal oxide clusters on TiO₂ nanosheets as co-catalysts for exceptional high photoactivity," *ACS Catalysis*, vol. 3, no. 9, pp. 2052-2061, 2013.

Research Article

Bottom-Up Enhancement of $g\text{-C}_3\text{N}_4$ Photocatalytic H_2 Evolution Utilising Disordering Intermolecular Interactions of Precursor

Xue Lu Wang,^{1,2} Wen Qi Fang,¹ Yu Hang Li,¹ Pengfei Liu,¹ Haimin Zhang,²
Yun Wang,² Porun Liu,² Yefeng Yao,³ Huijun Zhao,² and Hua Gui Yang^{1,2}

¹ Key Laboratory for Ultrafine Materials of Ministry of Education, School of Materials Science and Engineering, East China University of Science and Technology, 130 Meilong Road, Shanghai 200237, China

² Centre for Clean Environment and Energy, Griffith University, Gold Coast Campus, Gold Coast, QLD 4222, Australia

³ Physics Department and Shanghai Key Laboratory of Magnetic Resonance, East China Normal University, Shanghai 200062, China

Correspondence should be addressed to Huijun Zhao; h.zhao@griffith.edu.au and Hua Gui Yang; hgyang@ecust.edu.cn

Received 9 June 2014; Revised 20 August 2014; Accepted 8 September 2014; Published 30 November 2014

Academic Editor: Wenjun Luo

Copyright © 2014 Xue Lu Wang et al. This is an open access article distributed under the Creative Commons Attribution License, which permits unrestricted use, distribution, and reproduction in any medium, provided the original work is properly cited.

Disordered intermolecular interaction carbon nitride precursor prepared by water-assisted grinding of dicyandiamide was used for synthesis of $g\text{-C}_3\text{N}_4$. The final sample possesses much looser structure and provides a broadening optical window for effective light harvesting and charge separation efficiency, which exhibits significantly improved H_2 evolution by photocatalytic water splitting. The bottom-up mechanochemistry method opens new vistas towards the potential applications of weak interactions in the photocatalysis field and may also stimulate novel ideas completely different from traditional ones for the design and optimization of photocatalysts.

1. Introduction

Spurred by the increasing global energy demands and environmental issues, a noble pathway for converting solar energy into clean fuels has been widely recognised. Among various types of solar energy conversion, solar chemical conversion such as photolysis of water into hydrogen (H_2) has been regarded as a promising way to transfer biological photosynthesis to a manmade environment with a higher efficiency than plants [1, 2]. Thus, considerable efforts have been devoted to exploring robust photocatalytic systems for the purpose of efficient absorption, utilization, and conversion of solar photons in a sustainable manner [3, 4]. However, low light utilisation efficiency and high recombination of photogenerated carriers in most photocatalytic systems limit the applicability of photocatalysts for large-scale H_2 photosynthesis. Recently, organic polymer or supermolecular systems, which are much closer to the nature plant, have been introduced as solar-photons transducers and stimulated continuous research attentions [5, 6].

Polymeric graphitic carbon nitride ($g\text{-C}_3\text{N}_4$), a simple, efficient, highly stable, and sustainable organic material, has been introduced as a metal-free visible light photocatalyst for water splitting and attracted worldwide renaissance attention [4]. To improve the photocatalytic activities of $g\text{-C}_3\text{N}_4$, several strategies have been developed, such as doping [7–10], templating [11–13], cocatalyzing [14, 15], copolymerization [16, 17], heterogeneous catalysis [18, 19], and surface modification [20, 21]. In general, bulk $g\text{-C}_3\text{N}_4$ was synthesized by pyrolysis of nitrogen-rich organic precursors, such as cyanamide [4], dicyandiamide [14], melamine [11], ammonium thiocyanate [22], urea [23], and thiourea [24]. Nevertheless, most of the precursors involved in the synthetic process are crystallographic materials, and researchers considered only structures and functions involving strong covalent bonds. Instead, the structures of these organic precursors are usually made from loose aggregates that are held together by weak, noncovalent interactions, which are responsible for most of the processes occurring in living systems because of their dynamic nature [25–27]. As we

know, mechanochemical reaction such as ball mill grinding can break up the materials to expose fresh surfaces, introduce various defects, and eventually result in amorphization [28]. The crystal structures of organic solids which are very different in many respects from inorganic materials especially are usually anisotropic, and the shapes and the intermolecular interactions of organic particles are far from being isometric and different crystal faces have different properties [28]. Thus, new routes for the synthesis of compounds will be opened if we preprocess the precursors by mechanical action.

Herein, we for the first time developed a bottom-up strategy to synthesize $g\text{-C}_3\text{N}_4$ photocatalysts with improved optical property and chemical structure through using disordered dicyandiamide (D-DCDA) as reaction precursor. The D-DCDA was obtained by water-assisted grinding (WAG) of crystallographic dicyandiamide (DCDA). The final carbon nitride sample (D-CN) condensed by D-DCDA possesses much looser structure and provides a broadening optical window for effective light harvesting and charge separation efficiency which results in the significant enhancement in photocatalytic activity for hydrogen evolution.

2. Material and Methods

2.1. Materials Synthesis. The D-DCDA precursor was carried out in a planetary ball-mill machine (QM-3SP2) in the presence of deionized (DI) water. In a typical fabrication, 2 g of DCDA powders was added into an agate capsule containing agate balls of 5 mm in diameter. 10 mL of DI water was added into the above capsule as solvents assisted grinding. The container was fixed in the planetary ball-mill machine and agitated with 300 rpm for 12 h. The result products were collected by centrifugation with DI water and dried at 80 °C under vacuum for 24 h.

The D-CN sample was prepared by a facile thermal treatment of D-DCDA. Typically, 1 g of the as-prepared D-DCDA powder was put into a covered crucible and then heated at a rate of 5 °C min⁻¹ to reach the temperature of 550 °C and maintained at this temperature in air for 2 h. The samples obtained by simply heating DCDA at 550 °C were denoted by CN and were used as a reference sample.

2.2. Methods. The structures of the power samples were investigated by X-ray diffractometer (XRD, Bruker D8 Advanced Diffractometer operating with Cu K α radiation). The angular range was $2\theta = 5\text{--}75^\circ$, with a speed of 6°/min. Infrared transmission was obtained with a Fourier transform infrared (FTIR) spectrophotometer Spectrum (Nicolet). The optical absorbance spectra of the samples were performed on using a UV-vis spectrometer (CARY 300). All binding energies were referenced to C1s peaks (284.8 eV) arising from surface hydrocarbons (or possible adventitious hydrocarbon). Element analysis was conducted by an elemental analyzer (vario ELII; Elementar Analysensysteme, Germany). The photoluminescence measurements were performed in an Edinburgh instruments (FLSP 920) system operated at room temperature. The carbon and nitrogen K-edge X-ray absorption near-edge structure (XANES) measurement of

the samples were performed at the beamline 4B7B of Beijing Synchrotron Radiation Facility (BSRF). Brunauer-Emmett-Teller (BET) surface areas were determined by a TriStar 3020 nitrogen sorption isotherm apparatus.

3. Results

The possible mechanism diagrams of the synthesis of D-DCDA and D-CN are illustrated in Figure 1(a). After ball milling DCDA in the presence of deionized water, the parking patterns of the crystal structure of DCDA molecules become disordered owing to the introduction of water molecules by the stronger hydrogen bond [29, 30]. Chemical structures of D-DCDA were characterized with various techniques such as XRD, FTIR, and solid-state NMR. Figure 1(b) exhibits the XRD patterns of the DCDA and D-DCDA samples. The position of the main peaks of the two samples is almost same. However, the intensities of peaks sharply decrease after WAG of the DCDA, which indicates the deterioration of crystallinity which led to the destroyed molecules framework or disordered arrangement of molecules units. More structural properties of the D-DCDA were further characterized by SEM, FTIR and ¹³C solid-state NMR measurements. As can be seen from Figure S1, (see Figure S1 at Supplementary Material available online at <http://dx.doi.org/10.1155/2014/149520>) after the ball milling treatment, the particle size of DCDA decreased to about 1/10 of the original one. Figure 1(c) and S2 show that the FTIR and NMR spectra of the D-DCDA and DCDA are similar, suggesting that the composition monomer units of the D-DCDA remain unchanged compared with those of the DCDA. Thus, the possible destruction of surface functional groups and the covalent intramolecular bonds can be ruled out.

In order to understand the possible reaction process during pyrolysis of DCDA and D-DCDA, TG and DSC were carried out. As can be seen from the mass-loss curve (Figure 1(d)), most activities occur in the range of 210–720 °C. For D-DCDA, a slowed weight loss tendency is observed, which can be assigned to the less sublimation and evaporation of some small molecules derived from the pyrolysis; that is, more molecules are involved in the real reaction progress [31]. In addition, there is still 6.48 wt.% of residuals above 700 °C for D-DCDA, which would be due to the formation of stable C species at high temperature [32, 33]. Therefore, the final product D-CN may exist as some nitrogen defect or structure distortion compared to the CN sample. Figure 1(e) shows the DSC curves of the two precursors. An endothermic peak at around 213 °C is the melting point of them [34]. However, it seems that D-DCDA has the lower melting point. Ordinary, melting-point depression is the phenomenon of reduction of the melting point of a material with reduction of its size, which is accompanied with some lattice distortion. These accord well with the results obtained by XRD. Subsequently, the first strong exothermic peak is at about 237 °C, which indicated that sample starts to decompose and aggregate into melamine [4, 31]. Interestingly, another new exothermic peak appears at 255 °C for the D-DCDA, which means D-DCDA undergoing two exothermic reactions during the formation

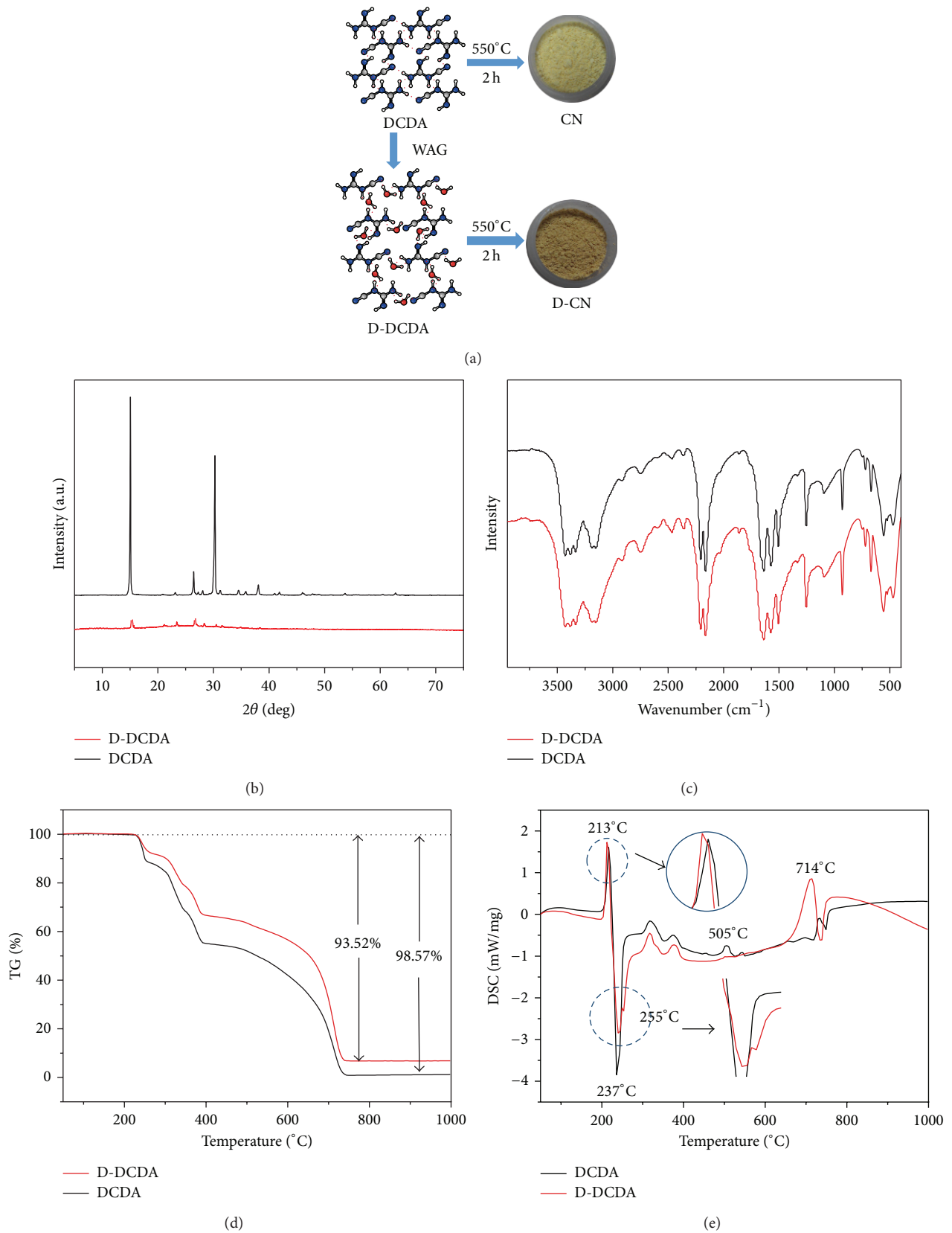


FIGURE 1: (a) Schematic illustration for the synthesis process of CN and D-CN. (b) XRD patterns, (c) FTIR spectra, (d) TG curves, and (e) DSC curves of the DCDA and D-DCDA samples.

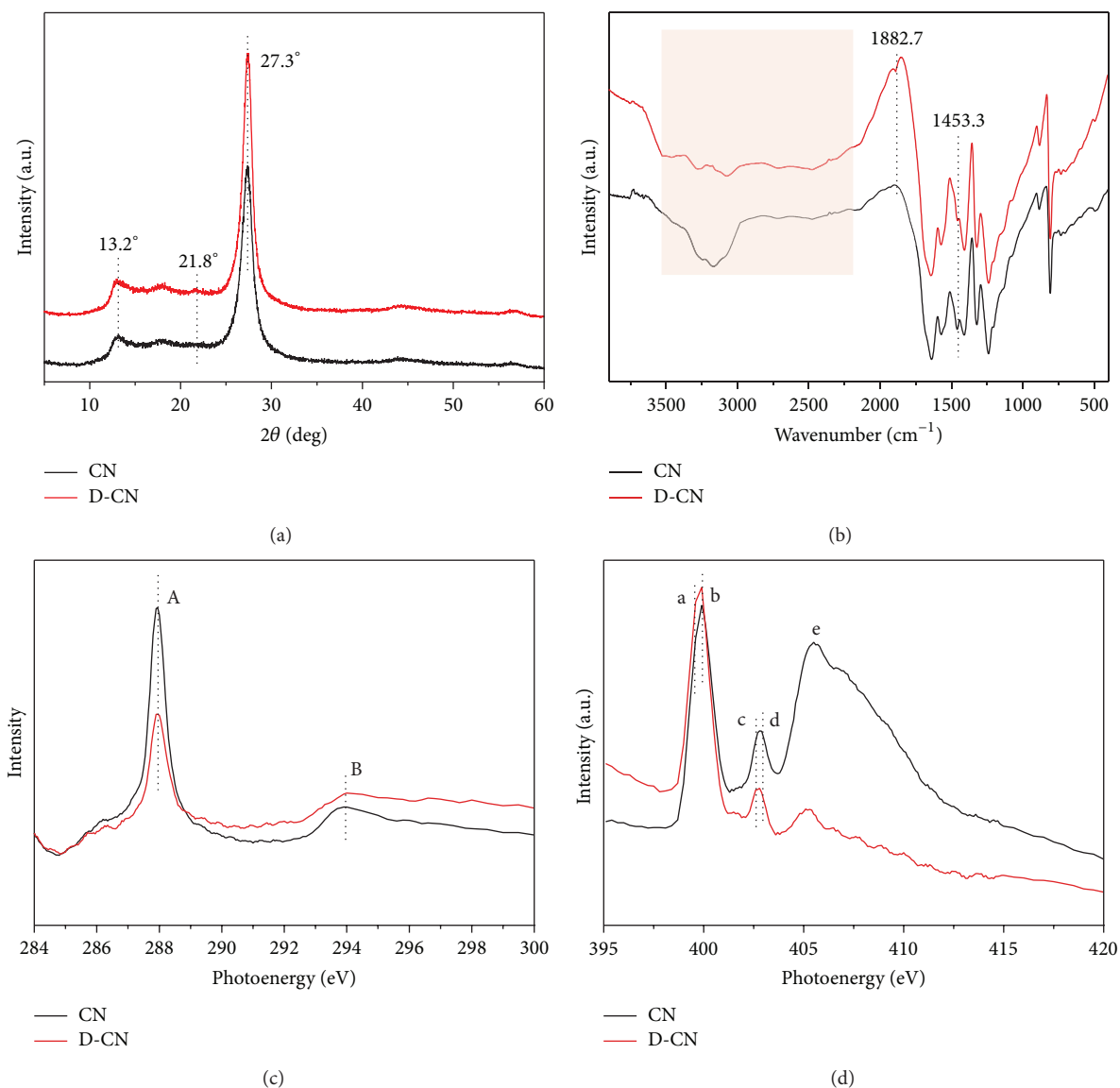


FIGURE 2: Comparison of XRD patterns (a), FTIR spectra (b), C K-edge (c), and N K-edge (d) XANES spectra of CN and D-CN.

of melamine, leading to the different degrees of condensation and different packing motifs. Finally, the endothermic peak at 714°C can be attributed to the sublimation of carbon nitride [31, 34]. The earlier decomposition point for D-DCDA further proves the incomplete structure.

To shed light on the effect of disordering of precursors on the performance of the final $g\text{-C}_3\text{N}_4$ products, various characterizations have been conducted. The carbon and nitrogen stoichiometry of prepared samples were determined by elemental analysis. As shown in Table S1, the C/N atomic ratio of the D-CN was determined as 0.676, which is very close to the bulk CN (0.675) but lower than that of the theoretical value of the ideal crystal $g\text{-C}_3\text{N}_4$ (0.75). Trace amounts of other compositions may be caused by absorbed H_2O and substituted oxygen. The XRD patterns of CN and D-CN samples are quite similar, which represent their graphitic like structures stacked by tri-s-triazine based connection

sheet as units. They all show two feature diffraction peaks at around 13.2° and 27.3°, characteristic of the interplanar structural repeating motifs and the stacking peak of conjugated aromatic systems, respectively [4]. However, a small new peak appears at 21.8° for D-CN and may originate from the defective condensation of melon structures [5].

The bonding of carbon and nitrogen of the final samples was analysed through FTIR spectra (Figure 2(b)). In the case of bulk CN, the set of peaks between 1700 and 1200 cm^{-1} is characteristic of organic molecules containing tri-s-triazine ring moieties, while the sharp peak at around 810 cm^{-1} is considered as their breathing mode. Additionally, the absorbance in the region of 3000–3500 cm^{-1} is assignable to the presence of secondary and primary amines and the O–H band which is originated from the uncondensed amino groups and adsorbed H_2O molecules, respectively. The obvious widen tendency of D-CN also implies the defective condensation.

In addition, besides the similar skeleton signs, some minute distinctions can be observed on the D-CN sample. To be specific, the peak at around 1453 cm^{-1} which is attributable to a network structure of triazine rings cross-linked with NH end and $>\text{N}$ -groups becomes weak and less developed [18, 20]. A small peak of D-CN at around 1883 cm^{-1} may be related to the C=O stretching induced by unavoidable oxidation from the D-DCDA. All these observations speak for the formation of a more defected polymeric network of $g\text{-C}_3\text{N}_4$ for D-CN compared to CN.

The chemical structures of the samples were further analysed by XPS measurements. The C1s spectra in Figure S3A can be deconvoluted into three peaks at 284.7, 288.2, and 289.4 eV, which are assigned to the sp^2 C-C bonds, N=C-N, and C-O groups induced by unavoidable oxidation, respectively. Additionally, there are three nitrogen species present in the N1s spectrum (Figure S3B) centred at 398.6, 399.6, and 401.1 eV, corresponding to C-N=C, N-(C)₃ and C-N-H, respectively. Among them, the ratio of N-(C)₃ decreases for D-CN compared with CN. From these observations, we deduce that the aromatic unit of D-CN was more incomplete than CN, in particular, the broken of cross-linked nitrogen in D-CN might lead to the nitrogen loss and formation of C=O bond, which is in good agreement with the FTIR analysis.

To get further insight into the intrinsic structure of the CN and D-CN, we then examined the C and N K-edge XAENES spectra. Looking at the C K-edge XANES spectra in Figure 2(c), the samples both exhibit two distinct peaks at ~ 287.9 (A) and ~ 294 eV (B). The signal A corresponds to the sp^2 -hybridized carbon in N-containing aromatic rings (N=C=N), which is the major carbon species in the $g\text{-C}_3\text{N}_4$ polymer. In addition, its intensity for the D-CN sample is found to be lower than that of bulk CN, indicating the deterioration of crystallinity, reduction of polymerization degree, or defective spatial structure. On the other hand, the feature B is related to interlayer states or transitions to sp^3 hybridized states [35].

Figure 2(d) shows the N K-edge XANES spectra of the samples. CN and D-CN both exhibit at least five peaks. The neighbouring peaks a and b at around 399.5 and 400.0 eV can be identified as the unoccupied π^* orbitals in pyridine-like C=N-C bonds and the graphitic-type N, respectively. Both of them, together with sp^2 hybridized C (N=C=N), make up the heptazine heterocyclic ring (C_6N_7) units for the construction of the basic substructural units of the $g\text{-C}_3\text{N}_4$ polymer. Another two adjacent peaks are centered at 402.6 and 403.0 eV, which are attributable to the amino-type N and the pyrrolic-type N, respectively [36]. Furthermore, a strongly weakened tendency appeared at the D-CN compared with the CN in the σ^* region of the N K-edge (region e), and a $1s \rightarrow \sigma^*$ transition is observed as a broad feature centered at ~ 407 eV which is a superposition of graphite-type N and pyridine-like N structures and sensitive to the bond length between N and C [37].

The N_2 adsorption-desorption isotherms were also investigated, as shown in Figure 3, together with the TEM images (Figure 3, inset). The BET surface area of the D-CN sample is

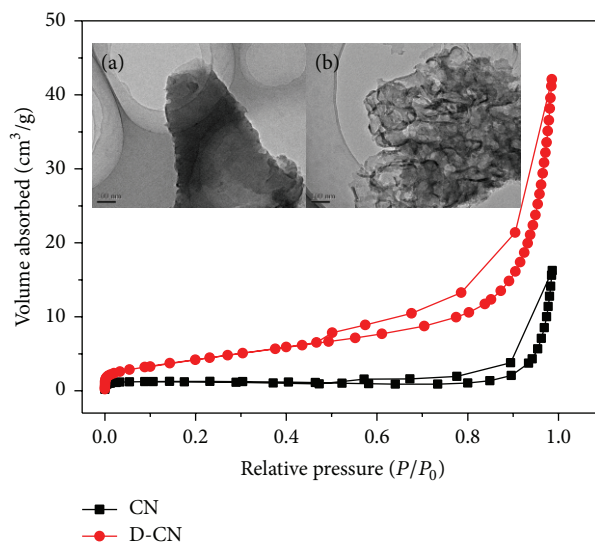


FIGURE 3: N_2 adsorption-desorption isotherms of CN and D-CN. Inset is the TEM images of (a) CN and (b) D-CN samples.

$16.1\text{ m}^2\text{ g}^{-1}$, which is almost three times higher than the bulk CN ($5.1\text{ m}^2\text{ g}^{-1}$). As shown in Figure 3 (inset), the CN displays two-dimensional layered and plate-like sheets, while a much more loose aggregated structure accompanied with some nanosized channels or pores on the surface can be observed for D-CN, indicating the important role of the disordered precursor. This fabricated D-CN with high surface area and unique surface structure could be favourable for improving photocatalytic activity for H_2 evolution, which deserved a further investigation.

The UV-vis spectra are shown in Figure 4(a). Compared with the bulk CN, a remarkable red shift of the optical absorption was observed for D-CN, which suggests a decreased band gap. The characteristic appearing near 500 nm is ascribed to $n\text{-}\pi^*$ transitions which involves lone pairs on the edge N atoms of the triazine/heptazine rings [38]. Furthermore, the transitions cannot appear for the perfectly symmetric C_3N_4 units, and they are observed here as the structures are distorted with the increased defects and holes, including effects from both layer buckling and deviation of the ring units from trigonal symmetry. Consequently, the extension of electron delocalization in the aromatic sheets with enhanced structural connections conduces the shift, somewhat similar to the bathochromic shift effect in J-aggregates. Within this context, more solar photon flux can be covered since the absorbance wavelength range extends to 800 nm. The enhanced absorbance intensities together with the enlarged surface areas are favourable for light harvesting and charge transfer that can improve the photocatalytic performance significantly.

Figure S4 shows the PL spectra of the as-prepared samples excited by 365 nm at room temperature. For these two samples, one main emission peak appears at about 465 nm, ascribed to the band-band recombination of the charge carriers with emission photon energy equal to its bandgap energy. Correspondingly, an obvious fluorescence quenching

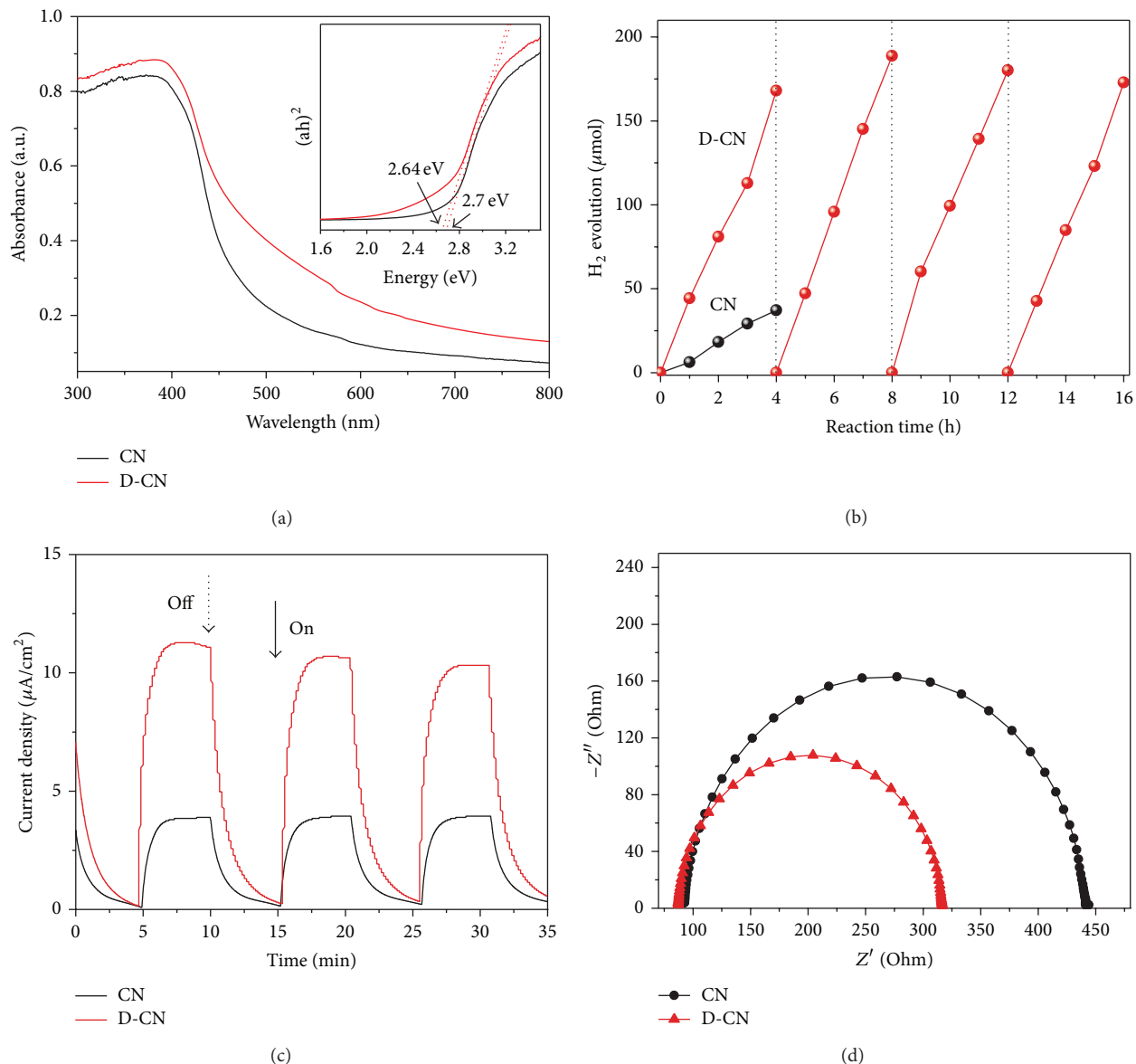


FIGURE 4: (a) UV-vis absorption spectra of the CN and D-CN samples. (b) Stability test of 3.0 wt% Pt-deposited D-CN (50 mg) for H_2 production in aqueous triethanolamine solution (10 vol%) under visible light and CN sample is also shown for comparison. (c) Transient photocurrent generation from CN and D-CN electrodes at 0.6 V versus Ag/AgCl in 0.2 M Na_2SO_4 under simulated sunlight irradiation. (d) EIS Nyquist plots of CN and D-CN.

is observed for the D-CN sample. That means the radiative charge recombination, which happens on the CN sample, has been efficiently suppressed. The suppression is due to the electron delocalization on surface terminal sites or the reduced density of charge carrier traps for electron-hole recombination. Furthermore, radiationless transitions have also been considered to cause fluorescence quenching, which is an unwanted process in photocatalysis either, increasing heat loss [39].

Visible-light-induced hydrogen production was evaluated to examine the catalytic activity of the samples, and a 16 h experiment with intermittent evacuation every 4 h was performed to investigate the stability of D-CN. Figure 4(b)

shows a remarkable improvement of D-CN sample in hydrogen evolution activities over bulk CN, whilst it increases steadily without noticeable deterioration of the activity. In addition, an extremely high apparent quantum yield (AQY, 2.7%) is obtained at 420 nm. The turnover numbers with respect to the melem units and Pt atoms are 2.05 and 74.2, respectively, clearly indicating that the reaction indeed proceeds catalytically.

The transient photocurrent responses of the CN and D-CN samples were investigated at a constant voltage of 0.6 V versus Ag/AgCl with several on-off cycles of intermittent simulated sunlight irradiation. As shown in Figure 4(c), both CN and D-CN photoanodes demonstrated steady and prompt

photocurrent generation during the on and off cycles of illumination, manifesting the photoelectrochemical activity and stability of both samples. The D-CN photoanode shows more than two times higher photocurrent intensity than the CN photoanode. To gain deeper insights into the charge transport behaviour in the samples, we also conducted electrochemical impedance spectroscopy (EIS) measurements in dark (Figure 4(d)). The D-CN exhibits the much smaller semicircular in Nyquist plots, suggesting a higher electron transfer conductivity of in D-CN film than in CN film [40]. The calculated electron transfer resistances with an equivalent circuit are 229.9 Ω and 372.3 Ω for the D-CN and CN photoanodes, respectively.

4. Conclusions

In summary, a facile method using disordered precursors was introduced to produce g-C₃N₄ with optimized structures for hydrogen evolution. The loose aggregates which are held together by weak, noncovalent interactions play important roles in living systems and the tiny distinction will influence the traditional chemical route. The final D-CN sample has improved intrinsic texture, morphology, optical properties and therefore leads to a significant enhancement in the photocatalytic activity for hydrogen evolution under visible light. This opens up new dimensions for the study of a general approach for preparing other catalysts with improved or new properties and extended applications.

Conflict of Interests

The authors declare that there is no conflict of interests regarding the publication of this paper.

Acknowledgments

The authors thank Professor Caihao Hong for the valuable discussion on XANES. This work was financially supported by National Natural Science Foundation of China (21373083), SRF for ROCS, SEM, SRFDP, Programme for Professor of Special Appointment (Eastern Scholar) at Shanghai Institutions of Higher Learning and Australian Research Council's Future Fellowships (FT120100913).

References

- [1] X. Chen, S. Shen, L. Guo, and S. S. Mao, "Semiconductor-based photocatalytic hydrogen generation," *Chemical Reviews*, vol. 110, no. 11, pp. 6503–6570, 2010.
- [2] A. Fujishima and K. Honda, "Electrochemical photolysis of water at a semiconductor electrode," *Nature*, vol. 238, no. 5358, pp. 37–38, 1972.
- [3] Z. Yi, J. Ye, N. Kikugawa et al., "An orthophosphate semiconductor with photooxidation properties under visible-light irradiation," *Nature Materials*, vol. 9, no. 7, pp. 559–564, 2010.
- [4] X. Wang, K. Maeda, A. Thomas et al., "A metal-free polymeric photocatalyst for hydrogen production from water under visible light," *Nature Materials*, vol. 8, no. 1, pp. 76–80, 2009.
- [5] A. Thomas, A. Fischer, F. Goettmann et al., "Graphitic carbon nitride materials: variation of structure and morphology and their use as metal-free catalysts," *Journal of Materials Chemistry*, vol. 18, no. 41, pp. 4893–4908, 2008.
- [6] I. D. W. Samuel and G. A. Turnbull, "Organic semiconductor lasers," *Chemical Reviews*, vol. 107, no. 4, pp. 1272–1295, 2007.
- [7] G. Liu, P. Niu, C. Sun et al., "Unique electronic structure induced high photoreactivity of sulfur-doped graphitic C₃N₄," *Journal of the American Chemical Society*, vol. 132, no. 33, pp. 11642–11648, 2010.
- [8] J. Li, B. Shen, Z. Hong, B. Lin, B. Gao, and Y. Chen, "A facile approach to synthesize novel oxygen-doped g-C₃N₄ with superior visible-light photoreactivity," *Chemical Communications*, vol. 48, no. 98, pp. 12017–12019, 2012.
- [9] B. Yue, Q. Li, H. Iwai, T. Kako, and J. Ye, "Hydrogen production using zinc-doped carbon nitride catalyst irradiated with visible light," *Science and Technology of Advanced Materials*, vol. 12, no. 3, Article ID 034401, 2011.
- [10] Z. Lin and X. Wang, "Nanostructure engineering and doping of conjugated carbon nitride semiconductors for hydrogen photosynthesis," *Angewandte Chemie—International Edition*, vol. 52, no. 6, pp. 1735–1738, 2013.
- [11] H. Yan, "Soft-templating synthesis of mesoporous graphitic carbon nitride with enhanced photocatalytic H₂ evolution under visible light," *Chemical Communications*, vol. 48, no. 28, pp. 3430–3432, 2012.
- [12] X. Wang, K. Maeda, X. Chen et al., "Polymer semiconductors for artificial photosynthesis: hydrogen evolution by mesoporous graphitic carbon nitride with visible light," *Journal of the American Chemical Society*, vol. 131, no. 5, pp. 1680–1681, 2009.
- [13] X.-H. Li, J. Zhang, X. Chen et al., "Condensed graphitic carbon nitride nanorods by nanoconfinement: promotion of crystallinity on photocatalytic conversion," *Chemistry of Materials*, vol. 23, no. 19, pp. 4344–4348, 2011.
- [14] Y. Hou, A. B. Laursen, J. Zhang et al., "Layered nanojunctions for hydrogen-evolution catalysis," *Angewandte Chemie: International Edition*, vol. 52, no. 13, pp. 3621–3625, 2013.
- [15] Y. Di, X. Wang, A. Thomas, and M. Antonietti, "Making metal-carbon nitride heterojunctions for improved photocatalytic hydrogen evolution with visible light," *ChemCatChem*, vol. 2, no. 7, pp. 834–838, 2010.
- [16] J. Zhang, G. Zhang, X. Chen et al., "Co-monomer control of carbon nitride semiconductors to optimize hydrogen evolution with visible light," *Angewandte Chemie*, vol. 51, no. 13, pp. 3183–3187, 2012.
- [17] J. Zhang, X. Chen, K. Takane et al., "Synthesis of a carbon nitride structure for visible-light catalysis by copolymerization," *Angewandte Chemie*, vol. 49, no. 2, pp. 441–444, 2010.
- [18] A. Suryawanshi, P. Dhanasekaran, D. Mhamane et al., "Doubling of photocatalytic H₂ evolution from g-C₃N₄ via its nanocomposite formation with multiwall carbon nanotubes: electronic and morphological effects," *International Journal of Hydrogen Energy*, vol. 37, no. 12, pp. 9584–9589, 2012.
- [19] Q. Li, B. Yue, H. Iwai, T. Kako, and J. Ye, "Carbon nitride polymers sensitized with N-doped tantalum acid for visible light-induced photocatalytic hydrogen evolution," *The Journal of Physical Chemistry C*, vol. 114, no. 9, pp. 4100–4105, 2010.
- [20] X. L. Wang, W. Q. Fang, H. F. Wang et al., "Surface hydrogen bonding can enhance photocatalytic H₂ evolution efficiency," *Journal of Materials Chemistry A*, vol. 1, no. 45, pp. 14089–14096, 2013.

- [21] X. L. Wang, W. Q. Fang, S. Yang, P. Liu, H. Zhao, and H. G. Yang, "Structure disorder of graphitic carbon nitride induced by liquid-assisted grinding for enhanced photocatalytic conversion," *RSC Advances*, vol. 4, no. 21, pp. 10676–10679, 2014.
- [22] Y. Cui, J. Zhang, G. Zhang et al., "Synthesis of bulk and nanoporous carbon nitride polymers from ammonium thiocyanate for photocatalytic hydrogen evolution," *Journal of Materials Chemistry*, vol. 21, no. 34, pp. 13032–13039, 2011.
- [23] F. Dong, L. Wu, Y. Sun, M. Fu, Z. Wu, and S. C. Lee, "Efficient synthesis of polymeric g-C₃N₄ layered materials as novel efficient visible light driven photocatalysts," *Journal of Materials Chemistry*, vol. 21, no. 39, pp. 15171–15174, 2011.
- [24] F. Dong, Y. Sun, L. Wu, M. Fu, and Z. Wu, "Facile transformation of low cost thiourea into nitrogen-rich graphitic carbon nitride nanocatalyst with high visible light photocatalytic performance," *Catalysis Science and Technology*, vol. 2, no. 7, pp. 1332–1335, 2012.
- [25] G. R. Desiraju, "Linus Pauling: the all-chemist," *Nature*, vol. 408, no. 6811, p. 407, 2000.
- [26] G. R. Desiraju, "Chemistry beyond the molecule," *Nature*, vol. 412, no. 6845, pp. 397–400, 2001.
- [27] T. Steiner, "The hydrogen bond in the solid state," *Angewandte Chemie—International Edition*, vol. 41, pp. 48–76, 2002.
- [28] E. Boldyreva, "Mechanochemistry of inorganic and organic systems: what is similar, what is different?" *Chemical Society Reviews*, vol. 42, no. 18, pp. 7719–7738, 2013.
- [29] E. W. Hughes, "The crystal structure of dicyandiamide," *Journal of the American Chemical Society*, vol. 62, no. 5, pp. 1258–1267, 1940.
- [30] W. J. Jones and W. J. Orville-Thomas, "The infra-red spectrum and structure of dicyandiamide," *The Faraday Society and Contributors*, vol. 55, pp. 193–202, 1959.
- [31] F. Dong, M. Ou, Y. Jiang, S. Guo, and Z. Wu, "Efficient and durable visible light photocatalytic performance of porous carbon nitride nanosheets for air purification," *Industrial and Engineering Chemistry Research*, vol. 53, no. 6, pp. 2318–2330, 2014.
- [32] K. Parvez, S. Yang, Y. Hernandez et al., "Nitrogen-doped graphene and its iron-based composite as efficient electrocatalysts for oxygen reduction reaction," *ACS Nano*, vol. 6, no. 11, pp. 9541–9550, 2012.
- [33] Y. Hou, Z. Wen, S. Cui, X. Guo, and J. Chen, "Constructing 2D porous graphitic C₃N₄ nanosheets/nitrogen-doped graphene/layered MoS₂ ternary nanojunction with enhanced photoelectrochemical activity," *Advanced Materials*, vol. 25, no. 43, pp. 6291–6297, 2013.
- [34] J.-B. Zhang, Z.-C. Tan, S.-H. Meng, S.-H. Li, and L.-M. Zhang, "Heat capacity and thermal decomposition of dicyandiamide," *Thermochimica Acta*, vol. 307, no. 1, pp. 11–15, 1997.
- [35] L. Liu, T.-K. Sham, and W. Han, "Investigation on the electronic structure of BN nanosheets synthesized via carbon-substitution reaction: The arrangement of B, N, C and O atoms," *Physical Chemistry Chemical Physics*, vol. 15, no. 18, pp. 6929–6934, 2013.
- [36] Y. Gao, G. Hu, J. Zhong et al., "Nitrogen-doped sp²-hybridized carbon as a superior catalyst for selective oxidation," *Angewandte Chemie*, vol. 52, no. 7, pp. 2109–2113, 2013.
- [37] S. C. Ray, C. W. Pao, J. W. Chiou et al., "Electronic properties of a-CN_x thin films: an x-ray-absorption and photoemission spectroscopy study," *Journal of Applied Physics*, vol. 98, no. 3, Article ID 033708, 2005.
- [38] A. B. Jorge, D. J. Martin, M. T. S. Dhanoa et al., "H₂ and O₂ evolution from water half-splitting reactions by graphitic carbon nitride materials," *Journal of Physical Chemistry C*, vol. 117, no. 14, pp. 7178–7185, 2013.
- [39] J. Zhang, M. Zhang, R.-Q. Sun, and X. Wang, "A facile band alignment of polymeric carbon nitride semiconductors to construct isotype heterojunctions," *Angewandte Chemie—International Edition*, vol. 51, no. 40, pp. 10145–10149, 2012.
- [40] Y. Hou, F. Zuo, A. Dagg, and P. Feng, "A three-dimensional branched cobalt-doped α-Fe₂O₃ nanorod/MgFe₂O₄ heterojunction array as a flexible photoanode for efficient photoelectrochemical water oxidation," *Angewandte Chemie—International Edition*, vol. 52, no. 4, pp. 1248–1252, 2013.

Research Article

Visible-Light Degradation of Dyes and Phenols over Mesoporous Titania Prepared by Using Anthocyanin from Red Radish as Template

Zhiying Yan, Wenjuan Gong, Yongjuan Chen, Deliang Duan, Junjie Li, Wei Wang, and Jiaqiang Wang

Department of Applied Chemistry, Key Laboratory of Medicinal Chemistry for Natural Resource, Ministry of Education, Yunnan University, Kunming 650091, China

Correspondence should be addressed to Jiaqiang Wang; jqwang@ynu.edu.cn

Received 7 July 2014; Accepted 20 August 2014; Published 2 September 2014

Academic Editor: Wenjun Luo

Copyright © 2014 Zhiying Yan et al. This is an open access article distributed under the Creative Commons Attribution License, which permits unrestricted use, distribution, and reproduction in any medium, provided the original work is properly cited.

Heterogeneous photocatalysis is able to operate effectively to eliminate organic compounds from wastewater in the presence of semiconductor photocatalyst and a light source. Although photosensitization of titania by organic dyes is one of the conventional ways for visible-light utilization of titania, previous studies have not yet addressed the use of natural food coloring agents as templates in the synthesis of mesostructured materials, let alone the simultaneous achievement of highly crystalline mesoscopic framework and visible-light photocatalytic activity. In this work, anthocyanin, a natural pigment from red radish was directly used as template in synthesis of highly crystalline mesoporous titania. The synthesized mesoporous titania samples were characterized by a combination of various physicochemical techniques, such as XRD, SEM, HRTEM, nitrogen adsorption/desorption, and diffuse reflectance UV-Vis. The prepared mesoporous titania photocatalyst exhibited significant activity under visible-light irradiation for the degradation of dyes and phenols due to its red shift of band-gap-absorption onset and visible-light response as a result of the incorporation of surface carbon species.

1. Introduction

Organic dyes and phenolic compounds usually come from industrial effluent and other artificial activities and are very toxic compounds which contribute significantly to water pollution. Elimination of these organic compounds from wastewater using heterogeneous photocatalysis which are able to operate effectively in the presence of semiconductor photocatalytic materials and a light source appears as the most emerging destructive technology [1]. Most of the semiconductor materials reported in the literature as photocatalysts are based on TiO_2 because of its low price and steady and high photocatalytic activation. Unfortunately, the wide band gap of pristine TiO_2 limits its light absorption only to the UV-light range and 97% of the visible spectra of sunlight reaching the surface of earth are unable to be used by TiO_2 , which hold back its practical applications. Therefore, many researchers are focusing on how to modify the quality of

TiO_2 to improve the efficiency of TiO_2 to absorb visible light [2, 3]. Photosensitization of TiO_2 nanoparticles by organic dyes was found to be an effective approach to enhance the visible-light utilization of TiO_2 , because organic dye molecules attached to the surface of TiO_2 are responsible for absorbing the incoming light [4–6]. For example, Chowdhury et al. [6] have used eosin Y dye as a sensitizer to prepare visible-light-active TiO_2 catalyst and found that about 93% degradation of 40 ppm phenol solution was achieved within 90 min using eosin Y- TiO_2 /Pt photocatalyst under visible solar light. Recently, natural dyes extracted from flowers, leaves, fruits, and beverages have become a viable alternative to expensive or toxic organic sensitizers because of their low cost, easy attainability, abundance in supply of raw materials, and no environment threat [7–9]. Among them, anthocyanins are naturally occurring compounds that are responsible for the coloration of flowers, fruits, fruit juice, wines, leaves, stems, bulbs, roots, and so forth. They are also

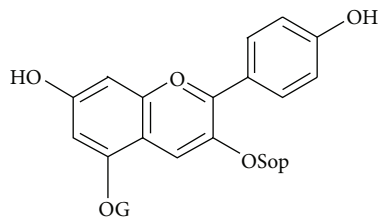


FIGURE 1: The structural formula of radish red pigment.

the most important group of visible plant pigments besides chlorophyll and show a broad absorption band in the range of visible light. Therefore, anthocyanins often are used as natural dye sensitizers of wide band gap semiconductors. Calogero et al. [10] extracted anthocyanin natural dyes from *Clitoria ternatea* as sensitizer of dye sensitized solar cells and absorption spectra of *Clitoria ternatea* sensitized nanocrystalline TiO_2 thin films show a small shift towards longer wavelength side. Zyoud et al. [11] have successfully used as them a safe alternative sensitizer in photodegradation of organic water contaminant catalyzed by TiO_2 particles. However, these dye-sensitized TiO_2 catalysts suffer from poor stability due to the thermal or photochemical decomposition of dyes and weak binding energy between the TiO_2 and dyes.

What is interesting is that Faul and Antonietti [12] have developed a facile method to synthesize an optically functional, organic composite material by simple precipitation of charged dyes with oppositely charged surfactants. Recently, Xu et al. [13] have also prepared mesoporous silica by using basic fuchsin as template and methylene diisocyanate or aminopropyltriethoxysilane as bridging molecules. More recently, in our group chrome azurol S [14] and even commercial synthetic dyes [15] have been successfully used as templates in synthesis of mesoporous anatase TiO_2 , shifting the absorption edge of TiO_2 to the visible-light range, narrowing the band gap, and resulting in strong absorption in the visible region. The prepared TiO_2 exhibited significant photocatalytic activity in the degradation of four dyes, gentian violet, methyl violet, rhodamine B, and methylthionine chloride under solar light irradiation.

Herein, in the continuation of our work, we further investigated the synthesis and its photocatalytic activity of mesoporous titania templated by anthocyanin from red radish (*Raphanus sativus* L.), an edible red shell, and heart radish which have a long planting history locally. Here, we call it the radish red pigment. The main ingredient of radish red pigment is pelargonidin derivative which belongs to one of the most widespread anthocyanin. The structural formula for pelargonidin is pelargonidin-3-sophoroside, 5-glucoside structure [16, 17] as shown in Figure 1. The prepared mesoporous TiO_2 was evaluated by the degradation of three dyes such as methylthionine chloride, gentian violet, and rhodamine B and two phenolic compounds including phenol and 2, 4-dichlorophenol under visible light. Besides, other food dyes with different structural forms, such as purple sweet potato color, safflower yellow, and gardenia blue pigment, were also used as templates to prepare TiO_2

aimed at investigating contrastively the influence of template structure on photocatalytic activities of TiO_2 . Our works imply that anthocyanin from red radish could be potential template for direct synthesis of highly crystalline mesoporous titania with visible-light photocatalytic activity to degrade organic contaminants. To the best of our knowledge, there is no report on using natural pigments as a template for synthesis of mesoporous materials, let alone the simultaneous achievement of highly crystalline mesoscopic frameworks and visible-light photocatalytic activity. In particular, the prepared mesoporous TiO_2 show good activity in the phenol degradation under visible-light irradiation, which have not yet studied in our previous reports [14, 15].

2. Materials and Methods

2.1. Materials

2.1.1. Chemicals. All chemicals such as titanium isopropoxide $\text{Ti}[\text{OCH}(\text{CH}_3)_2]_4$, three dyes including methylthionine chloride (MC), rhodamine B (RB), and gentian violet (GV) and two phenolic compounds including phenol and 2, 4-dichlorophenol were used without further purification and all of them were analytical reagents.

2.1.2. Natural Food Coloring Agents. All pigments were kindly provided by Yunnan Tonghai Yang Natural Products Co., LTD. (a) Radish red pigment (RRP) was extracted from *Raphanus sativus* L., an edible red shell and heart radish which have a long planting history locally. The process was checked, washed, sliced, extracted, filtrated, purified, concentrated, sterilized, sprayed, and dried. The main ingredient is anthocyanidin which contains pelargonidin. (b) Purple sweet potato color (PSPC) was extracted from purple root tuber of edible sweet potato (*Ipomoea batatas*) planted locally. The process was checked, washed, sliced, extracted, filtrated, purified, concentrated, sterilized, sprayed, and dried. The main coloring ingredient is cyaniding acyl glucoside and peonidin acyl glucoside. (c) Safflower yellow (SY) was extracted from the petal of *Carthamus tinctorius*, by the process of extracting, filtrating, purifying, concentrating, sterilizing, spraying, and drying. The main ingredient is carthamin yellow. (d) Gardenia blue (GB) was obtained by amination of genipin which was formed by hydrolysis of colorless geniposide from the gardenia fruit of madder family by biological fermentation.

2.2. Preparation of Mesoporous TiO_2 . In a typical preparation process of 1.0 g radish red pigment was dissolved in 30 mL ethanol under stirring, and 3.0 g titanium isopropoxide $\text{Ti}[\text{OCH}(\text{CH}_3)_2]_4$ was added slowly until the solution became a clear gel. Then 60 mL water was added dropwise under continuous stirring, which caused the immediate precipitation of a solid. Subsequently, the final mixture was stirred for 24 h and then transferred into a Teflon bottle and treated under autogenous pressure at 363 K for 7 days, filtered, washed, dried, and calcined at 673 K in air for 6 h. Finally light-yellow powder was obtained. The samples are designated

as MTiO_2/RRP . Following the same procedure as preparing MTiO_2/RRP , other mesoporous TiO_2 catalyst prepared by using purple sweet potato color, safflower yellow, and gardenia blue pigment as templates are called $\text{MTiO}_2/\text{PSPC}$, MTiO_2/SY , and MTiO_2/GB , respectively.

2.3. Characterization. X-ray powder diffraction (XRD) experiments were conducted on a D/max-3B spectrometer with $\text{Cu K}\alpha$ radiation. Scans were made in the 2θ range $0.5\text{--}5^\circ$ with a scan rate of $0.02^\circ/\text{min}$ (low angle diffraction) and in the 2θ range $10\text{--}90^\circ$ with a scan rate of $10^\circ/\text{min}$ (wide angle diffraction). High-resolution transmission electron microscopy (HRTEM) images were taken on a TEM (JEOL-200CX). Pore size distributions, BET surface areas, and pore volumes were measured by nitrogen adsorption/desorption using a NOVA 2000e gas sorption analyzer (Quantachrome Corp.). Prior to the analysis, the samples were degassed at 150°C for 1 h. UV-Vis diffuse reflectance spectra were measured at room temperature in air on a Shimadzu UV-2401PC photometer over the range from 200 to 800 nm. FT-IR measurements were performed on a Thermo Nicolet 8700 instrument. Potassium bromide pellets containing 0.5% of the catalysts were used in FT-IR experiments and 32 scans were accumulated for each spectrum in transmission, at a spectral resolution of 4 cm^{-1} . The spectrum of dry KBr was taken for background subtraction. X-ray photoelectron spectra (XPS) measurement was performed on a PHI5000VersaProbe II analyzer.

2.4. Evaluation of Photocatalytic Activity. The reactions of the photocatalytic degradation of dyes and phenolic compounds were carried out in a glass batch photoreactor containing 50 mL of a 10 ppm model solution and 25 mg of photocatalyst. The suspensions were magnetically stirred in dark for 24 h to attain adsorption-desorption equilibrium between dyes and mesoporous TiO_2 . The decrease due to adsorption can be deduced after the adsorption equilibrium was achieved. After 24 h in the dark, the reactor was illuminated with a 500 W tungsten lamp. A combination of two filters, VIS-NIR long pass filter (400 nm) and a coloured glass filter ($>420\text{ nm}$), was utilized for the purpose of allowing only visible-light radiation. Samples were analyzed after centrifugation (1500 rpm for 10 min). The color removal of the dye solution was measured by Shimadzu UV-2401PC photometer over the range from 400 to 800 nm.

3. Results and Discussion

3.1. Structure and Morphology of Mesoporous Titania. The XRD patterns of MTiO_2/RRP prepared by using radish red pigment as a template, shown in Figure 2, demonstrates clearly that the sample is highly crystallized and could be indexed to titania of the anatase phase (JCPDS card number 04-0477). No other diffraction is observed, suggesting a pure anatase phase. Detailed analysis of the peak broadening of the (1 0 1) reflection using the Scherrer equation indicates an average crystallite size of ca. 8 nm, indicating that the anatase TiO_2 particles are composed of nanocrystal subunits.

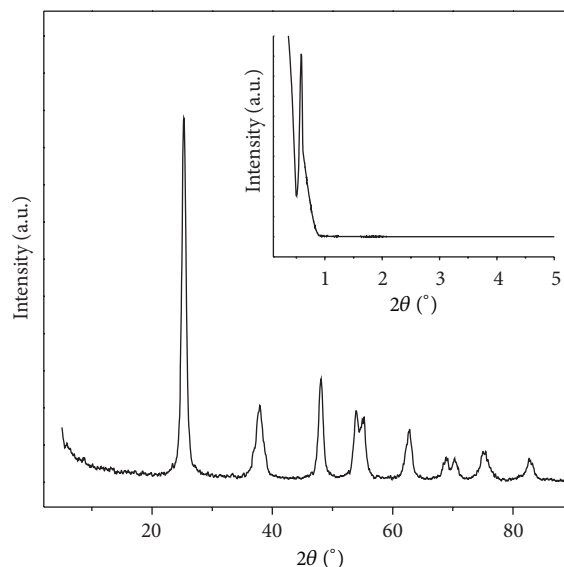


FIGURE 2: XRD wide and small angle patterns of MTiO_2/RRP .

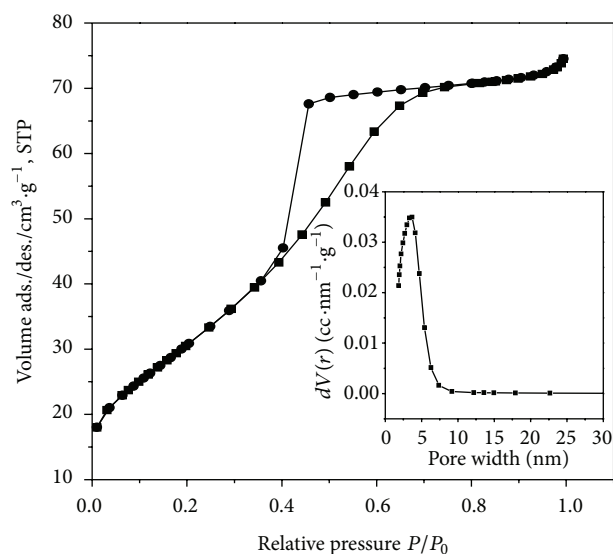


FIGURE 3: Nitrogen adsorption-desorption isotherm of MTiO_2/RRP . BJH pore size distributions are shown in the inset.

Moreover, the small-angle peak at around 0.8° in 2θ (inset in Figure 2) corresponds to the internanoparticle separations of 12.6 nm, suggesting that the materials lack long-range ordered arrangements. This is coincident with the results in the literatures [18, 19].

The N_2 adsorption/desorption isotherms and the pore size distribution of the obtained MTiO_2/RRP are shown in Figure 3. This hysteresis shows an IV-type hysteresis loop in the P/P_0 range from 0.40 to 0.8, a characteristic of titania type mesoporous materials. The BET surface area and pore diameter of the sample are $112\text{ m}^2\cdot\text{g}^{-1}$ and 3.3 nm, respectively. This phenomenon is in good agreement with those mesoporous TiO_2 templated by other templates, such as block copolymers or surfactants. Typical mesoporous

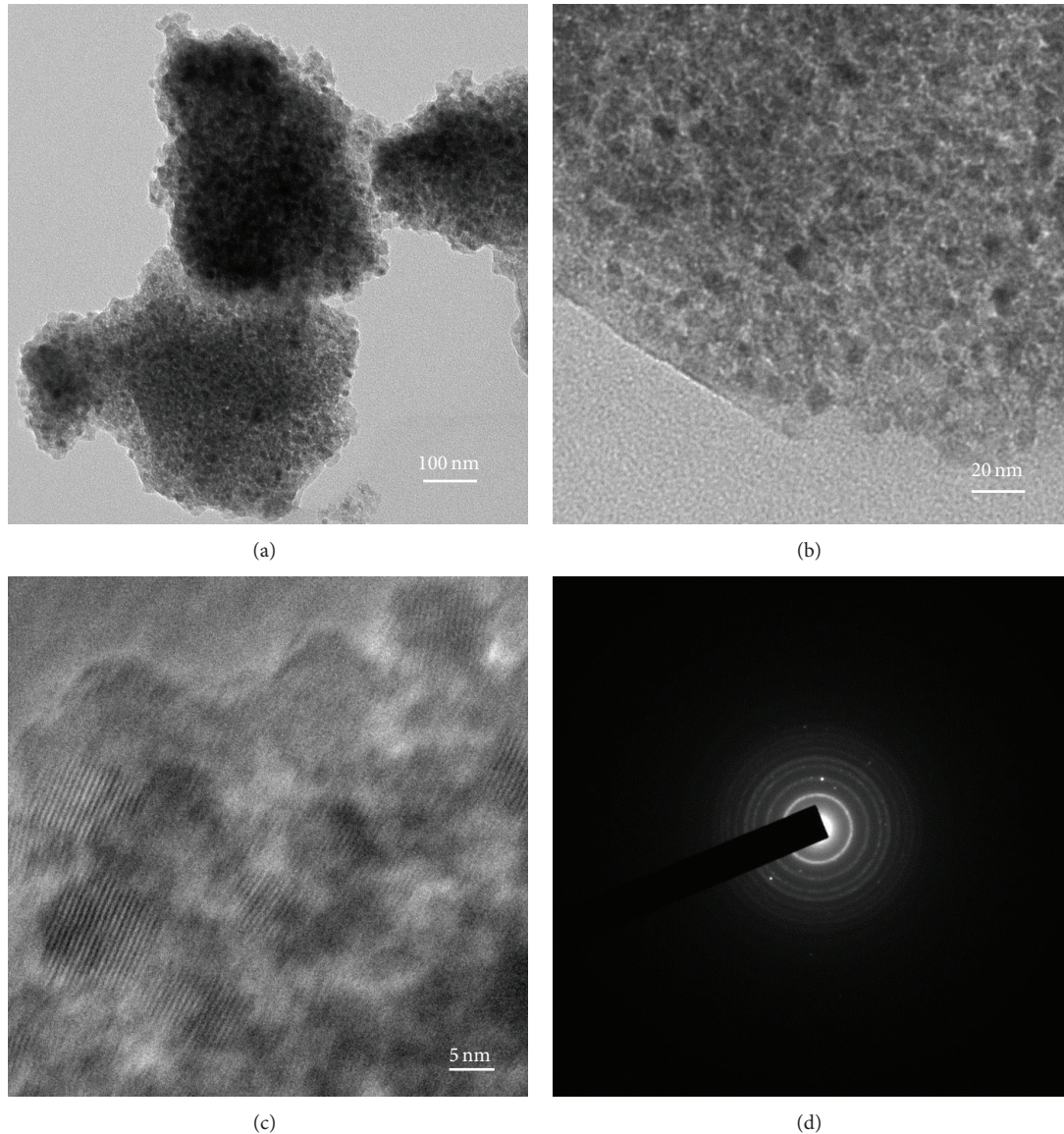


FIGURE 4: TEM ((a) and (b)), HRTEM (c) images, and ED (d) of MTiO_2/RRP .

titania prepared by using dodecylamine as templates shows highly aggregated and nonuniform structure [20]. TEM image presented in Figure 4(a) shows the morphology of MTiO_2/RRP . By contrast, MTiO_2/RRP particles are reasonably uniform in size of 200 nm. Moreover, direct evidence for the existence of mesopores with highly crystalline and orderly wormhole frameworks has been obtained from TEM images and selected area electron diffraction pattern shown in Figures 4(b), 4(c), and 4(d), respectively. Therefore, N_2 adsorption/desorption isotherms, XRD, and TEM are all similar to those of mesoporous TiO_2 templated by block copolymers or surfactants [21] or commercial synthetic dyes previously used by us [15].

3.2. Photocatalytic Activity of Mesoporous TiO_2 . The photoactivities of the synthesized samples were evaluated by the degradation of dyes and phenolic compounds including

MC, RB, GV, phenol, and 2, 4-dichlorophenol under visible light. In order to obtain the real photodegradation yield due to the photocatalysis in the presence of photocatalysts, the decreases of the contaminants concentration because of the adsorption and direct photolysis should be deducted. The photodegradation yield was calculated by the following equation [22]:

$$\text{Photodegradation yield} = \frac{(C_o - C_a - C_b)}{C_o} \times 100. \quad (1)$$

C_o is the initial concentration of contaminants, C_a is the concentration after photodegradation of contaminants, and C_b is the decreased concentration because of the direct photolysis.

Based on the above definition, the comparison of their photodegradation yields for the degradation of three dyes under visible-light irradiation is shown in Figure 5. It is noted

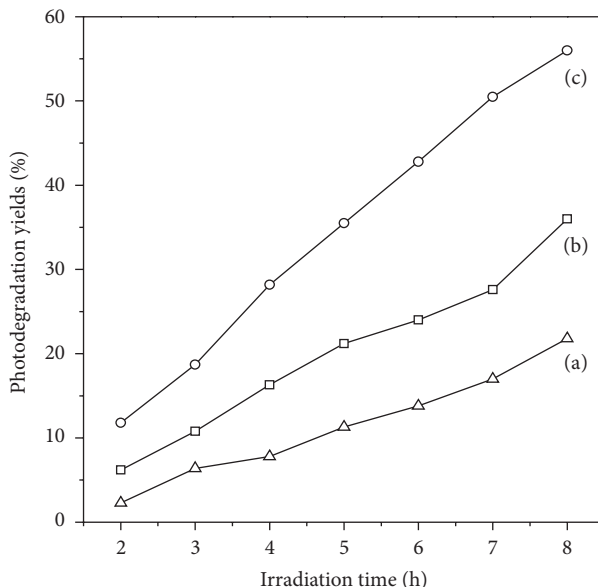


FIGURE 5: Photodegradation yields of methylthionine chloride (a), rhodamine B (b), and gentian violet (c) over MTiO_2/RRP under visible-light irradiation ($\lambda > 420 \text{ nm}$).

that the photodegradation yields increased sharply with the exposure time, and 20%, 34.9%, and 56.2% of MC, RB, and GV were degraded within 8 h, respectively. The results suggest that some dyes, especially RB, could be degraded effectively by MTiO_2/RRP . Such behavior has not been observed when the commercial Degussa P25 TiO_2 was used. As is known to all, P25 TiO_2 does not exhibit any meaningful activity for the degradation of RB with visible light even though it exhibits photodegradation yield of $\sim 87\%$ with UV light. More interestingly, it was found in Figure 6 that the photocatalytic activity of MTiO_2/RRP for phenolic compounds was higher than that for dyes and the photodegradation yields of phenol and 2, 4-dichlorophenol are up to 54%, 65% after 4 h visible-light irradiation, respectively. By contrast, Degussa P25 TiO_2 had no any photocatalysis for degradation of the two phenolic compounds.

The success in synthesis of MTiO_2/RRP by using RRP as a template and its unusual visible-light activity of MTiO_2/RRP encouraged us to extend this method to other natural pigments. Following the same procedure as preparing MTiO_2/RRP , safflower yellow (SY), purple sweet potato color (PSPC), and gardenia blue pigment (GB) were used as templates to prepare mesoporous titania called $\text{MTiO}_2/\text{PSPC}$, MTiO_2/SY , and MTiO_2/GB , respectively. In the selected pigments, PSPC is an acylated anthocyanidin and SY belongs to chalcone group with the same type C6–C3–C6 backbone structure as anthocyanidin, whereas GB is a rare natural blue pigment with iridoid base structure. The structure of pigments [23–25] and the results of $\text{MTiO}_2/\text{PSPC}$, MTiO_2/SY , and MTiO_2/GB to degrade RB and phenol under visible-light irradiation are summarized in Table 1. It can be found that the photodegradation yields of RB over $\text{MTiO}_2/\text{PSPC}$ and MTiO_2/SY are 26.7% and 31.2% within 8 h, respectively, whereas MTiO_2/GB is only 4.6% of photodegradation to

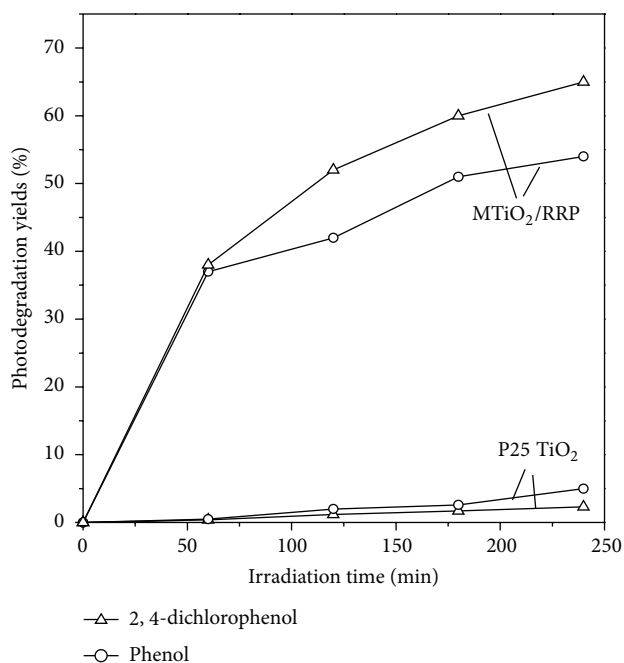
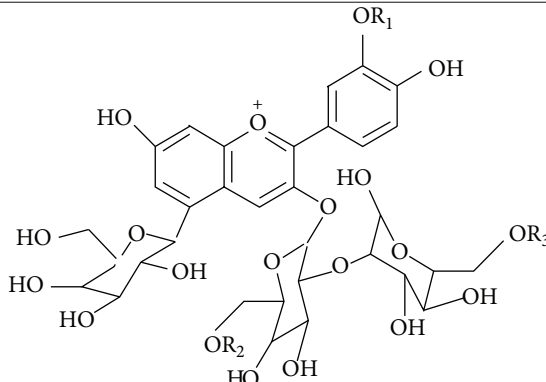
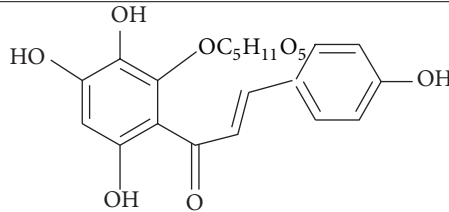
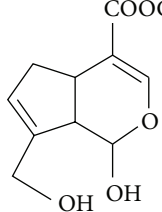


FIGURE 6: Photodegradation yields for degradation of phenol and 2, 4-dichlorophenol over MTiO_2/RRP and P25 TiO_2 under visible-light irradiation ($\lambda > 420 \text{ nm}$).

RB and is slightly better than commercial Degussa P25 TiO_2 on visible light activity. By contrast, only $\text{MTiO}_2/\text{PSPC}$ shows 29.8% of photodegradation yields after 4 h visible-light irradiation.

From Table 1, Figures 5 and 6, we find that TiO_2 prepared by RRP, PSPC, and SY with the C6–C3–C6 backbone structure shows the visible-light activity for RB. Furthermore,

TABLE 1: Summary of photodegradation yields for degradation of RB and phenol under visible-light irradiation over MTiO₂ samples synthesized by using different natural pigments as template.

Template	Molecular structures	Photodegradation yield (%)	
		RB	Phenol
PSPC		26.7	29.8
SY		31.2	—
GB		4.6	—
P25		0	4.3

TiO₂ prepared by RRP and PSPC of anthocyanin have more obvious catalyzed effect on phenol. These results suggest that the effectiveness of the titania photocatalysts prepared by using these natural pigments as templates maybe depend on the structure and complexity of natural pigments [26]. Although there are no more facts to illustrate the relationship between the structures of natural pigments and the photocatalytic efficiency of titania using natural pigments-templates in this study, it can be concluded that anthocyanin from radish red, that is radish red pigment, may be an appropriate selection of natural pigment templates which allows new visible-light photocatalysts to be built directly.

3.3. FT-IR and XPS Investigation. To gain further insight of these phenomena, UV-Vis, FTIR, and XPS spectra of MTiO₂/RRP, MTiO₂/GB along with P25 TiO₂ were investigated. The FT-IR spectra of MTiO₂/RRP, MTiO₂/GB, and P25 TiO₂ between 400 and 4000 cm⁻¹ are presented in Figure 7. Interestingly, the peak of MTiO₂/RRP in the range of 400–1000 cm⁻¹ which is a contribution from the vibrations

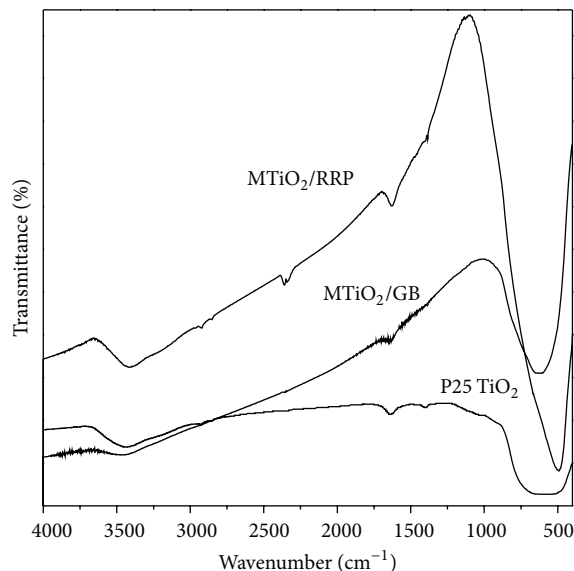


FIGURE 7: FT-IR spectra of MTiO₂/RRP, MTiO₂/GB, and P25.

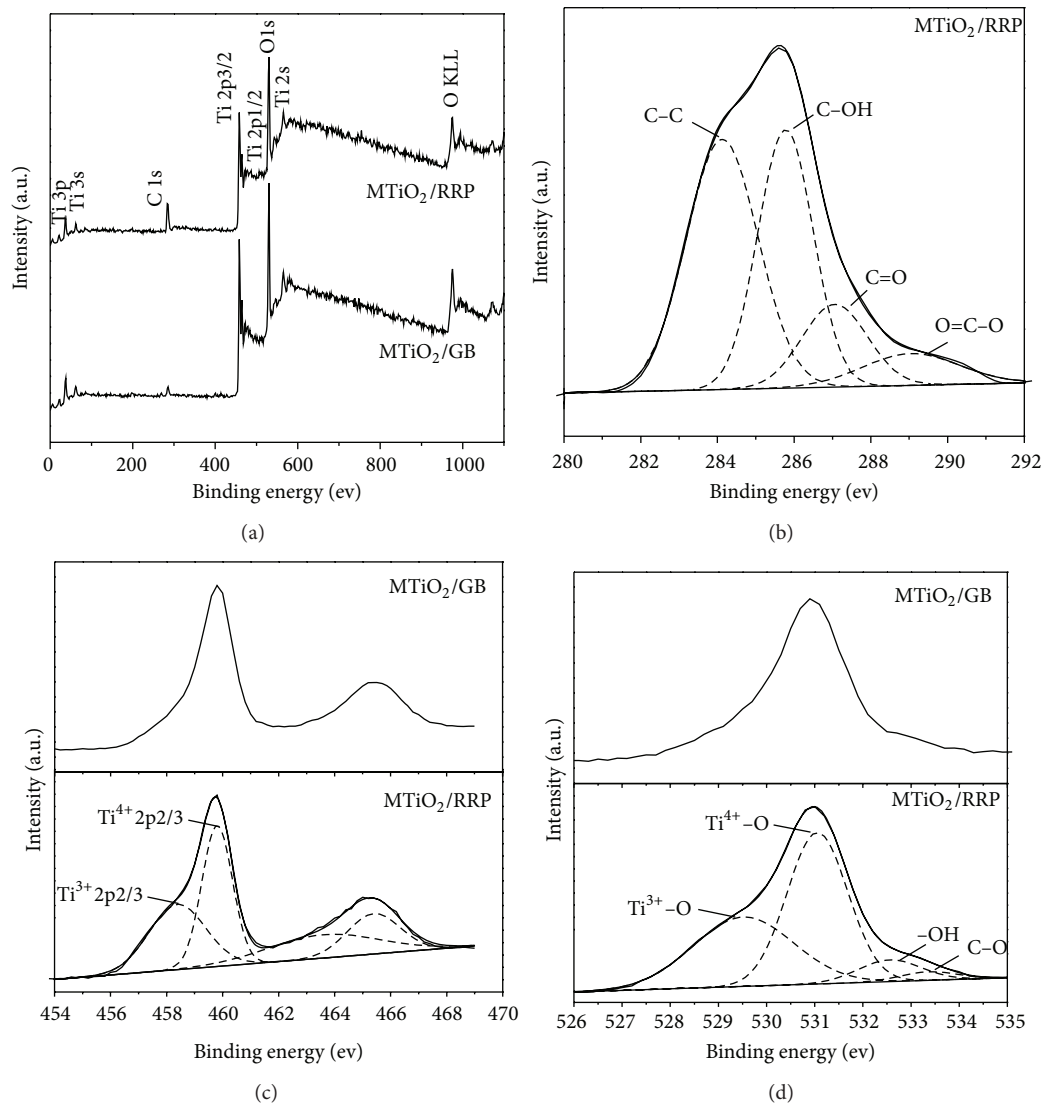


FIGURE 8: XPS survey spectrum of MTiO₂ (a) and corresponding C 1s (b), Ti 2p (c), and O 1s (d) high-resolution XPS spectra.

of Ti-O [21, 27] is much sharper than that of P25 TiO₂ and MTiO₂/GB. The two broad peaks at 1640 and 3200~3420 cm⁻¹ which can be attributed to the surface-adsorbed water and hydroxyl groups [21, 27, 28] were also observed in MTiO₂/RRP. The surface hydroxyl groups have been recognized to play an important role in the photodegradation process through their interactions with photogenerated holes. In addition, MTiO₂/RRP have two bands at 2925 and 2854 cm⁻¹ assigned to the asymmetric and symmetric stretching vibrations of -CH₂- and CH₃- in alkyl chains, as well as a band in the 1300-1500 cm⁻¹ assigned to CH₂ bending vibrations, which are evident [29-31]. The peak at 1400 cm⁻¹ is assigned to CO₂ band [31]. Thus these indicate that during the heating process, dye template was decomposed and removed or physically adsorbed on the surface of MTiO₂/RRP [31]. However, the FTIR data of -COOTi vibration referenced values of 1070, 1710 and 1220 cm⁻¹ [32, 33] were not found.

XPS measurements were also performed to elucidate the surface chemical composition and the oxidation state for the mesoporous TiO₂. Figure 8(a) depicts the full survey spectra of MTiO₂/RRP and MTiO₂/GB samples. One can see that in both samples the elements of Ti and O can be clearly identified, with the binding energies of Ti 2p and O 1s electrons at approximately 459.1 eV and 529.8 eV, respectively. Moreover, it is interestingly found that the carbon signal with the binding energies of C 1s electrons at approximately 285 eV is obviously stronger in MTiO₂/RRP than in MTiO₂/GB. This indicates that the surface of MTiO₂/RRP adsorbs more carbon likely from the organic precursors and template used to prepare the TiO₂, not adventitious hydrocarbon from the XPS instrument itself. To analyze the state of the carbon element in MTiO₂/RRP, the C 1s high-resolution XPS survey was conducted and the typical spectra are shown in Figure 8(b). The C 1s XPS curves of MTiO₂/RRP can be fitted to four peaks located at 284, 285.8, 287, and 289.2 eV by

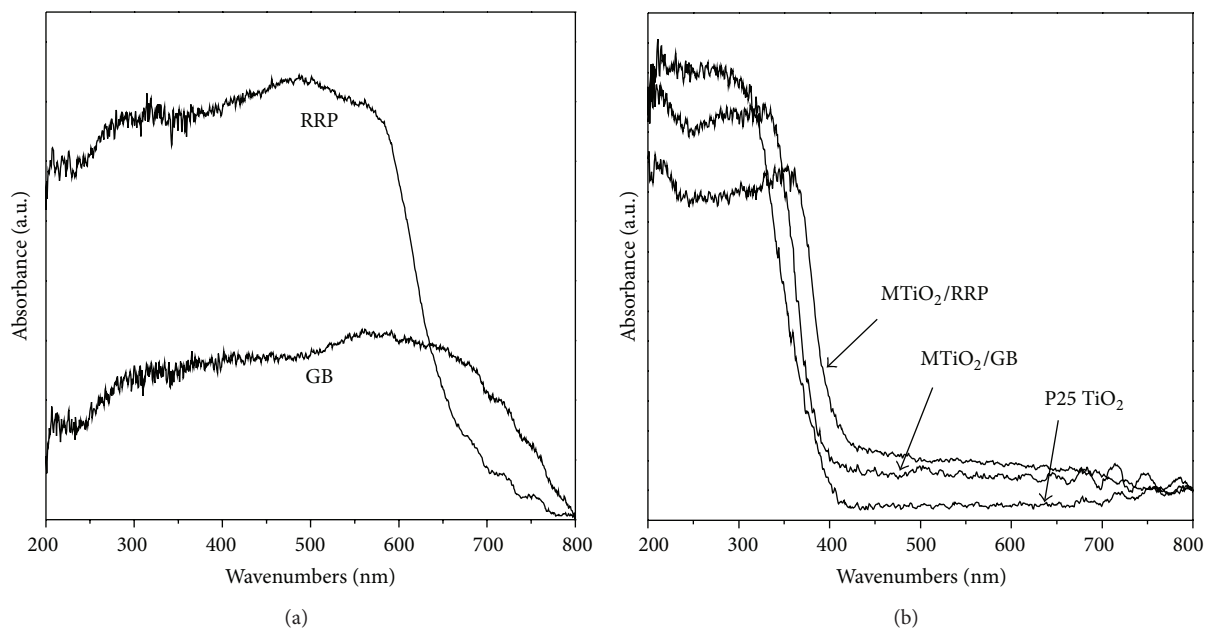


FIGURE 9: Comparison of absorption spectra of natural pigments RRP and GB (a); MTiO_2/RRP , MTiO_2/GB , and P25 (b).

using computer assisted Gaussian-Lorentzian peak model, respectively. The major peak at 284 eV is related to carbon atoms in the C–C, C=C, and C–H bonds [34]. In addition, the binding energies around 285.8, 287, and 289.2 eV are assigned to the C–O, C=O and O=C–O bonds, respectively [35]. The peak around 281 eV resulting from Ti–C bond was not observed, so carbon elements do not substitute oxygen atom in the lattice of anatase. These results are similar to those obtained by using commercial synthetic dyes in our previous work [15]. Figure 8(c) shows the high-resolution XPS spectra of Ti2p in MTiO_2/RRP and MTiO_2/GB samples, respectively. The Ti2p XPS curve of MTiO_2/RRP has a similar shape to MTiO_2/GB and could be resolved into two contributions corresponding to the different oxidation states of titanium. Each contribution consists of a doublet between the 2p_{3/2} and 2p_{1/2} peaks. A main doublet composed of two symmetric peaks situated at binding energies 459.8 eV and 465.5 eV, in agreement with the literature [36], is assigned to Ti (IV). Another contribution is Ti (III) from Ti_2O_3 species; the symmetric peaks of the corresponding doublet are situated at binding energies 458.2 eV and 463.7 eV, as reported in the literature [35]. Because the presence of reducing species (C and H) from organic radicals introduced by molecular precursors, TiO_2 synthesized under the present conditions is likely to be oxygen deficient. To maintain the charge neutrality the presence of oxygen vacancies will lead to the formation of lower valent Ti cations [37]. The contributions of Ti^{3+} in Ti 2p on the surface of MTiO_2/RRP and MTiO_2/GB samples are 42.6% and 20.8%, respectively. The result indicates that the Ti^{3+} ions content of MTiO_2/RRP is evidently higher than that of MTiO_2/GB , which is due to the fact that a large amount of carbon around the MTiO_2/RRP nanoparticles reduces TiO_2 to form more Ti^{3+} ions. The O1s XPS curve of MTiO_2/RRP has also a similar shape to MTiO_2/GB and could

be decomposed into several contributions in Figure 8(d). The main contribution is attributed to Ti–O (531.0 eV) in TiO_2 [38]. The other two kinds of oxygen contributions can be counted by the hydroxyl groups (532.6 eV) and the C–O bonds (533.5 eV), respectively. In addition to the three peaks a shoulder is present at 529.5 eV to the lower binding energy side, indicating the presence of different types of Ti–O species. Thus, Ti 2p and O 1s spectra confirm the presence of Ti^{3+} .

3.4. UV/Vis Spectrum. Figure 9 shows the diffuse reflectance UV-Vis spectra of two dyes templates, RRP and GB, and their corresponding titania samples, MTiO_2/RRP and MTiO_2/GB , as well as P25. Although RRP and GB exhibit absorption in the visible and UV region, RRP shows obviously higher absorption strength than GB in the range of 200–650 nm in Figure 9(a). Interestingly, as shown in Figure 9(b), the titania samples MTiO_2/RRP also exhibited higher absorption strength than MTiO_2/GB in visible region. Moreover, the band-gap-absorption onset of MTiO_2/RRP at the edge of the UV and visible-light range shows an apparent red-shift compared to MTiO_2/GB which only has slight shift in absorption spectra. Many investigations [15, 37] have found that organic impurities are still present in the TiO_2 , which could be responsible for the unusually high absorption of light. Regarding to MTiO_2/RRP , the incorporation of carbonaceous species formed during the calcination is a possible reason for the absorption tail in the visible-light region. On the one hand, carbonaceous species can effectively lower the band gap and make the absorption edge of TiO_2 shift to the visible-light range [15]. Therefore, the MTiO_2/RRP photocatalyst with lower band gap energies could absorb more visible light. On the other hand, according to the literature [37], these

carbon residues may occur in highly condensed and coke-like structure around TiO_2 nanoparticles, so it could play the role of sensitizer to induce the visible-light absorption and response. By contrast, P25 TiO_2 does not show any absorption in the visible region and considerable shift in absorption spectra as seen from Figure 9(b).

Due to the significant differences of the preparation processes between our sample and all of those which were prepared by using dyes as only photosensitizers, it is necessary to evoke some reasons why the mesoporous titanium dioxides (MTiO_2/RRP) prepared by using radish red pigment as templates exhibited the better visible-light photocatalytic activities. The formation of mesoporous metal oxides via such a simple procedure suggests again that radish red pigment molecular, like commercial dyes used in our previous works [14, 15], is the ideal building blocks for supramolecular chemistry. Although the mechanism details of the formation of mesoporous materials are still far from understood, its highly crystalline framework and high specific surface area can provide more active sites and adsorb more reactive species, which could be one of the reasons that MTiO_2/RRP affords the better activity toward photocatalytic reactions. On the other hand, both FTIR and XPS measurements in MTiO_2/RRP indicate the presence of carbon residues such as carbonaceous species formed during calcinations. The incorporation of carbonaceous species may be responsible for the unusually high photodegradation yield of MTiO_2/RRP under visible-light irradiation. Carbonaceous species can not only induce the visible-light absorption and response as a photosensitizer but also enhance the photoquantum efficiency. When the photocatalyst was excited under visible light, the carbonaceous species can also serve as an electron scavenger to protect the process of electron-hole recombination and that could be important because of the formation of low amount of free carriers [31]. In addition, it has also been reported [39] that Ti^{3+} surface states of TiO_2 should act as a photocatalytic active site for the photodegradation of dye molecules and hydrogen generation via water-splitting. However, in our works MTiO_2/GB with 20% Ti^{3+} ions does not show any visible-light photocatalytic activity for RB. The fact suggests that high visible-light activity of MTiO_2/RRP could mainly result from high carbonaceous species content rather than Ti^{3+} ion.

4. Conclusions

Visible-light responsive mesoporous anatase TiO_2 with highly crystalline framework was successfully synthesized by facile combine sol-gel chemistry and self-assembly routes, directly using RRP, a natural food coloring agent as template. The excellent visible-light driven photocatalytic performance of MTiO_2/RRP in the degradation of methyl orange and phenolic compounds are mainly attributed to its red shift of band-gap-absorption onset and visible-light response as a result of the incorporation of surface carbon species.

In summary, mesoporous titania prepared here was not modified with any transition metals or anions and show good visible-light photocatalytic activities for the degradation

of aqueous phase pollutants. This approach is simpler and potentially more stable than conventional photosensitization. Furthermore, the new mesoporous titania materials synthesized using natural food coloring agents as templates may be less toxic than those prepared by the toxic dyes. We believe that the synthetic strategy demonstrated here could be extended to other mesoporous materials. This could open up new uses for mesoporous titania in applications such as treatment of polluted water, dye-sensitized solar cells, or other regions.

Conflict of Interests

The authors declare that there is no conflict of interests regarding the publication of this paper.

Acknowledgment

The work was supported by the National Natural Science Funding (China, nos. 21367024, 21063016, and U1033603).

References

- [1] A. Kubacka, M. Fernández-García, and G. Colón, "Advanced nanoarchitectures for solar photocatalytic applications," *Chemical Reviews*, vol. 112, no. 3, pp. 1555–1614, 2012.
- [2] N. Todorova, T. Vaimakis, D. Petrakis et al., "N and N,S-doped TiO_2 photocatalysts and their activity in NO_x oxidation," *Catalysis Today*, vol. 209, pp. 41–46, 2013.
- [3] Z. Zheng, B. Huang, X. Qin, X. Zhang, Y. Dai, and M. H. Whangbo, "Facile in situ synthesis of visible-light plasmonic photocatalysts M@TiO_2 ($\text{M} = \text{Au}, \text{Pt}, \text{Ag}$) and evaluation of their photocatalytic oxidation of benzene to pheno l," *Journal of Material Chemistry*, vol. 21, no. 25, pp. 9079–9087, 2011.
- [4] M. Liang and J. Chen, "Arylamine organic dyes for dye-sensitized solar cells," *Chemical Society Reviews*, vol. 42, no. 8, pp. 3453–3488, 2013.
- [5] A. Venkateswararao, K. R. Justin Thomas, C. P. Lee, C. T. Li, and K. C. Ho, "Organic dyes containing carbazole as donor and p-Linker: optical, electrochemical, and photovoltaic properties," *ACS Applied Material & Interfaces*, vol. 6, no. 4, pp. 2528–2539, 2014.
- [6] P. Chowdhury, J. Moreira, H. Goma, and A. K. Ray, "Visible-solar-light-driven photocatalytic degradation of phenol with dye-sensitized TiO_2 : parametric and kinetic study," *Industrial and Engineering Chemistry Research*, vol. 51, no. 12, pp. 4523–4532, 2012.
- [7] H. Hubert, B. Michael, M. Peter, and T. Glztael, "Biophotovoltaics: natural pigments in dye-sensitized solar cells," *Applied Energy*, vol. 115, no. 3, pp. 216–225, 2014.
- [8] H. Zhou, L. Wu, Y. Gao, and T. Ma, "Dye-sensitized solar cells using 20 natural dyes as sensitizers," *Journal of Photochemistry and Photobiology A: Chemistry*, vol. 219, no. 2-3, pp. 188–194, 2011.
- [9] N. A. Ludin, A. M. A. Mahmoud, A. B. Mohamad, A. A. H. Kadhum, K. Sopian, and N. S. A. Karim, "Review on the development of natural dye photosensitizer for dye-sensitized solar cells," *Renewable and Sustainable Energy Reviews*, vol. 31, pp. 386–396, 2014.

- [10] G. Calogero, J.-H. Yum, A. Sinopoli, G. di Marco, M. Grätzel, and M. K. Nazeeruddin, "Anthocyanins and betalains as light-harvesting pigments for dye-sensitized solar cells," *Solar Energy*, vol. 86, no. 5, pp. 1563–1575, 2012.
- [11] A. Zyoud, N. Zaatari, I. Saadeddin et al., "Alternative natural dyes in water purification: anthocyanin as TiO₂-sensitizer in methyl orange photo-degradation," *Solid State Sciences*, vol. 13, no. 6, pp. 1268–1275, 2011.
- [12] C. F. J. Faul and M. Antonietti, "Facile synthesis of optically functional, highly organized nanostructures: dye-surfactant complexes," *Chemistry*, vol. 8, no. 12, pp. 2764–2768, 2002.
- [13] Y. Xu, Y. Cui, D. Jiang, D. Wu, and Y. H. Sun, "Dye-templating nonsurfactant synthesis of mesoporous silica," *Microporous and Mesoporous Materials*, vol. 109, no. 1–3, pp. 335–341, 2008.
- [14] W.-J. Gong, H.-W. Tao, G.-L. Zi et al., "Visible light photodegradation of dyes over mesoporous titania prepared by using chrome azurol S as template," *Research on Chemical Intermediates*, vol. 35, no. 6–7, pp. 751–760, 2009.
- [15] J. Wang, J. Wang, Q. Sun et al., "UV and solar light degradation of dyes over mesoporous crystalline titanium dioxides prepared by using commercial synthetic dyes as templates," *Journal of Materials Chemistry*, vol. 19, no. 36, pp. 6597–6604, 2009.
- [16] J.-M. Kong, L.-S. Chia, N.-K. Goh, T.-F. Chia, and R. Brouillard, "Analysis and biological activities of anthocyanins," *Phytochemistry*, vol. 64, no. 5, pp. 923–933, 2003.
- [17] T. Otsuki, H. Matsufuji, M. Takeda, M. Toyoda, and Y. Goda, "Acylation of anthocyanins from red radish (*Raphanus sativus* L.)," *Phytochemistry*, vol. 60, no. 1, pp. 79–87, 2002.
- [18] T. Sreethawong, Y. Suzuki, and S. Yoshikawa, "Photocatalytic evolution of hydrogen over nanocrystalline mesoporous titania prepared by surfactant-assisted templating sol-gel process," *Catalysis Communications*, vol. 6, no. 2, pp. 119–124, 2005.
- [19] J.-Y. Zheng, J.-B. Pang, K.-Y. Qiu, and Y. Wei, "Synthesis of mesoporous titanium dioxide materials by using a mixture of organic compounds as a non-surfactant template," *Journal of Materials Chemistry*, vol. 11, no. 12, pp. 3367–3372, 2001.
- [20] J. Wang, H. Fang, Y. Li, J. Li, and Z. Yan, "Liquid phase oxidation of *p*-chlorotoluene to *p*-chlorobenzaldehyde over cobalt-doped mesoporous titania with a crystalline framework," *Journal of Molecular Catalysis A: Chemical*, vol. 250, no. 1–2, pp. 75–79, 2006.
- [21] J. C. Yu, L. Zhang, Z. Zheng, and J. Zhao, "Synthesis and characterization of phosphated mesoporous titanium dioxide with high photocatalytic activity," *Chemistry of Materials*, vol. 15, no. 11, pp. 2280–2286, 2003.
- [22] Y. Wu, S. Liu, Y. Zuo, J. Li, and J. Wang, "Photodegradation of some dyes over Ce/FSM-16 catalyst under solar light," *Catalysis Letters*, vol. 119, no. 3–4, pp. 245–251, 2007.
- [23] M. Yoshinaga, M. Tanaka, and M. Nakatani, "Changes in anthocyanin content and composition of developing storage root of purple-fleshed sweet potato (*Ipomoea batatas* (L.) Lam)," *Breeding Science*, vol. 50, no. 1, pp. 59–64, 2000.
- [24] J.-M. Yoon, M.-H. Cho, J.-E. Park, Y.-H. Kim, T.-R. Hahn, and Y.-S. Paik, "Thermal stability of the pigments hydroxysafflor yellow A, safflor yellow B, and precarthamin from safflower (*Carthamus Tinctorius*)," *Journal of Food Science*, vol. 68, no. 3, pp. 839–843, 2003.
- [25] W. Winotapun, P. Opanasopit, T. Ngawhirunpat, and T. Rojanarata, "One-enzyme catalyzed simultaneous plant cell disruption and conversion of released glycoside to aglycone combined with in situ product separation as green one-pot production of genipin from gardenia fruit," *Enzyme and Microbial Technology*, vol. 53, no. 2, pp. 92–96, 2013.
- [26] K.-C. Chen, J.-Y. Wu, D.-J. Liou, and S.-C. J. Hwang, "Decolorization of the textile dyes by newly isolated bacterial strains," *Journal of Biotechnology*, vol. 101, no. 1, pp. 57–68, 2003.
- [27] T. Peng, D. Zhao, H. Song, and C. Yan, "Preparation of lanthana-doped titania nanoparticles with anatase mesoporous walls and high photocatalytic activity," *Journal of Molecular Catalysis A: Chemical*, vol. 238, no. 1–2, pp. 119–126, 2005.
- [28] M. Zheng, M. Gu, Y. Jin, and G. Jin, "Preparation, structure and properties of TiO₂-PVP hybrid films," *Materials Science and Engineering B: Solid-State Materials for Advanced Technology*, vol. 77, no. 1, pp. 55–59, 2000.
- [29] X. U. Zhao, Z. Li, Y. Chen, L. Shi, and Y. Zhu, "Solid-phase photocatalytic degradation of polyethylene plastic under UV and solar light irradiation," *Journal of Molecular Catalysis A: Chemical*, vol. 268, no. 1–2, pp. 101–106, 2007.
- [30] J. Yang, H. Bai, X. Tan, and J. Lian, "IR and XPS investigation of visible-light photocatalysis-Nitrogen-carbon-doped TiO₂ film," *Applied Surface Science*, vol. 253, no. 4, pp. 1988–1994, 2006.
- [31] M. Janus, M. Inagaki, B. Tryba, M. Toyoda, and A. W. Morawski, "Carbon-modified TiO₂ photocatalyst by ethanol carbonisation," *Applied Catalysis B: Environmental*, vol. 63, no. 3–4, pp. 272–276, 2006.
- [32] S. Doeuff, M. Henry, C. Sanchez, and J. Livage, "Hydrolysis of titanium alkoxides: modification of the molecular precursor by acetic acid," *Journal of Non-Crystalline Solids*, vol. 89, no. 1–2, pp. 206–216, 1987.
- [33] D. Jiang, Y. Xu, D. Wu, and Y. Sun, "Visible-light responsive dye-modified TiO₂ photocatalyst," *Journal of Solid State Chemistry*, vol. 181, no. 3, pp. 593–602, 2008.
- [34] H. Yang, S. Wu, Y. Duan, X. Fu, and J. Wu, "Surface modification of CNTs and enhanced photocatalytic activity of TiO₂ coated on hydrophilically modified CNTs," *Applied Surface Science*, vol. 258, no. 7, pp. 3012–3018, 2012.
- [35] Y. Park, W. Kim, H. Park, T. Tachikawa, T. Majima, and W. Choi, "Carbon-doped TiO₂ photocatalyst synthesized without using an external carbon precursor and the visible light activity," *Applied Catalysis B: Environmental*, vol. 91, no. 1–2, pp. 355–361, 2009.
- [36] N. C. Raut, T. Mathews, P. Chandramohan, M. P. Srinivasan, S. Dash, and A. K. Tyagi, "Effect of temperature on the growth of TiO₂ thin films synthesized by spray pyrolysis: structural, compositional and optical properties," *Materials Research Bulletin*, vol. 46, no. 11, pp. 2057–2063, 2011.
- [37] P. Górska, A. Zaleska, E. Kowalska et al., "TiO₂ photoactivity in vis and UV light: the influence of calcination temperature and surface properties," *Applied Catalysis B: Environmental*, vol. 84, no. 3–4, pp. 440–447, 2008.
- [38] N. K. Dey, M. J. Kim, K.-D. Kim et al., "Adsorption and photocatalytic degradation of methylene blue over TiO₂ films on carbon fiber prepared by atomic layer deposition," *Journal of Molecular Catalysis A: Chemical*, vol. 337, no. 1–2, pp. 33–38, 2011.
- [39] X. Liu, H. Xu, and L. R. Grabstanowicz, "Ti³⁺ self-doped TiO_{2-x} anatase nanoparticles via oxidation of TiH₂ in H₂O₂," *Catalysis Today*, vol. 225, pp. 80–89, 2014.

Research Article

Band-Gap Engineering of NaNbO_3 for Photocatalytic H_2 Evolution with Visible Light

Peng Li,¹ Hideki Abe,^{1,2,3} and Jinhua Ye^{1,2,4}

¹ Catalytic Materials Group, Environmental Remediation Materials Unit, National Institute for Materials Science (NIMS), 1-1 Namiki, Tsukuba, Ibaraki 305-0044, Japan

² TU-NIMS Joint Research Center, School of Materials Science and Engineering, Tianjin University, 92 Weijin Road, Nankai District, Tianjin 300072, China

³ PRESTO, Japan Science and Technology Agency (JST), 4-1-8 Honcho Kawaguchi, Saitama 332-0012, Japan

⁴ International Center for Materials Nanoarchitectonics (WPI-MANA), National Institute for Materials Science (NIMS), 1-1 Namiki, Tsukuba, Ibaraki 305-0044, Japan

Correspondence should be addressed to Hideki Abe; abe.hideki@nims.go.jp

Received 4 July 2014; Accepted 3 August 2014; Published 26 August 2014

Academic Editor: Wenjun Luo

Copyright © 2014 Peng Li et al. This is an open access article distributed under the Creative Commons Attribution License, which permits unrestricted use, distribution, and reproduction in any medium, provided the original work is properly cited.

A new visible light response photocatalyst has been developed for H_2 evolution from methanol solution by elemental doping. With lanthanum and cobalt dopants, the photoabsorption edge of NaNbO_3 was effectively shifted to the visible light region. It is also found that the photoabsorption edge is effectively controlled by the dopant concentration. Under visible light irradiation, H_2 was successfully generated over the doped NaNbO_3 samples and a rate of $12 \mu\text{mol}\cdot\text{h}^{-1}$ was achieved over $(\text{LaCo})_{0.03}(\text{NaNb})_{0.97}\text{O}_3$. Densityfunctional theory calculations show that Co-induced impurity states are formed in the band gap of NaNbO_3 and this is considered to be the origin of visible-light absorption upon doping with La and Co.

1. Introduction

Because of the current energy crisis and environmental pollution from the consumption of fossil fuels, new source which can provide a big amount of maintainable energy must be developed in hurry. H_2 is considered as a candidate of the next generation energy source because of its renewable, unlimited, and environmental friendly performances [1, 2]. However, there are still several barriers to realize the practical utilization of H_2 energy, and the produce of H_2 is the most serious one. As the present H_2 is mostly generated from the reformation of fossil fuel, a new method which can produce H_2 with clean energy should be developed [3]. Photocatalysis has been developed as a candidate that can satisfy the demand of supplying H_2 by splitting water with solar energy. In the past decades, a lot of photocatalysts were developed for producing H_2 with high efficiency. But most of the photocatalysts, such as TiO_2 , SrTiO_3 , and NaTaO_3 , have only UV light responsibility, and the low visible light utilization limited the practical

use of photocatalysis with solar light [4–6]. To improve the visible light absorption, the common method is doping with cations to adjust the electronic structures of photocatalysts [7]. When the cation dopants replace the positions of lattice cations or occupy the interstices in the crystal lattice, impurity energy levels might be generated within the band gap of the photocatalyst, which can extend the responsive region of photocatalytic reactions into visible light [8, 9].

NaNbO_3 is a typical nontoxic and highly stable semiconductor which has abundant applications in photocatalysis. In many reports, NaNbO_3 has been demonstrated to be a high efficiency photocatalyst for H_2 generation [10–17]. Under the irradiation of UV light, NaNbO_3 nanoparticles could reduce H_2O to H_2 with quite high efficiency with sacrificial agents [12]. Fiber-structured NaNbO_3 was also verified to be useful in splitting pure H_2O into H_2 and O_2 [10]. However, almost all the reported NaNbO_3 photocatalysts are only sensitive to the UV light. Although iridium doped NaNbO_3 was proved to be active in water splitting under visible light irradiation,

the efficiency is still low and this method needs precious metal [18]. To achieve visible light photoactivity of NaNbO_3 without previous metal dopant is still a big challenge. Cobalt, which is a typical transition element with partially occupied d state, is commonly used as dopant to improve the visible light responsibility of wide band-gap photocatalysts [19–22]. However, simply doping binary oxide with cobalt may increase the defect concentration and negatively affect the photocatalytic performance. Thus, codoping is more popular to balance the charge state and decrease the defects [23, 24]. In this work, we developed a series of NaNbO_3 doped with lanthanum and cobalt with H_2 evolution activity under visible light irradiation. The further theoretical study indicates that the cobalt dopant creates new states in the band gap of NaNbO_3 and provides the visible light absorption.

2. Experimental Section

2.1. Material Preparation. The samples were synthesized via a hydrothermal method [12]. In a typical synthesis of NaNbO_3 , 1.0 g of $(\text{C}_2\text{H}_5\text{O})_5\text{Nb}$ and 0.24 g of $\text{C}_2\text{H}_5\text{ONa}$ were added into 10 mL of 2-methoxyethanol and stirred at room temperature to form a clear colloid. Next, the mixture was stirred for 30 minutes and then heated to 120°C with a rate of $1^\circ\text{C}\cdot\text{min}^{-1}$ and maintained at this temperature until a dry gel was obtained. After that, 40 mL of 6 M NaOH solution was added to the powdered dry gel and stirred at room temperature to form a uniform precursor. Then, the mixture was transferred into a 50 mL Teflon sealed autoclave and heated at 180°C for 24 h. Finally, the product was washed with distilled water until pH was lower than 8.0 and the obtained powder was dried at 70°C overnight. To synthesize La, Co codoped NaNbO_3 , the dopant reagent $\text{La}(\text{CH}_3\text{COO})_3$, and $\text{Co}(\text{CH}_3\text{COO})_2$ were added in the first step and all the other procedures were the same.

2.2. Sample Characterization. The crystal structure of NaNbO_3 powder was determined by an X-ray diffractometer (Rint-2000, Rigaku Co., Japan) with Cu-K α radiation. The optical absorption spectra were measured with a UV-visible spectrophotometer (UV-2500PC, Shimadzu Co., Japan) using a BaSO_4 reference. Scanning electron microscopy images were recorded with a field emission scanning electron microscopy (JSM-6701F, JEOL Co., Japan) operated at 15 kV.

2.3. Photocatalytic H_2 Evolution. The H_2 evolution experiments were carried out in a gas closed circulation system. In a typical experiment, 0.3 g catalyst was dispersed by a magnetic stirrer in a CH_3OH solution (220 mL distilled water and 50 mL CH_3OH) in a Pyrex cell with a side window. Calculated amount of H_2PtCl_6 solution (0.5 wt%) was added into the solution. The light source used for cocatalyst deposition was a 300 W Xe arc lamp without filter ($\lambda > 300$ nm). After the H_2 evolution rate became constant, the system was evacuated and an L-42 cutoff filter was added to the 300 W Xe arc lamp ($\lambda > 420$ nm). The H_2 evolution was measured by an in situ gas chromatograph (GC-8A, Shimadzu Co., Japan) with a thermal conductivity detector (TCD).

2.4. Theoretical Calculation. The band structures, densities of state (DOS), and partial densities of state (PDOS) of NaNbO_3 and codoped NaNbO_3 were calculated using the plane-wave density functional theory (DFT) with the CASTEP program package [25]. The doping concentration was set to 3.125% by, respectively, replacing a Na atom and a Nb atom by a La and a Co atom in a $2 \times 2 \times 1$ supercell. The electronic state of Co was $[\text{Ar}]3d^6$ and high spin. The core electrons were replaced by ultrasoft pseudopotentials with a plane-wave basis cutoff energy of 410 eV, and the interactions of exchange and correlation were treated with Perdew-Burke-Ernzerhof parameterization (PBE) of the generalized gradient approximation (GGA). The FFT grids of basis in all the models were $40 \times 40 \times 108$ and the k -point sets of $3 \times 3 \times 1$ were used.

3. Results and Discussions

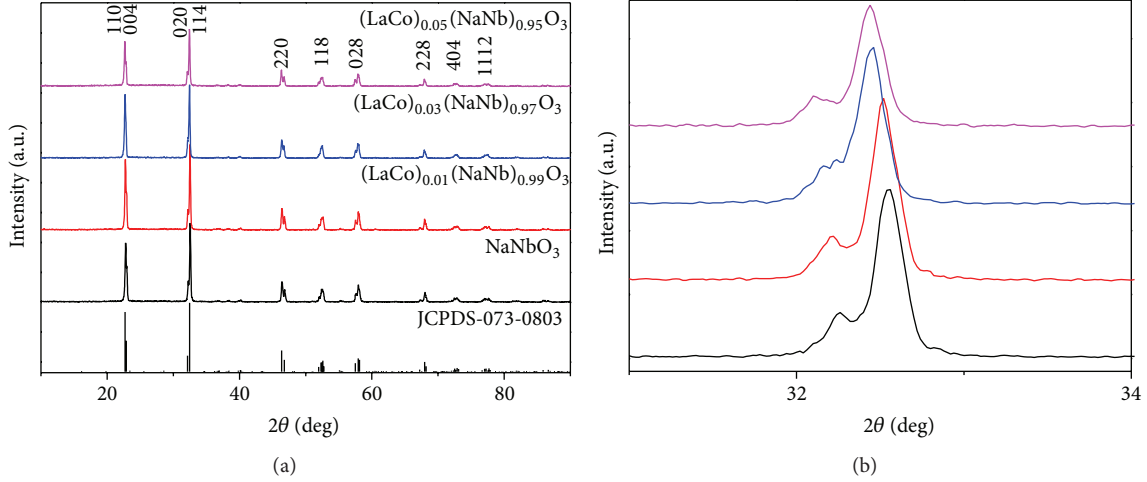
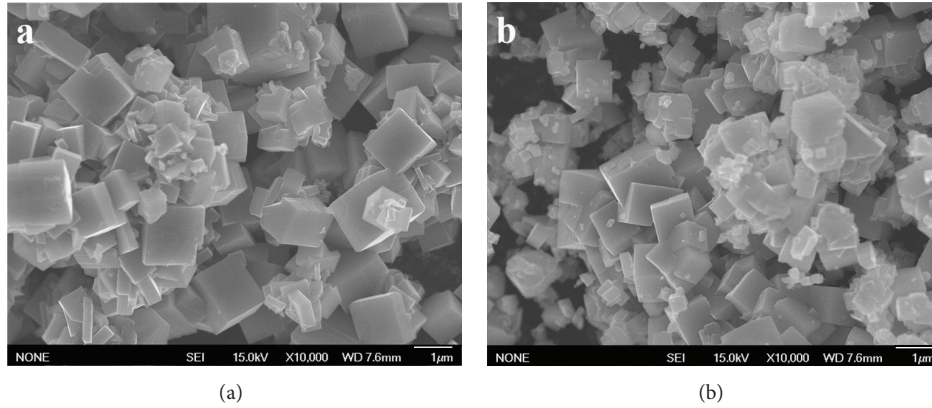
The crystallographic structures of all the synthesized NaNbO_3 samples were determined by X-ray diffraction (XRD) measurement (as shown in Figure 1(a)). All the observed diffraction peaks in the XRD patterns of NaNbO_3 and doped NaNbO_3 present good agreement with the reference data from the standard diffraction database (JCPDS-073-0803), showing that every sample was well crystalized in a single phase with the space group of $Pbcm$, which is the common phase of NaNbO_3 . However, slight shifts could be found when focusing on the particular diffraction peaks. Figure 1(b) gives the enlarged diffraction peaks with the highest intensity of NaNbO_3 and doped NaNbO_3 . When doping NaNbO_3 with La and Co, the diffraction peak shifts to the smaller diffraction angle, suggesting that the unit cell of NaNbO_3 has a slight expansion. As the radius changes from Na^+ (102 pm) and Nb^{5+} (64 pm) to La^{3+} (103.2 pm) and Co^{3+} (61 pm), such expansion of cell volume is understandable [26]. The XPS measurement (as shown in Figure S1 in Supplementary Material available online at <http://dx.doi.org/10.1155/2014/380421>) gives obvious evidence that the valance state of Co is +3 as no evident peak of Co^{2+} is observed [27]. The detailed lattice parameters of the as-prepared doped and undoped NaNbO_3 samples are shown in Table 1.

Since the morphology is an important factor which can greatly affect the photocatalytic performance, the scanning electron microscope (SEM) was further used to observe the morphology of the as-prepared samples and the SEM images of NaNbO_3 and $(\text{LaCo})_{0.05}(\text{NaNb})_{0.95}\text{O}_3$ are shown in Figure 2. The NaNbO_3 sample is constituted by particles with the cubic morphology, and the cubic particles are generally 300~1000 nm in length. The obtained NaNbO_3 has the similar morphology as the sample synthesized by hydrothermal reaction in the previous report [12]. Although the crystal structure changes a little after doping with La and Co, the crystal growth process has almost no change. The doped sample has the same morphology as the pure NaNbO_3 .

UV-visible absorption spectra of NaNbO_3 and La, Co codoped NaNbO_3 powder samples are shown in Figure 3(a). The pure NaNbO_3 sample only has an intense absorption

TABLE 1: Crystal structures of the as-prepared doped and undoped NaNbO_3 samples.

Materials	Crystal system	Lattice parameters (\AA)		
		a	b	c
NaNbO_3	Orthorhombic	5.5028(7)	5.5474(3)	15.4988(6)
$(\text{LaCo})_{0.01}(\text{NaNb})_{0.99}\text{O}_3$	Orthorhombic	5.5098(4)	5.5542(2)	15.5047(4)
$(\text{LaCo})_{0.03}(\text{NaNb})_{0.97}\text{O}_3$	Orthorhombic	5.5122(5)	5.5650(2)	15.5321(3)
$(\text{LaCo})_{0.05}(\text{NaNb})_{0.95}\text{O}_3$	Orthorhombic	5.5128(7)	5.5674(4)	15.5388(3)

FIGURE 1: (a) XRD patterns of the as-prepared NaNbO_3 and La, Co codoped NaNbO_3 compared with the standard NaNbO_3 XRD pattern. (b) The enlarged XRD patterns of the highest diffraction peak of NaNbO_3 .FIGURE 2: SEM images of the as-prepared (a) NaNbO_3 and (b) La, Co codoped NaNbO_3 .

with steep edges in the UV region. Different from the pure NaNbO_3 , the samples have evident absorptions in the visible light region. The optical band gaps E_g of the as-prepared NaNbO_3 samples were determined according to the following equation:

$$(\alpha h\nu)^n = A(h\nu - E_g), \quad (1)$$

in which α , ν , A , and E_g are absorption coefficient, light frequency, proportionality constant, and optical band gap, respectively [28]. The value of index n depends on the property of materials, whereas $n = 2$ for the direct transition

and $n = 1/2$ for the indirect transition. For NaNbO_3 , the index n was determined to be $1/2$ according to the relationship between $\lg(\alpha h\nu)$ and $\lg(h\nu - E_g)$. For La, Co codoped NaNbO_3 , the indexes n were determined to be 2. The different indexes of NaNbO_3 and doped NaNbO_3 indicate that NaNbO_3 is an indirect band-gap semiconductor, while the doped NaNbO_3 samples have direct transitions with visible light absorptions. From Figure 3(b), the values of the optical band gaps for NaNbO_3 , $(\text{LaCo})_{0.01}(\text{NaNb})_{0.99}\text{O}_3$, $(\text{LaCo})_{0.03}(\text{NaNb})_{0.97}\text{O}_3$, and $(\text{LaCo})_{0.05}(\text{NaNb})_{0.95}\text{O}_3$ are determined to be 3.42, 2.74, 2.70, and 2.65 eV, respectively.

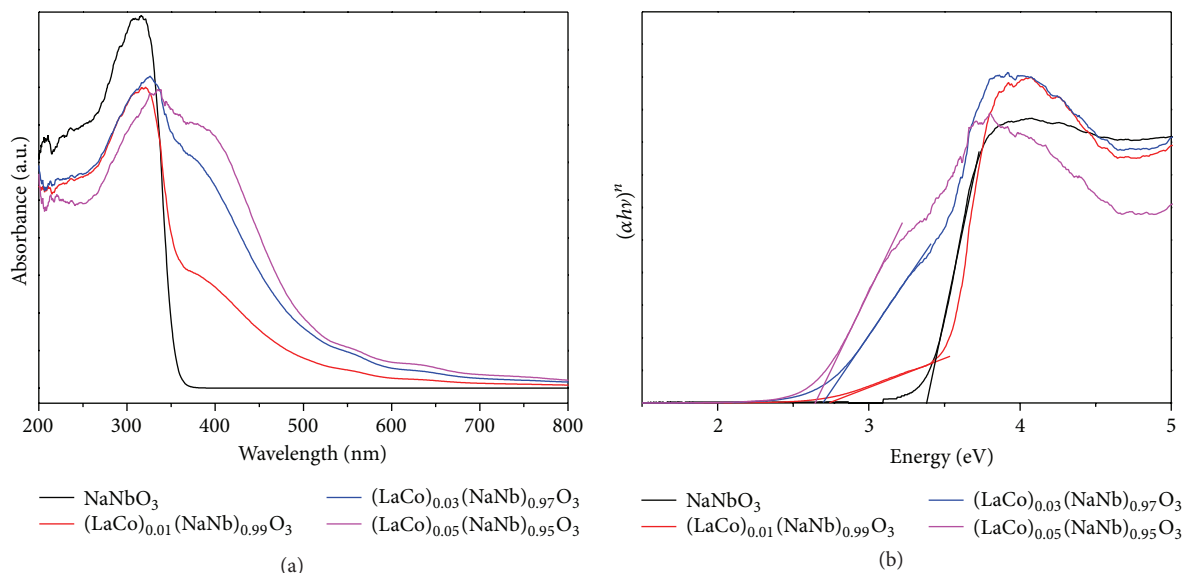


FIGURE 3: (a) UV-visible absorption spectra of the as-prepared NaNbO₃ and La, Co codoped NaNbO₃. (b) The corresponding $(\alpha h\nu)^n \sim h\nu$ curves of the as-prepared NaNbO₃ and La, Co codoped NaNbO₃.

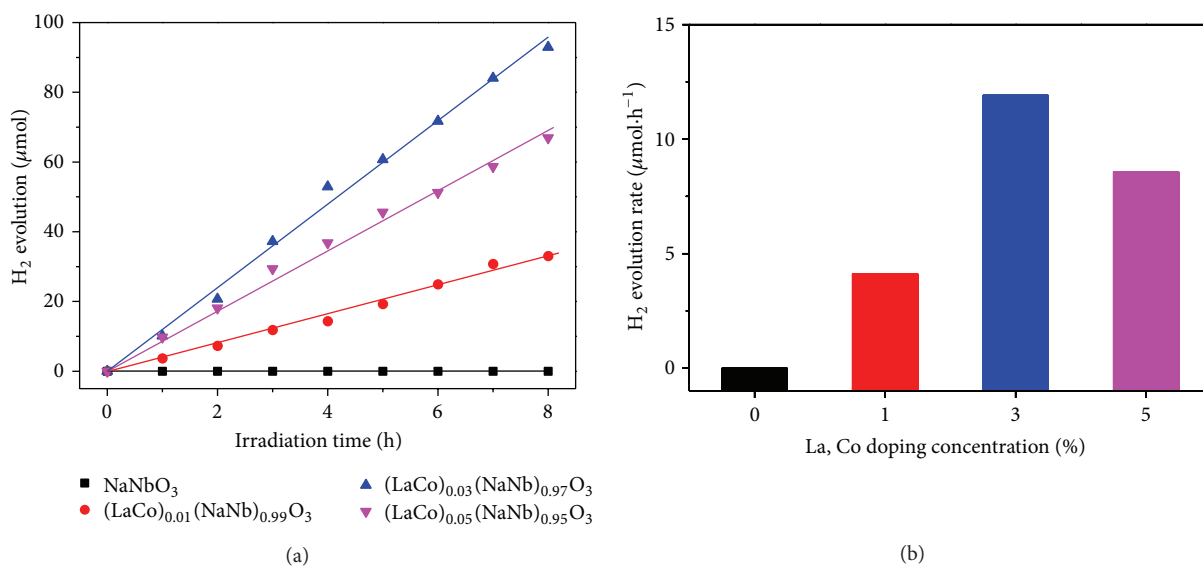


FIGURE 4: (a) Photocatalytic H₂ evolutions from the aqueous methanol solution over the as-prepared NaNbO₃ and La, Co codoped NaNbO₃ with 0.5 wt% Pt loading under the irradiation of visible light ($\lambda > 420$ nm). (b) The comparison of average photocatalytic H₂ evolution rates from the aqueous methanol solution over NaNbO₃ and La, Co codoped NaNbO₃ with 0.5 wt% Pt loading under the irradiation of visible light ($\lambda > 420$ nm).

With the increasing of doping concentration, the optical band gap of NaNbO₃ is continuously decreasing.

The H₂ evolutions from aqueous CH₃OH solution (50 mL CH₃OH + 220 mL H₂O) over NaNbO₃ and La, Co codoped NaNbO₃ (0.3 g) with 0.5 wt% Pt loading under the irradiation of visible light ($\lambda > 420$ nm) are presented in Figure 4(a). As shown by the UV-visible absorption in the previous part, NaNbO₃ has no visible light absorption. Under the irradiation of visible light, there is no H₂ detected during the experiment in 8 hours, while the doped NaNbO₃ samples exhibit photoactivities for H₂ evolution in the presence of methanol as sacrificial reagent. H₂ was generated

almost linearly over all the doped samples in 8 hours. As plotted in Figure 4(b), the H₂ evolution rates are significantly different: (LaCo)_{0.03}(NaNb)_{0.97}O₃ > (LaCo)_{0.05}(NaNb)_{0.95}O₃ > (LaCo)_{0.01}(NaNb)_{0.99}O₃. Over the best catalyst (LaCo)_{0.03}(NaNb)_{0.97}O₃, 11.9 μmol H₂ could be produced every hour.

To understand the mechanism of visible light photocatalytic activity of La, Co codoped NaNbO₃, theoretical calculation based on density functional theory (DFT) was carried out. The density of states (DOS) in Figure 5 indicates that the undoped NaNbO₃ has simple valence band maxima (VBM) and conduction band minima (CBM). Its VBM and CBM

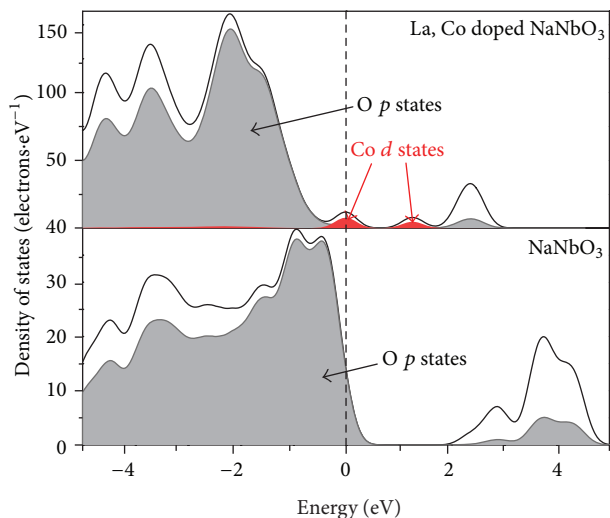


FIGURE 5: The calculated density of states and partial density of states of NaNbO_3 and La, Co codoped NaNbO_3 .

are mainly composed by O p states and Nb d states. Under light irradiation, the electrons are excited from O p orbitals to Nb d orbitals and the holes are left in O p orbitals. Then, the photogenerated electrons and holes migrate to the surface and react with water and sacrificial reagent, respectively. With La and Co doping, significant changes could be found with VBM and CBM. Two dopant states are observed between the original VBM and CBM, which narrow the band gap of doped NaNbO_3 and induce the visible light absorption and visible light response H_2 evolution activity. However, these two states are hybrid by Co d states and O p states and Co d states have larger combination ratio. Thus, the improved visible light absorption is mostly caused by the $d-d$ transition of Co. Since the electrons excited from d states to d states have a high backward transition rate, the photogenerated electrons could hardly migrate to the surface and perform photocatalytic reactions. This is the reason why the photoactivity of La, Co codoped NaNbO_3 under visible light is not as high as pure NaNbO_3 under UV light. The general mechanism of the visible light activity over La, Co codoped NaNbO_3 could be concluded in Figure 6. The doping with Co element creates new occupied and unoccupied energy levels in the band gap of NaNbO_3 . The transition between the new CBM and VBM could absorb visible and make the visible light photocatalytic reaction possible.

4. Conclusions

In conclusion, La, Co codoped NaNbO_3 were synthesized to realize the visible light response photocatalytic H_2 evolution. The doped NaNbO_3 samples showed narrower optical band gaps (2.65, 2.70, and 2.74 eV for $(\text{LaCo})_{0.05}(\text{NaNb})_{0.95}\text{O}_3$, $(\text{LaCo})_{0.03}(\text{NaNb})_{0.97}\text{O}_3$, and $(\text{LaCo})_{0.01}(\text{NaNb})_{0.99}\text{O}_3$, resp.) than the pure NaNbO_3 (3.42 eV). In photocatalytic H_2 evolution experiments, the doped NaNbO_3 samples showed activity under the visible light irradiation, while the undoped

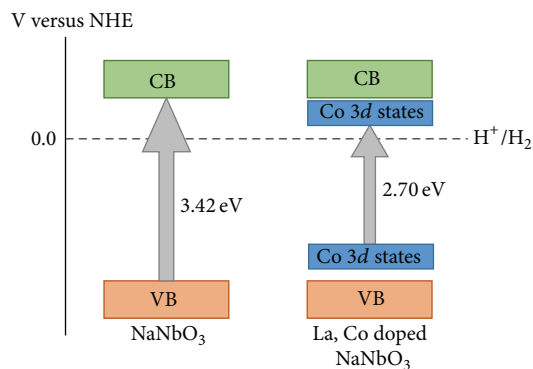


FIGURE 6: The schematic band structures of NaNbO_3 and La, Co codoped NaNbO_3 .

NaNbO_3 was not active. According to the theoretical calculation, the visible light activity of La, Co codoped NaNbO_3 could be attributed to the new impurity electronic states of Co dopant. Therefore, this work presented a new material for visible light photocatalytic H_2 evolution.

Conflict of Interests

The authors declare that there is no conflict of interests regarding the publication of this paper.

Acknowledgments

The authors thank Professor Naoto Umezawa for the result discussion and Dr. Akihiro Tanaka and Dr. Hideo Iwai of Materials Analysis Station of NIMS for the XPS measurement and analysis. This work was supported by Japan Science and Technology Agency (JST) and Precursory Research for Embryonic Science and Technology (PRESTO) program.

References

- [1] A. J. Bard and M. A. Fox, "Artificial photosynthesis: solar splitting of water to hydrogen and oxygen," *Accounts of Chemical Research*, vol. 28, no. 3, pp. 141–145, 1995.
- [2] T. J. Meyer, "Chemical approaches to artificial photosynthesis," *Accounts of Chemical Research*, vol. 22, pp. 163–170, 1989.
- [3] M. D. Hernández-Alonso, F. Fresno, S. Suárez, and J. M. Coronado, "Development of alternative photocatalysts to TiO_2 : challenges and opportunities," *Energy and Environmental Science*, vol. 2, no. 12, pp. 1231–1257, 2009.
- [4] Y. Yoshida, M. Matsuoka, S. C. Moon, H. Mametsuka, E. Suzuki, and M. Anpo, "Photocatalytic decomposition of liquid-water on the Pt-loaded TiO_2 catalysts: effects of the oxidation states of Pt-species on the photocatalytic reactivity and the rate of the back reaction," *Research on Chemical Intermediates*, vol. 26, no. 6, pp. 567–574, 2000.
- [5] H. Kato and A. Kudo, "New tantalate photocatalysts for water decomposition into H_2 and O_2 ," *Chemical Physics Letters*, vol. 295, no. 5–6, pp. 487–492, 1998.

- [6] K. Domen, S. Naito, M. Soma, T. Onishi, and K. Tamaru, "Photocatalytic decomposition of water vapour on an NiO–SrTiO₃ catalyst," *Journal of the Chemical Society, Chemical Communications*, no. 12, pp. 543–544, 1980.
- [7] H. Tong, S. Ouyang, Y. Bi, N. Umezawa, M. Oshikiri, and J. Ye, "Nano-photocatalytic materials: possibilities and challenges," *Advanced Materials*, vol. 24, no. 2, pp. 229–251, 2012.
- [8] J. Y. Cao, Y. J. Zhang, H. Tong, P. Li, T. Kako, and J. H. Ye, "Selective local nitrogen doping in a TiO₂ electrode for enhancing photoelectrochemical water splitting," *Chemical Communications*, vol. 48, pp. 8649–8651, 2012.
- [9] J. W. Shi, J. H. Ye, L. J. Ma, S. X. Ouyang, D. W. Jing, and L. J. Guo, "Site-selected doping of upconversion luminescent Er³⁺ into SrTiO₃ for visible-light-driven photocatalytic H₂ or O₂ evolution," *Chemistry*, vol. 18, no. 24, pp. 7543–7551, 2012.
- [10] H. F. Shi, X. K. Li, D. F. Wang, Y. P. Yuan, Z. G. Zou, and J. H. Ye, "NaNbO₃ nanostructures: facile synthesis, characterization, and their photocatalytic properties," *Catalysis Letters*, vol. 132, pp. 205–212, 2009.
- [11] P. Li, S. Ouyang, G. Xi, T. Kako, and J. Ye, "The effects of crystal structure and electronic structure on photocatalytic H₂ evolution and CO₂ reduction over two phases of perovskite-structured NaNbO₃," *The Journal of Physical Chemistry C*, vol. 116, no. 14, pp. 7621–7628, 2012.
- [12] G. Li, T. Kako, D. Wang, Z. Zou, and J. Ye, "Synthesis and enhanced photocatalytic activity of NaNbO₃ prepared by hydrothermal and polymerized complex methods," *Journal of Physics and Chemistry of Solids*, vol. 69, no. 10, pp. 2487–2491, 2008.
- [13] P. Li, H. Xu, L. Liu et al., "Constructing cubic-orthorhombic surface-phase junctions of NaNbO₃ towards significant enhancement of CO₂ photoreduction," *Journal of Materials Chemistry A*, vol. 2, no. 16, pp. 5606–5609, 2014.
- [14] N. Chen, G. Li, and W. Zhang, "Effect of synthesis atmosphere on photocatalytic hydrogen production of NaNbO₃," *Physica B*, vol. 447, pp. 12–14, 2014.
- [15] G. Li, W. Wang, N. Yang, and W. F. Zhang, "Composition dependence of AgSbO₃/NaNbO₃ composite on surface photovoltaic and visible-light photocatalytic properties," *Applied Physics A: Materials Science & Processing*, vol. 103, pp. 251–256, 2011.
- [16] G. Li, Z. Yi, Y. Bai, W. Zhang, and H. Zhang, "Anisotropy in photocatalytic oxidization activity of NaNbO₃ photocatalyst," *Dalton Transactions*, vol. 41, no. 34, pp. 10194–10198, 2012.
- [17] X. Li, G. Li, S. Wu, X. Chen, and W. Zhang, "Preparation and photocatalytic properties of platelike NaNbO₃ based photocatalysts," *Journal of Physics and Chemistry of Solids*, vol. 75, pp. 491–494, 2014.
- [18] A. Iwase, K. Saito, and A. Kudo, "Sensitization of NaMO₃ (M: Nb and Ta) photocatalysts with wide band gaps to visible light by Ir doping," *Bulletin of the Chemical Society of Japan*, vol. 82, pp. 514–518, 2009.
- [19] J. Choi, H. Park, and M. R. Hoffmann, "Effects of single metal-ion doping on the visible-light photoreactivity of TiO₂," *The Journal of Physical Chemistry C*, vol. 114, no. 2, pp. 783–792, 2010.
- [20] D. Dvoranova, V. Brezova, M. Mazur, and M. A. Malati, "Investigations of metal-doped titanium dioxide photocatalysts," *Applied Catalysis B*, vol. 37, no. 2, pp. 91–105, 2002.
- [21] M. Iwasaki, M. Hara, H. Kawada, H. Tada, and S. Ito, "Cobalt ion-doped TiO₂ photocatalyst response to visible light," *Journal of Colloid and Interface Scienc*, vol. 224, pp. 202–204, 2000.
- [22] B. Zhou, X. Zhao, H. Liu, J. Qu, and C. P. Huang, "Visible-light sensitive cobalt-doped BiVO₄ (Co-BiVO₄) photocatalytic composites for the degradation of methylene blue dye in dilute aqueous solutions," *Applied Catalysis B*, vol. 99, pp. 214–221, 2010.
- [23] Z. G. Yi and J. H. Ye, "Band gap tuning of Na_{1-x}La_xTa_{1-x}Co_xO₃ solid solutions for visible light photocatalysis," *Applied Physics Letters*, vol. 91, Article ID 254108, 2007.
- [24] Z. G. Yi and J. H. Ye, "Band gap tuning of Na_{1-x}La_xTa_{1-x}Cr_xO₃ for H₂ generation from water under visible light irradiation," *Journal of Applied Physics*, vol. 106, Article ID 074910, 2009.
- [25] M. D. Segall, P. J. D. Lindan, M. J. Probert et al., "First-principles simulation: ideas, illustrations and the CASTEP code," *Journal of Physics Condensed Matter*, vol. 14, no. 11, pp. 2717–2744, 2002.
- [26] R. Shannon, "Revised effective ionic radii and systematic studies of interatomic distances in halides and chalcogenides," *Acta Crystallographica A*, vol. 32, pp. 751–767, 1976.
- [27] M. C. Biesinger, B. P. Payne, A. P. Grosvenor, L. W. M. Lau, A. R. Gerson, and R. S. C. Smart, "Resolving surface chemical states in XPS analysis of first row transition metals, oxides and hydroxides: Cr, Mn, Fe, Co and Ni," *Applied Surface Science*, vol. 257, no. 7, pp. 2717–2730, 2011.
- [28] M. A. Butler, "Photoelectrolysis and physical properties of the semiconducting electrode WO₂," *Journal of Applied Physics*, vol. 48, pp. 1914–1920, 1977.

Research Article

Sensitization of Perovskite Strontium Stannate SrSnO_3 towards Visible-Light Absorption by Doping

Hungru Chen¹ and Naoto Umezawa^{1,2,3}

¹ Environmental Remediation Materials Unit, National Institute for Materials Sciences, Ibaraki Prefecture 305-0044, Japan

² PRESTO, Japan Science and Technology Agency (JST), 4-1-8 Honcho, Kawaguchi, Saitama Prefecture 332-0012, Japan

³ TU-NIMS Joint Research Center, School of Materials Science and Engineering, Tianjin University, 92 Weijin Road, Nankai District, Tianjin, China

Correspondence should be addressed to Naoto Umezawa; umezawa.naoto@nims.go.jp

Received 26 June 2014; Accepted 3 August 2014; Published 18 August 2014

Academic Editor: Wenjun Luo

Copyright © 2014 H. Chen and N. Umezawa. This is an open access article distributed under the Creative Commons Attribution License, which permits unrestricted use, distribution, and reproduction in any medium, provided the original work is properly cited.

Perovskite strontium stannate SrSnO_3 is a promising photocatalyst. However, its band gap is too large for efficient solar energy conversion. In order to sensitize SrSnO_3 toward visible-light activities, the effects of doping with various selected cations and anions are investigated by using hybrid density functional calculations. Results show that doping can result in dopant level to conduction band transitions which lie lower in energy compared to the original band gap transition. Therefore, it is expected that doping SrSnO_3 can induce visible-light absorption.

1. Introduction

Photocatalysis is an important technology for fuel production and environmental remediation from solar energy conversion [1–4]. Perovskite strontium stannate SrSnO_3 has been reported to be a promising photocatalyst [5–7]. Due to its suitable valence band and conduction band edge positions, it is able to split water into hydrogen and oxygen. The main drawback of SrSnO_3 is the large band gap of 4.1 eV [7] and therefore it can only absorb light in the ultraviolet region. A material for efficient solar energy conversion should be able to absorb the majority of the sunlight, namely, visible light. In order to sensitize wide gap materials to visible light, doping has been a common approach [8–10]. In this study, hybrid density functional theory calculations are carried out to investigate the effect of doping in SrSnO_3 . Cations Cr^{3+} , Fe^{3+} , and Rh^{3+} and anions N^{3-} , N^{2-} , and S^{2-} , which have been reported to be effective dopants for sensitizing titanates to visible light, are considered [10, 11].

2. Computational Methods

All calculations are carried out based on density functional theory [12] with the range separated HSE06 hybrid functional

[13]. Valence electrons are described by a plane wave basis set with the energy cutoff of 500 eV. The interactions between core and valence electrons are treated with the projector augmented wave (PAW) method [14]. The k-space is sampled with k-point spacing less than 0.03 \AA^{-1} . The lattice vectors and atomic positions in all cells are optimized until the force is converged to less than 0.03 eV-\AA^{-1} at each atomic position. Vienna ab initio simulation package (VASP) [15] is used for all calculations.

SrSnO_3 adopts the orthorhombic perovskite structure with space group symmetry $Pbnm$ [16], as shown in Figure 1. To model doped SrSnO_3 , a $2 \times 1 \times 2$ SrSnO_3 supercell, which contains 16 formula units (80 atoms), is constructed. Cation doping is simulated by substituting a dopant, Cr^{3+} , Fe^{3+} , or Rh^{3+} , for one Sn^{4+} , which corresponds to 6.25% of B-site cation impurity. To ensure the correct trivalent charge states of cation dopants, in each of the above cases La^{3+} is simultaneously substituted for Sr^{2+} . Anion doping is modeled by substituting a dopant, N^{3-} , N^{2-} , or S^{2-} , for one O^{2-} , which corresponds to 2.08% of anion impurity. In the N^{3-} case La^{3+} is simultaneously substituted for Sr^{2+} .

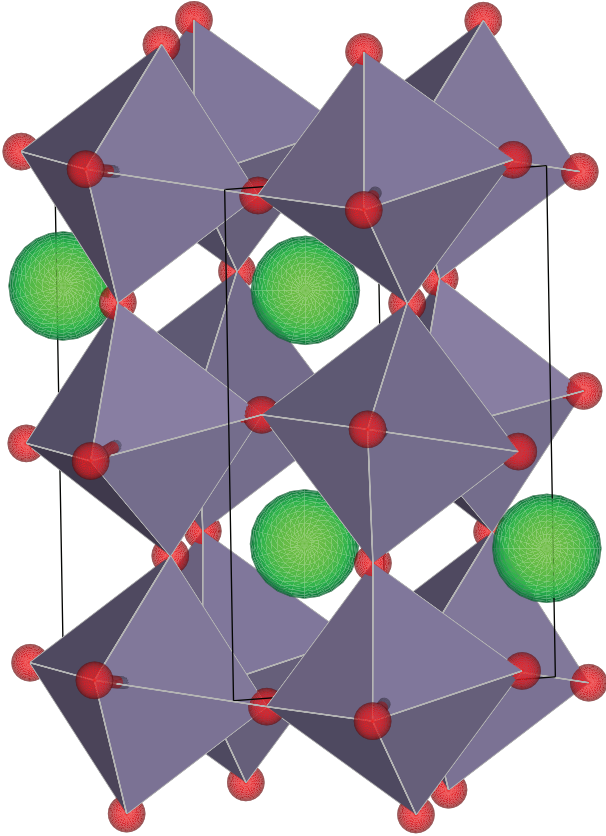


FIGURE 1: The orthorhombic perovskite structure of SrSnO_3 . The green and red spheres denote strontium and oxygen, respectively. The gray octahedra denote SnO_6 units.

3. Results and Discussions

The calculated lattice parameters for the orthorhombic perovskite SrSnO_3 are $a = 5.717 \text{ \AA}$, $b = 5.729 \text{ \AA}$, and $c = 8.084 \text{ \AA}$, which are in good agreement with experimental values $a = 5.709 \text{ \AA}$, $b = 5.703 \text{ \AA}$, and $c = 8.065 \text{ \AA}$ [17]. Figure 2 shows the density of states and band structure from our calculations. The calculated band gap of pristine SrSnO_3 is 3.52 eV, smaller than experimentally reported optical gap 4.1 eV. The origin of this 0.5 eV discrepancy is not clear at the moment. It could be an underestimation from the functional used in calculations. It could be that the transition from the highest occupied state to the lowest occupied state is forbidden [18]. More detailed analysis is necessary to clarify this. The bottom of the conduction band is a mixture of Sn 5s states and O 2p states. Different from d state conduction bands, it is very dispersive and therefore electrons in this band should possess lower effective mass than in d bands. The top of valence band is comprised mainly of oxygen 2p states.

Figure 3 shows the calculated density of states of cation and anion doped SrSnO_3 . It is assumed that dopants do not influence the position of the SrSnO_3 O 2p valence band and the top of O 2p valence band in each cell is aligned at 0 eV. In each case, dopant produces occupied states above the SrSnO_3 valence band maximum (VBM). This indicates the

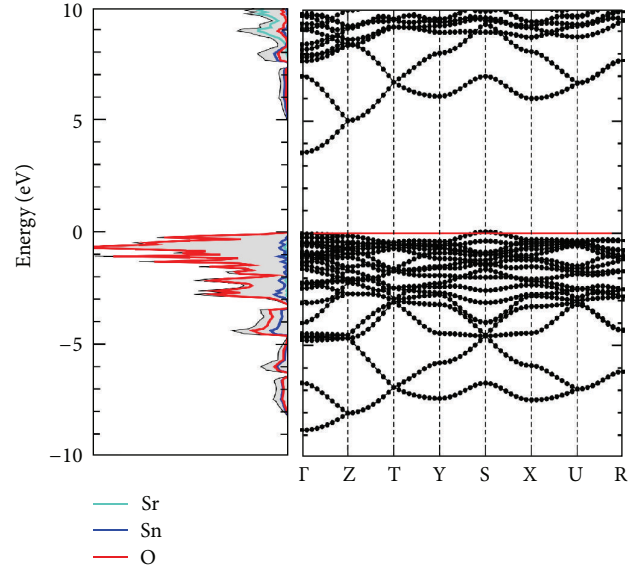


FIGURE 2: Calculated density of states and band structure of the pristine SrSnO_3 .

emergence of dopant to conduction band minimum (CBM) transitions. However, in the cases of Cr^{3+} , Fe^{3+} , and Rh^{3+} doping, the position of CBM is also shifted up by about 0.3 eV compared to pristine SrSnO_3 . This is probably due to the s state interaction between Sn^{4+} ions, which form the lowest part of conduction band, being disturbed by the presence of cation impurity. Overall, the $\text{Cr}^{3+} \rightarrow \text{CBM}$ and $\text{Rh}^{3+} \rightarrow \text{CBM}$ transitions are 3.21 eV and 2.63 eV, respectively. The position of Fe^{3+} states above VBM is relatively shallow and therefore the $\text{Fe}^{3+} \rightarrow \text{CBM}$ transition 3.53 eV is even higher in energy than the pristine SrSnO_3 band gap. In anion doping cases, the position of CBM is less affected. In the S^{2-} doping case, the CBM is actually downshifted by about 0.1 eV. Overall, the transitions from N^{2-} , N^{3-} , and S^{2-} to CBM are 2.94 eV, 2.45 eV, and 3.09 eV, respectively.

4. Conclusions

Through hybrid density functional calculations, it is shown that the doping of various cations and anions introduces occupied dopant states above the SrSnO_3 O 2p valence band. Transitions from these dopant states to the SrSnO_3 conduction band cost lower energies than the original band gap transition, apart from the Fe^{3+} case, and are hoped to contribute more towards visible-light photocatalytic activities. Among all considered cation dopants, Rh^{3+} gives rise to the deepest in gap states. The transition from Rh^{3+} to SrSnO_3 conduction band is 0.89 eV lower than the band gap. Among all considered anion dopants, N^{3-} appears to show the best result. The transition from N^{3-} to SrSnO_3 conduction band is 1.07 eV lower than the SrSnO_3 band gap. Nevertheless, one should be cautioned that whether or not dopant associated

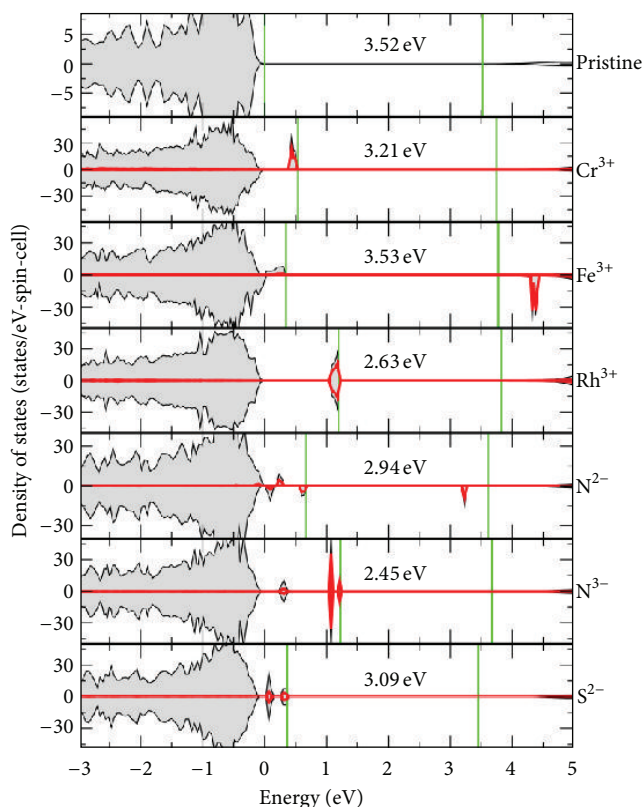


FIGURE 3: The calculated density of states in the pristine and doped cases. The shaded areas denote total density of states and the red lines denote the dopant states. The positions of the highest occupied state and the edge of conduction band minimum are marked by green lines. The magnitudes of the dopant to conduction band minimum transitions in each case are listed.

localized states can really contribute to steady-state activities is a question [8, 19].

Conflict of Interests

The authors declare that there is no conflict of interests regarding the publication of this paper.

Acknowledgments

This work is partly supported by the Japan Science and Technology Agency (JST) Precursory Research for Embryonic Science and Technology (PRESTO) program and by the World Premier International Research Center Initiative on Materials Nanoarchitectonics (MANA), MEXT.

References

[1] S. C. Roy, O. K. Varghese, M. Paulose, and C. A. Grimes, "Toward solar fuels: photocatalytic conversion of carbon dioxide to hydrocarbons," *ACS Nano*, vol. 4, no. 3, pp. 1259–1278, 2010.

[2] F. E. Osterloh and B. A. Parkinson, "Recent developments in solar water-splitting photocatalysis," *MRS Bulletin*, vol. 36, no. 1, pp. 17–22, 2011.

[3] M. R. Hoffmann, S. T. Martin, W. Choi, and D. W. Bahnemann, "Environmental applications of semiconductor photocatalysis," *Chemical Reviews*, vol. 95, no. 1, pp. 69–96, 1995.

[4] F. E. Osterloh, "Inorganic materials as catalysts for photochemical splitting of water," *Chemistry of Materials*, vol. 20, no. 1, pp. 35–54, 2008.

[5] D. Chen and J. Ye, "SrSnO₃ nanostructures: synthesis, characterization, and photocatalytic properties," *Chemistry of Materials*, vol. 19, no. 18, pp. 4585–4591, 2007.

[6] W. F. Zhang, J. Tang, and J. Ye, "Structural, photocatalytic, and photophysical properties of perovskite MSnO₃ (M = Ca, Sr, and Ba) photocatalysts," *Journal of Materials Research*, vol. 22, no. 7, pp. 1859–1871, 2007.

[7] W. F. Zhang, J. Tang, and J. Ye, "Photoluminescence and photocatalytic properties of SrSnO₃ perovskite," *Chemical Physics Letters*, vol. 418, no. 1–3, pp. 174–178, 2006.

[8] K. Mizushima, M. Tanaka, A. Asai, S. Iida, and J. B. Goodenough, "Impurity levels of iron-group ions in TiO₂(II)," *Journal of Physics and Chemistry of Solids*, vol. 40, no. 12, pp. 1129–1140, 1979.

[9] H. P. Maruska and A. K. Ghosh, "Transition-metal dopants for extending the response of titanate photoelectrolysis anodes," *Solar Energy Materials*, vol. 1, no. 3–4, pp. 237–247, 1979.

[10] R. U. E. 't Lam, L. G. J. de Haart, A. W. Wiersma, G. Blasse, A. H. A. Tinnemans, and A. Mackor, "The sensitization of SrTiO₃ photoanodes by doping with various transition metal ions," *Materials Research Bulletin*, vol. 16, no. 12, pp. 1593–1600, 1981.

[11] K. Iwashina and A. Kudo, "Rh-doped SrTiO₃ photocatalyst electrode showing cathodic photocurrent for water splitting under visible-light irradiation," *Journal of the American Chemical Society*, vol. 133, no. 34, pp. 13272–13275, 2011.

[12] P. Hohenberg and W. Kohn, "Inhomogeneous electron gas," vol. 136, pp. B864–B871, 1964.

[13] J. Heyd, G. E. Scuseria, and M. Ernzerhof, "Erratum: "Hybrid functionals based on a screened Coulomb potential" [J. Chem. Phys. 118, 8207 (2003)]," *The Journal of Chemical Physics*, vol. 124, no. 21, Article ID 219906, 2006.

[14] P. E. Blöchl, "Projector augmented-wave method," *Physical Review B*, vol. 50, no. 24, pp. 17953–17979, 1994.

[15] G. Kresse and J. Furthmüller, "Efficient iterative schemes for *ab initio* total-energy calculations using a plane-wave basis set," *Physical Review B—Condensed Matter and Materials Physics*, vol. 54, no. 16, pp. 11169–11186, 1996.

[16] E. H. Mountstevens, S. A. T. Redfern, and J. P. Attfield, "Order-disorder octahedral tilting transitions in SrSnO₃ perovskite," *Physical Review B*, vol. 71, no. 22, Article ID 220102, 2005.

[17] M. A. Green, K. Prassides, P. Day, and D. A. Neumann, "Structure of the $n = 2$ and $n = \infty$ member of the Ruddlesden-Popper series, Sr_(n+1)Sn_nO_{3n+1}," *International Journal of Inorganic Materials*, vol. 2, no. 1, pp. 35–41, 2000.

[18] V. T. Agekyan, "Spectroscopic properties of semiconductor crystals with direct forbidden energy gap," *Physica Status Solidi A*, vol. 43, no. 1, pp. 11–42, 1977.

[19] J. B. Goodenough, A. Hamnett, M. P. Dare-Edwards, G. Campet, and R. D. Wright, "Inorganic materials for photoelectrolysis," *Surface Science*, vol. 101, no. 1–3, pp. 531–540, 1980.

Research Article

Development of Thin Film Amorphous Silicon Tandem Junction Based Photocathodes Providing High Open-Circuit Voltages for Hydrogen Production

F. Urbain,¹ K. Wilken,¹ V. Smirnov,¹ O. Astakhov,¹ A. Lambertz,¹ J.-P. Becker,¹
U. Rau,¹ J. Ziegler,² B. Kaiser,² W. Jaegermann,² and F. Finger¹

¹ IEK-5 Photovoltaik, Forschungszentrum Jülich, 52425 Jülich, Germany

² Institute of Materials Science, TU Darmstadt, 64287 Darmstadt, Germany

Correspondence should be addressed to F. Urbain; f.urbain@fz-juelich.de

Received 13 March 2014; Revised 24 June 2014; Accepted 30 June 2014; Published 16 July 2014

Academic Editor: Wenjun Luo

Copyright © 2014 F. Urbain et al. This is an open access article distributed under the Creative Commons Attribution License, which permits unrestricted use, distribution, and reproduction in any medium, provided the original work is properly cited.

Hydrogenated amorphous silicon thin film tandem solar cells (a-Si:H/a-Si:H) have been developed with focus on high open-circuit voltages for the direct application as photocathodes in photoelectrochemical water splitting devices. By temperature variation during deposition of the intrinsic a-Si:H absorber layers the band gap energy of a-Si:H absorber layers, correlating with the hydrogen content of the material, can be adjusted and combined in a way that a-Si:H/a-Si:H tandem solar cells provide open-circuit voltages up to 1.87 V. The applicability of the tandem solar cells as photocathodes was investigated in a photoelectrochemical cell (PEC) measurement set-up. With platinum as a catalyst, the a-Si:H/a-Si:H based photocathodes exhibit a high photocurrent onset potential of 1.76 V versus the reversible hydrogen electrode (RHE) and a photocurrent of 5.3 mA/cm² at 0 V versus RHE (under halogen lamp illumination). Our results provide evidence that a direct application of thin film silicon based photocathodes fulfills the main thermodynamic requirements to generate hydrogen. Furthermore, the presented approach may provide an efficient and low-cost route to solar hydrogen production.

1. Introduction

Solar based hydrogen production via photoelectrochemical water splitting provides an alluring route to convert solar energy into a storable and clean chemical fuel and, therefore, increasingly plays a decisive role in sustainable energy concepts [1, 2]. Among the current variety of photoelectrode absorber materials for integrated water splitting devices, including III–V semiconductors [3–6], metal oxides [7–9], or crystalline silicon [10–12], amorphous silicon thin films emerge as a novel promising candidate [9, 13–16]. Overall, thin film silicon technology stands out as an attractive choice for water splitting applications, because it combines low-cost production, earth abundance, and versatility [17].

Amorphous silicon tandem solar cells have been intensively developed in the past, with major focus on high conversion efficiencies [18]. In our approach here, however, the focus is on the development of high V_{OC} devices, suitable

for water splitting applications. Therefore, we will describe a development route to achieve high voltage devices and emphasize which particular parameter regimes are optimal in order to achieve high open-circuit voltages in a-Si:H/a-Si:H tandem junction solar cells. Additionally it will be shown that the parameters can be systematically adjusted to tune the V_{OC} values in the range between 1.60 V and 1.87 V, which is relevant if one considers various PEC systems with different overpotential losses, that is, when different voltage requirements are implied. The major part of the reported a-Si:H tandem solar cells for water splitting applications was merely designed to provide additional bias to a photoactive metal oxide electrode [9, 14, 16]. In contrast, this study reports on the direct application of the a-Si:H tandem solar cells as all-silicon photoelectrodes for driving the water splitting reactions.

Regarding solar assisted water electrolysis and the concomitant requirement of electrochemical potentials, that is,

photovoltages above 1.23 V (disregarding overpotentials) [19–21], photocathodes providing high photocurrent at high voltages are desirable. Concerning this, great importance is given to the versatility of the a-Si:H material. By changing deposition process parameters, the electronic and optical properties of the a-Si:H absorber material can be adjusted, such that a wide range of high open-circuit voltages is provided in a-Si:H based single junction solar cells, without significantly impairing current densities [22, 23]. In comparison, other photocathode material systems listed above often suffer from rather low photovoltages and therefore limit the solar to hydrogen efficiency. The open-circuit voltage of a properly designed solar cell mainly depends on the band gap of the absorber layer. Thus, attempts for the variation in band gap energy of intrinsic a-Si:H absorber layers were made in this study. In real photoelectrochemical assemblies, the potential losses inevitably exceed 200 mV, depending on the current densities and catalysts used [24, 25]. Thus, for self-contained solar water splitting devices photovoltages of at least 1.43 V are needed. In this manner, a-Si:H based solar cells are very beneficial, because the electronic properties of individual a-Si:H absorber layers can be combined by connecting two single junction cells (subcells) in series. In this configuration a-Si:H/a-Si:H tandem junction solar cells promote a further extended range of achievable high voltages [26, 27]. Thus, they may satisfy the specific thermodynamic requirements of different photoelectrochemical systems.

Based on (photo-)electrochemical experiments, the performance and stability of the developed a-Si:H/a-Si:H tandem junction based photocathodes were evaluated with respect to the hydrogen evolution reaction (HER). Moreover, to fully explore the performance of the photocathode, platinum was evaporated as a catalyst.

2. Experimental Details

2.1. Preparation of a-Si:H Layers and Solar Cells. All a-Si:H layers were deposited by a plasma enhanced chemical vapor deposition (PECVD) technique in a multichamber system. For the intrinsic a-Si:H absorber layers a mixture of silane (SiH_4) and hydrogen (H_2) gases was used. For the n- and p-type layers, trimethylborane (TMB), methane (CH_4), and phosphine (PH_3) gases were added to the silane-hydrogen mixture. An excitation frequency of 13.56 MHz was applied for all depositions. The a-Si:H material optimization was mainly performed as a function of the substrate temperature T_s and silane concentration SC, defined as the ratio between the SiH_4 flow and the total gas flow. Single junction and tandem junction solar cells were made in a p-i-n and in a p-i-n-p-i-n superstrate configuration, respectively, with a sputtered zinc oxide/silver (ZnO/Ag) reflecting back contact [28] defining the area (1 cm^2) of the individual cells. The thickness of the intrinsic a-Si:H layer in single junction solar cells was kept constant at 400 nm. In the standard tandem device, the bottom cell thickness was 400 nm and the top cell thickness was 110 nm. The p- and n-doped layers are the same for all fabricated solar cells and are deposited at a substrate temperature of 180°C . Since T_s is varied for the deposition of the intrinsic a-Si:H layer, a waiting time of 30

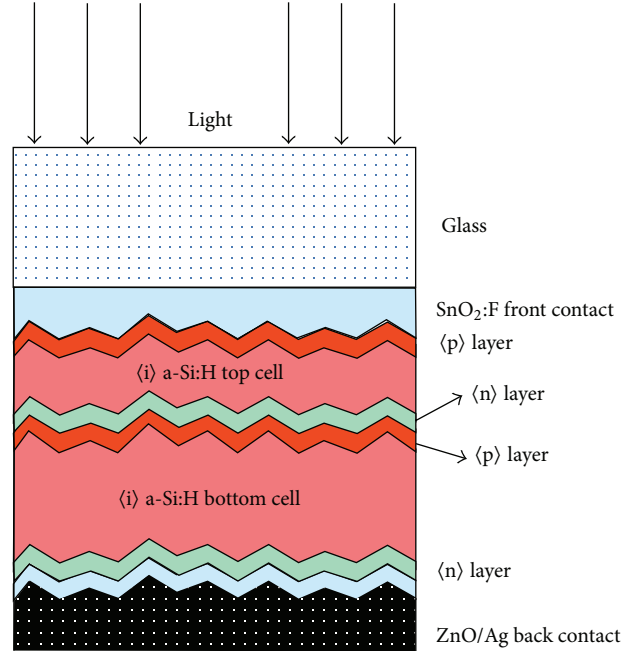


FIGURE 1: Schematic drawing of the layer stack used for the deposition of a-Si:H/a-Si:H tandem solar cells.

minutes between the layer deposition was implemented in order to maintain a required temperature of the substrate. All solar cells were deposited on 100 cm^2 fluorine-doped tin oxide ($\text{SnO}_2\text{:F}$) coated glass substrates with a native texture (Asahi U). Figure 1 schematically shows the tandem junction solar cell configuration used in the photovoltaic arrangement. For the investigation of the intrinsic a-Si:H layers alone, glass substrate (type Corning Eagle XG) and crystalline silicon wafers were used as substrates and all respective single a-Si:H layers had a thickness of approximately 500 nm. For the photoelectrochemical arrangement, 50 nm of platinum was deposited on the ZnO/Ag back contact by electron beam evaporation.

2.2. Characterization of Materials and Solar Cells. Infrared (IR) absorption measurements were carried out, using a Fourier transform spectrometer (type Nicolet 5700), to evaluate the hydrogen content c_{H} in the intrinsic a-Si:H layer. IR transmission was measured between 400 and 2400 cm^{-1} . This spectrum was normalized to the spectrum of the crystalline silicon wafer substrate.

Photothermal deflection spectroscopy (PDS) was performed to measure the absorption spectra of the intrinsic a-Si:H layers, which were deposited on glass substrates. From these spectra the gap energy E_{04} with a PDS absorption coefficient of 10^4 cm^{-1} was extracted, which serves as a measure for the optical band gap of the intrinsic a-Si:H layer.

The constant photocurrent method (CPM) was used to evaluate the absorption within the band gap (e.g., subgap absorption), which can be linked to the defect density of the a-Si:H material. The corresponding defect absorption densities

of the a-Si:H intrinsic layers were determined by using the absorption coefficient $\alpha_{1.2}$ at an energy of 1.2 eV [29].

Solar cells were characterized by current-voltage (J - V) measurements under AM 1.5 illumination using a double source (Class A) sun simulator and by quantum efficiency (QE) measurements.

2.3. Photoelectrochemical Measurements. The photoelectrochemical performance of the electrodes was evaluated at room temperature in an aqueous 0.1 M sulfuric acid (H_2SO_4) electrolyte solution (pH 1) using a three-electrode configuration [30]. The potential of the working electrode was controlled by a potentiostat (μ Autolab Type III). For illumination, a 150 W xenon-halogen lamp was used, which was calibrated (by adjusting the current) with a crystalline silicon diode to provide a light intensity of 100 mW cm^{-2} . The solar cells were illuminated through the glass substrate. The set-up of the electrochemical cell (type Zahner PECC-2) consists of a Teflon cell body and three electrodes: a working electrode (optimized a-Si:H/a-Si:H tandem junction solar cell, 8 mm diameter), a coiled platinum wire as a counter electrode, and a Ag/AgCl reference electrode being in contact with 3 M sodium chloride (NaCl) [0.268 V versus normal hydrogen electrode (NHE)]. For simplicity, the entire set-up will be denoted as photoelectrochemical cell (PEC) arrangement hereafter. Cyclic voltammetry measurements were performed with a scan rate of 30 mV s^{-1} . Electrical contact to the SnO_2 coated substrate, that is, the front contact of the solar cell, was made by a silver paste.

3. Results and Discussion

3.1. Material Properties of Intrinsic a-Si:H Absorber Layer. Since the band gap of amorphous a-Si:H correlates with the hydrogen content of the material [22], FTIR measurements were conducted to estimate the amount of hydrogen in the samples. Figure 2 shows the hydrogen content as a function of the substrate temperature for a-Si:H layers with different silane concentrations. The general trend indicates that a decrease in T_s results in an increase of c_H . This behavior can be attributed to the increased desorption of hydrogen at higher substrate temperatures. As deposition temperature increases, the desorption of hydrogen atoms is energetically favored and thus less hydrogen is incorporated into the layer [31]. No clear dependency of c_H on the silane concentration in the chosen range was visible in FTIR data. The hydrogen content in all samples investigated is between 10.6% and 16.8%.

For the determination of the band gap energy of the a-Si:H material, absorption spectra for different T_s and SC are measured and subsequently evaluated, with respect to E_{04} as an estimation of the band gap. The evaluated E_{04} values for all samples are shown in Figure 3. In the considered temperature range the band gap energy E_{04} decreases by approximately 80 meV with increasing T_s for a given SC. Additionally, a slight dependency of the E_{04} on SC can be extracted. For constant T_s , an average difference of approximately 30 meV between SC of 4% and 10% was observed. Considering all

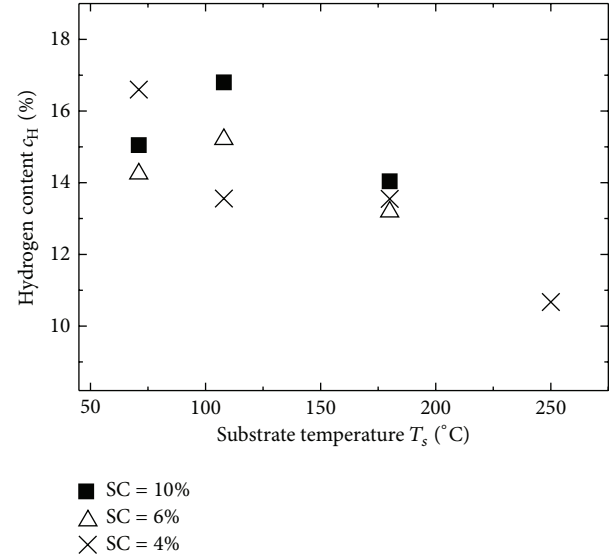


FIGURE 2: Hydrogen content as a function of the substrate temperature during deposition of the a-Si:H layers, with different silane concentrations.

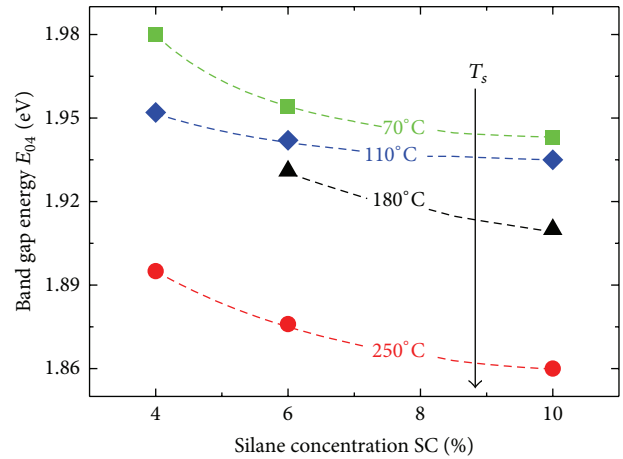


FIGURE 3: E_{04} band gap as a function of silane concentrations for a-Si:H layers deposited at different substrate temperatures T_s . The dotted lines are to guide the eye.

a-Si:H absorber layers, the optical band gap could be varied by 120 meV from 1.86 eV to 1.98 eV.

Figure 4 presents the evaluated E_{04} values as a function of c_H for different silane concentrations. The data of this study is in line with the commonly observed trend for an increase of the band gap energy with increasing fraction of bound hydrogen in the a-Si:H material [32–34]. A possible explanation suggested that the hydrogen could be involved in breaking of weak Si–Si bonds responsible for the states in the top of the valence band. As a consequence, by increasing c_H , stronger Si–H bonds emerge, leading to states deep in the valence band and resulting in the valence band edge being shifted down. The conduction band remains unaffected and thus, the band gap energy increases [22, 32]. Other microscopic models involve a discussion of the effects of nanosized

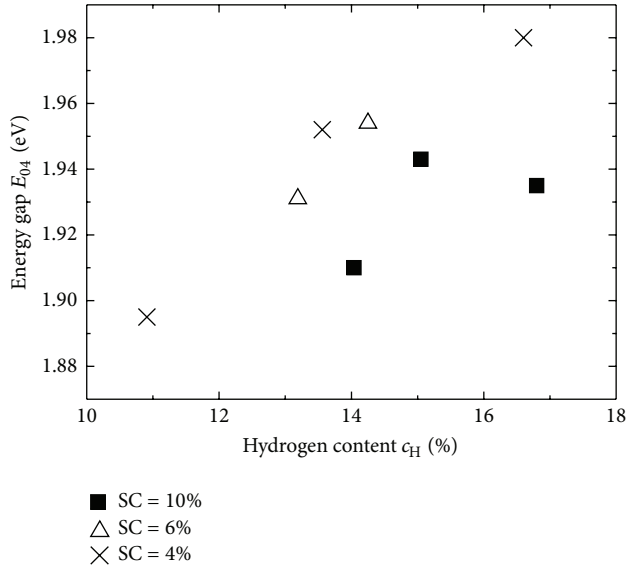


FIGURE 4: Band gap energy E_{04} as a function of the hydrogen content of deposited a-Si:H layers with different silane concentrations.

void configurations on the hydrogen incorporation in a-Si:H material [35, 36].

The defect density is an important parameter for absorber materials, because electronic defects can act as recombination centers and lead to a deterioration of the device performance [37, 38]. In general, it is well accepted that a reduction in the deposition temperature (below 250°C) results in the increase in the defect density of a-Si:H material [31]. Here, by adjusting SC together with T_s , we can maintain a material with a reasonable electronic quality (low defect density) even at a very low deposition temperature of around 70°C. Figure 5 shows the absorption at an energy of 1.2 eV as a function of T_s for different SC of the a-Si:H layers. It is apparent that for substrate temperatures between 110°C and 250°C the absorption in the subgap region is similar for different silane concentrations investigated here and $\alpha_{1,2}$ ranges between 4.2 cm⁻¹ and 8.5 cm⁻¹. At a temperature of 70°C, a distinct trend of decreasing $\alpha_{1,2}$ with decreasing silane concentration was observed. The defect absorption in this region rapidly increases up to 28 cm⁻¹ for SC of 10%. By reducing SC of the a-Si:H layers deposited at 70°C, $\alpha_{1,2}$ continuously decreases to 6.5 cm⁻¹ for SC of 4%. This value is similar to $\alpha_{1,2}$ values of the layers deposited at higher temperatures. Hence, this result emphasizes that the electronic quality of the a-Si:H material deposited at low substrate temperatures (around 70°C) can be improved, in terms of defect absorption density, by using lower silane concentrations during the deposition. We note that even at low SC of 4%, the materials are still fully amorphous as evident from the Raman scattering experiments.

3.2. Solar Cells

3.2.1. Single Junction Solar Cells. The investigated intrinsic a-Si:H absorber layers with different band gaps were subsequently applied in single junction solar cells in a p-i-n

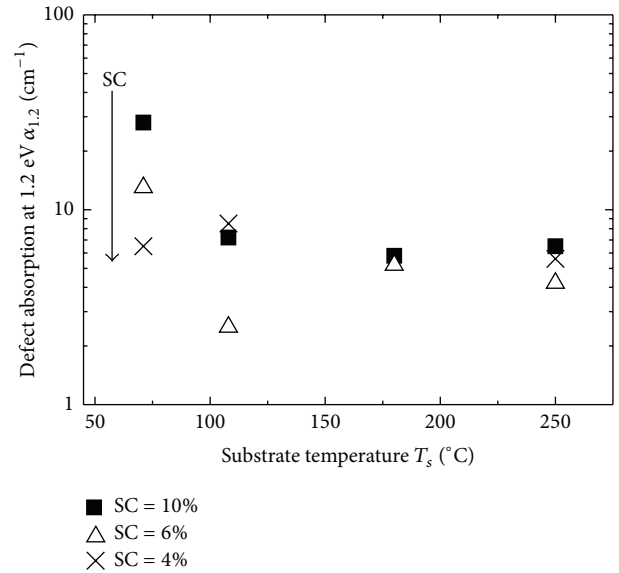


FIGURE 5: Absorption coefficient at 1.2 eV as a function of substrate temperature for different silane concentrations of the intrinsic a-Si:H layer.

configuration. The solar cells were prepared with intrinsic a-Si:H layers at silane concentrations of 4% and 10%, in order to consider the entire range of E_{04} absorber layer band gaps (from 1.86 eV to 1.98 eV) for the relevant temperatures, shown in Figure 3.

The performance of the a-Si:H solar cells as a function of T_s is shown in Figure 6. Reducing T_s from 250°C down to 110°C, the open-circuit voltage V_{OC} increases with decreasing T_s and can be varied from 802 mV up to a value of 946 mV, achieved in the case of an absorber layer with SC of 4% and T_s of 130°C (Figure 6(b)). In this temperature range (250°C–110°C), the fill factor FF is only slightly affected and varies between 68.5% and 73.8% for SC of 10% and between 70.2% and 74.2% for SC of 4% (Figure 6(c)). The best efficiency η of 10.3% is obtained with an intrinsic a-Si:H layer with SC of 10%, deposited at 180°C (Figure 6(a)).

For even lower T_s of 70°C all performance parameters tend to deteriorate considerably, as compared with the solar cells deposited at T_s of 110°C or above. In the 70°C temperature region increased defect absorption density $\alpha_{1,2}$ (Figure 5.) and higher optical band gap E_{04} (Figure 3) significantly impair the electronic material quality. Nevertheless, as already apparent in the previous section, through the use of lower SC during low-temperature deposition, a significant improvement of the optoelectronic properties of a-Si:H material can be achieved. When SC is reduced down to 4%, a significant improvement in V_{OC} and FF is observed in the case of solar cells deposited at temperatures below 180°C. At T_s of 70°C and SC of 4%, all parameters are enhanced, compared to the 70°C cell with SC of 10%, and η yields 7.7% (Figure 6(a)). This underlines that a combination of low deposition temperature together with reduced SC of the absorber layer is necessary to obtain high voltage solar cells with appropriate efficiency level.

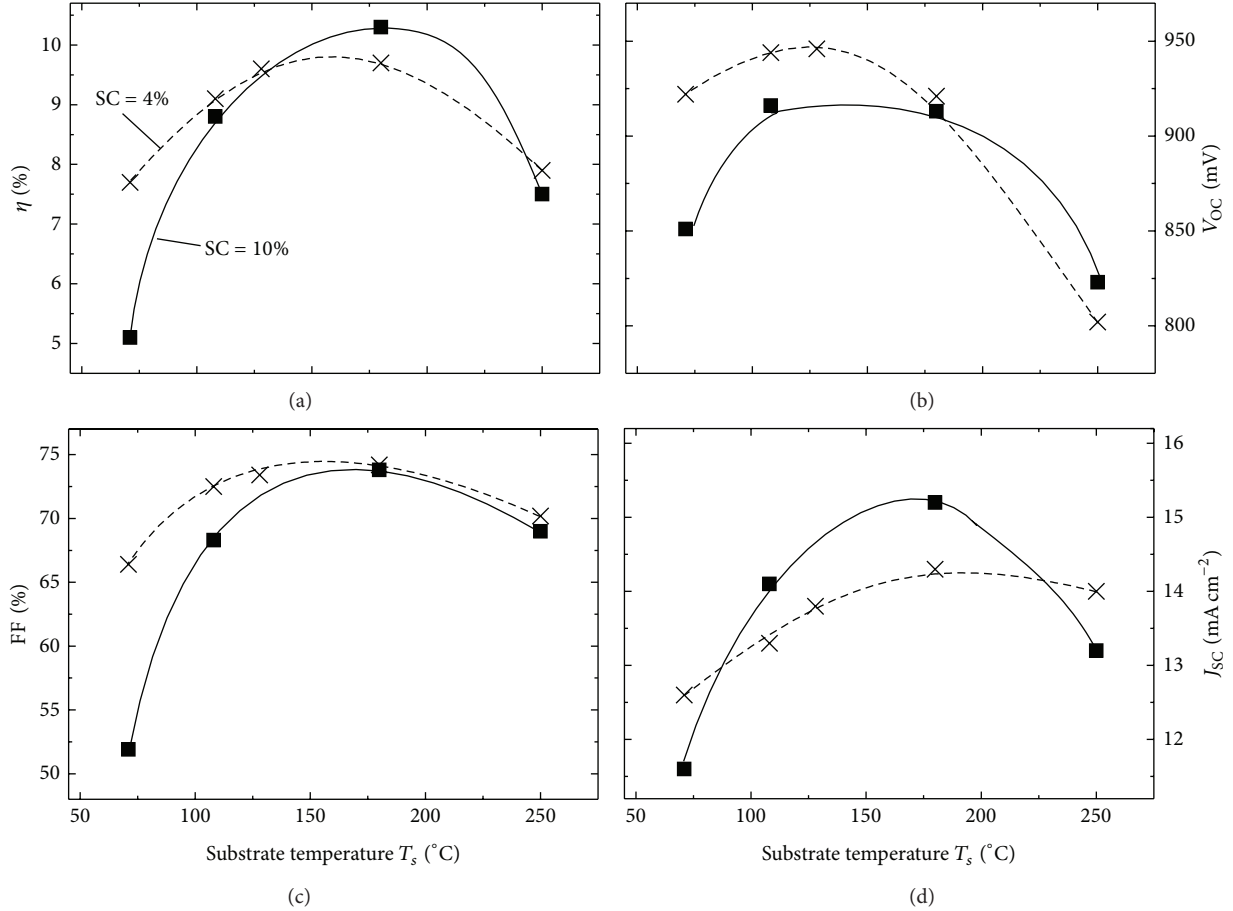


FIGURE 6: Photovoltaic parameters of single junction solar cells (efficiency (a), open-circuit voltage (b), fill factor (c), and short circuit current density (d)) as a function of the substrate temperature of the intrinsic a-Si:H layer, with 10% and 4% silane concentration, respectively. The lines are to guide the eye.

Figure 6(d) presents the J_{SC} data of the solar cell series as a function of T_s . From 70°C to 180°C, J_{SC} increases with increasing T_s and, except for T_s of 70°C, solar cells with SC of 10% promote higher J_{SC} compared to cells with SC of 4%. This can be explained by the wider E_{04} gap of a-Si:H layers with SC of 4%, in comparison to layers with SC of 10% (Figure 3). For T_s of 250°C however, J_{SC} decreases for both SC.

The quantum efficiencies for the solar cell series (the same as in Figure 6) deposited at SC of 4% and 10% at different T_s are shown in Figures 7(a) and 7(b), respectively. In the longer wavelength region the expected increase in QE with increasing T_s (i.e., decreasing E_{04}) is apparent for both SC. The QE in the shorter wavelength region reflects the trend of J_{SC} data shown in Figure 6(d). Thus, the decrease in total J_{SC} for T_s of 250°C (Figure 6(d)) is caused by the drop in current under short wavelength illumination and can be localized to the region of the solar cell where light of short wavelengths is mainly absorbed, that is, the region of the p-doped/intrinsic a-Si:H layer interface. At T_s of 250°C for the deposition of the intrinsic absorber layer, boron diffusion from the p-doped layer (deposited at 180°C) into the intrinsic a-Si:H layer is assisted, leading to a deterioration of the p-/i-interface, which can result in a reduction of the short wavelength QE [39]. In

addition, as can be deduced from Figure 7(a), the QE for T_s of 70°C deteriorates over the entire wavelength range at SC of 10% but can be improved considerably by using a lower SC of 4% during the deposition of the intrinsic a-Si:H layer (Figure 7(b)).

3.2.2. Tandem Junction Solar Cells. Several tandem junction combinations of two a-Si:H single junction solar cells have been realized. The top and bottom cell combinations along with the absorber layer parameters (SC and T_s) and photovoltaic device parameters are listed in Table 1. The bottom cell thickness was 400 nm and the top cell thickness was 110 nm, respectively, for all the tandem junction cells from Table 1.

The data in Table 1 confirms that a broad range of high open-circuit voltages can be achieved, ranging from 1601 mV to 1870 mV. In addition, the V_{OC} values of the tandem solar cells are in good agreement with the summed V_{OC} values of the respective individual subcells, proving a stable process control. To ensure efficient hydrogen production, the a-Si:H/a-Si:H photocathode should preferably provide high photocurrent and operate near its maximum power point (MPP) during photoelectrochemical water splitting. Thus, J_{SC} and V_{MPP} play an important role here. In this regard, the

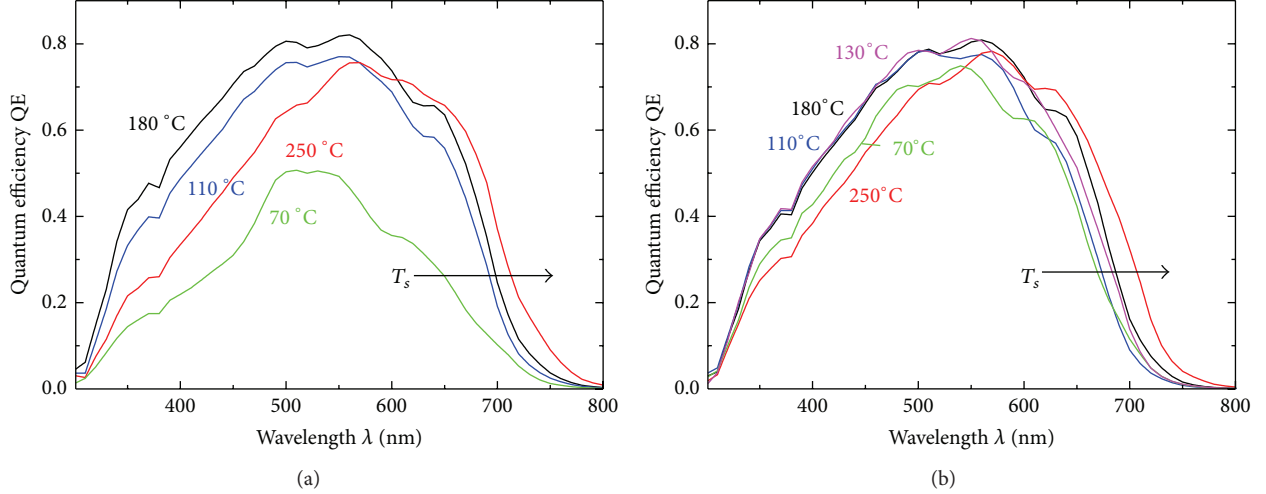


FIGURE 7: Quantum efficiency curves for single junction solar cells at silane concentration of (a) 10% and (b) 4% for different T_s of the absorber layer.

TABLE 1: Photovoltaic parameters of a-Si:H/a-Si:H tandem junction solar cells fabricated with varying SC and T_s of top and bottom cell.

Top cell		Bottom cell		η [%]	V_{OC} [mV]	FF [%]	J_{SC} [mA/cm ²]	V_{MPP} [mV]
SC _{top} [%]	$T_{s,top}$ [°C]	SC _{bot} [%]	$T_{s,bot}$ [°C]					
4	250	4	250	8.3	1602	71.8	7.2	1325
10	180	4	250	8.7	1700	68.5	7.4	1410
4	110	4	110	9.5	1870	77.5	6.6	1580
10	180	10	180	9.8	1796	78.8	7	1555
4	130	10	180	10.5	1816	73.5	7.9	1520
4	130	4	130	9.7	1855	78.2	6.7	1595

best two tandem cells listed in Table 1, with respect to J_{SC} and V_{MPP} , were chosen to be further optimized by means of current matching. The MPP voltage for all tandem cells is presented in the last column of Table 1. The highest V_{MPP} of 1595 mV is achieved by the tandem cell combining two subcells with SC of 4% and both $T_{s,top}$ and $T_{s,bot}$ of 130°C. The tandem cell consisting of a 4% SC top cell with $T_{s,top}$ of 130°C and a 10% SC bottom cell with $T_{s,bot}$ of 180°C exhibits the highest J_{SC} of 7.9 mA/cm² and an η of 10.5%.

In order to match the two subcells, with respect to the current, the thickness of the absorber layer of the top cell d_{top} has been optimized. The two chosen tandem cells were deposited with d_{top} of 70 nm and 90 nm, respectively, and compared with the tandem cell comprising the 110 nm thick top cell. Figure 8 presents the respective photovoltaic parameters as a function of the top cell thickness.

The matching series of the tandem cells with top and bottom absorber layers deposited at different T_s and SC (filled squares in Figure 8) shows that V_{OC} was only marginally affected by a reduced top cell thickness and increased by 15 mV for d_{top} of 110 nm to 70 nm (Figure 8(b)). The J_{SC} decreased with decreasing d_{top} from 7.9 mA/cm² for d_{top} of 110 nm to 6.7 mA/cm² for d_{top} of 70 nm (Figure 8(d)). As current matching should enhance the J_{SC} [40], one can conclude that the tandem cell was better matched at d_{top} of

110 nm and became top cell limited by further reducing d_{top} . The fill factor is expected to decrease when top and bottom cells are matched [39]. This is observed in Figure 8(c) where FF decreased by 4.9% with increasing d_{top} . The highest η of 10.5% was achieved when bottom and top cell are current matched (Figure 8(a)).

In the matching series of the second tandem cell, in which both top and bottom cell were deposited at T_s of 130°C and SC of 4% (open squares in Figure 8), the reduction of d_{top} leads to an increase in J_{SC} of 0.4 mA/cm² from d_{top} of 110 nm to 70 nm (Figure 8(d)). The FF decreased by 2.6% with decreasing d_{top} (Figure 8(c)). The highest V_{OC} of 1871 mV was achieved for the tandem cell with d_{top} of 90 nm (Figure 8(b)), which also exhibits the highest η of 9.9%.

The best two tandem cells, with respect to η , are summarized in Table 2.

3.3. Photoelectrochemical Measurements. The performance of the developed a-Si:H/a-Si:H tandem junction based photocathodes was examined and compared to the photovoltaic performance of the corresponding solar cells. For this purpose, four tandem cells covering up the V_{OC} range from 1600 mV to 1870 mV (from Tables 1 and 2) were chosen and the onset potential for cathodic current (E_{onset}), the potential at maximum power point (E_{MPP}), and the photocurrent density at 0 V versus RHE (J_{RHE}) were determined. Table 3

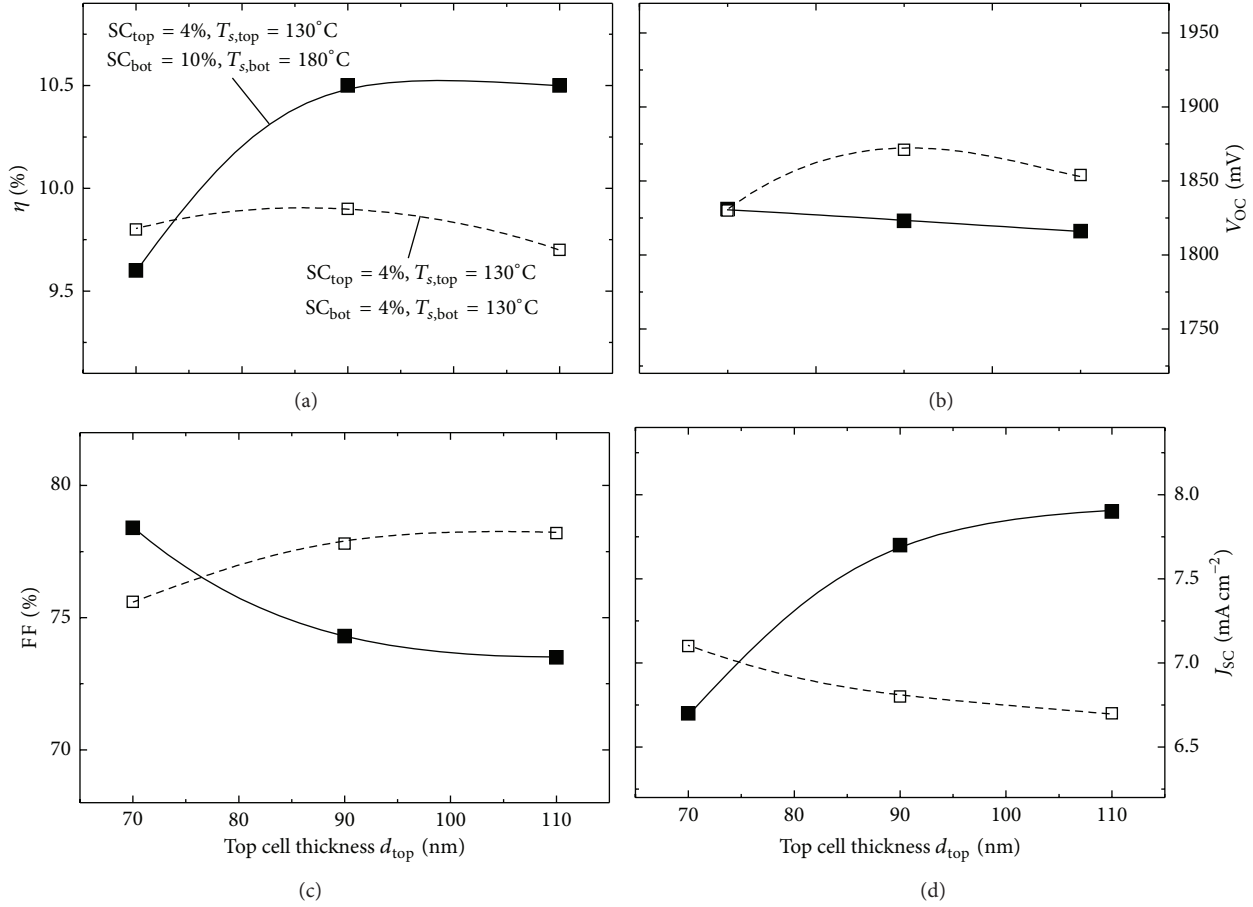


FIGURE 8: Photovoltaic parameters of the current matching series of two tandem junction solar cells deposited at different SC and T_s , as a function of their top cell thickness. The lines are to guide the eye.

TABLE 2: Photovoltaic parameters of a-Si:H/a-Si:H tandem junction solar cells resulting from the current matching series.

Top cell		Bottom cell		η [%]	V_{OC} [mV]	FF [%]	J_{SC} [mA/cm^2]	V_{MPP} [mV]
SC_{top} [%]	$T_{s,top}$ [$^\circ\text{C}$]	SC_{bot} [%]	$T_{s,bot}$ [$^\circ\text{C}$]					
4	130	10	180	10.5	1816	73.5	7.9	1520
4	130	4	130	9.9	1872	77.8	6.8	1600

provides the photovoltaic and PEC device parameters of the respective photocathodes. E_{MPP} and J_{RHE} (from Table 3.) are extracted from cyclic voltammetry (CV) measurements depicted in Figure 9. The measurements were conducted with the four a-Si:H/a-Si:H photocathodes without any further surface or back contact modification.

The disparity in J_{SC} and J_{RHE} values originates from the different illumination source used in photovoltaic and PEC arrangement, respectively. AM 1.5 illumination provides higher light intensities in the wavelength range between 300 nm and 800 nm, where a-Si:H possesses the highest light absorption, compared to the halogen lamp used in the PEC arrangement. Notwithstanding this, photovoltaic and photoelectrochemical performances show the same trends. The higher the V_{MPP} of a photocathode is, the higher its E_{MPP} is. A similar correlation was observed for the current densities J_{SC} and J_{RHE} . This result provides evidence that the

photoelectrochemical performance of the photocathode can be partly deduced from the photovoltaic performance of the solar cell, which is highly important for further development.

Photocathode D exhibits the highest photocurrent density of $6.3 \text{ mA}/\text{cm}^2$ at 0 V versus RHE. E_{MPP} of photocathode D is 1098 mV versus RHE and thus slightly lower than the highest E_{MPP} value of 1127 mV versus RHE and is promoted by photocathode C, which in contrast has a lower J_{RHE} of $5.3 \text{ mA}/\text{cm}^2$. The onset potential of cathodic current was taken as the value at a photocurrent density of $-0.5 \text{ mA}/\text{cm}^2$. Hereby, E_{onset} data (from Table 3) reflects V_{OC} data obtained in photovoltaic arrangement and shifts anodically from photocathodes A and B (1196 mV versus RHE and 1338 mV versus RHE, resp.) to photocathodes D and C (1450 mV versus RHE and 1495 mV versus RHE, resp.). Efficient self-contained solar water splitting requires a photocathode with high photocurrent at a positive potential over 1.23 V versus

TABLE 3: Photovoltaic and PEC parameters of a-Si:H/a-Si:H tandem junction based photocathodes.

Photocathode	η [%]	V_{OC} [mV]	FF [%]	J_{SC} [mA/cm ²]	V_{MPP} [mV]	E_{onset} [mV versus RHE]	E_{MPP} [mV versus RHE]	J_{RHE} [mA/cm ²]
A	8.3	1602	71.8	7.2	1325	1196	832	5.9
B	8.7	1700	68.5	7.4	1410	1338	960	6.1
C	9.9	1872	77.8	6.8	1600	1495	1127	5.3
D	10.5	1816	73.5	7.9	1520	1450	1098	6.3

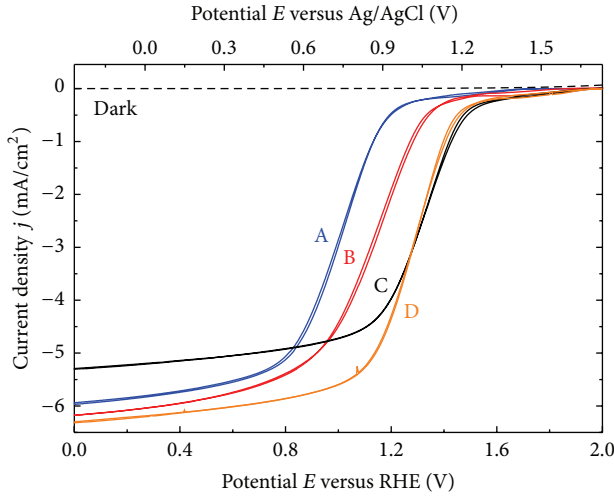


FIGURE 9: Cyclic voltammetry measurement of a-Si:H/a-Si:H photocathodes (listed in Table 3). Measurements were performed in 0.1 M H₂SO₄ solution (pH 1) under 100 mW/cm² illumination intensity at a scan rate of 30 mV s⁻¹. The dark current is shown as a black dashed curve.

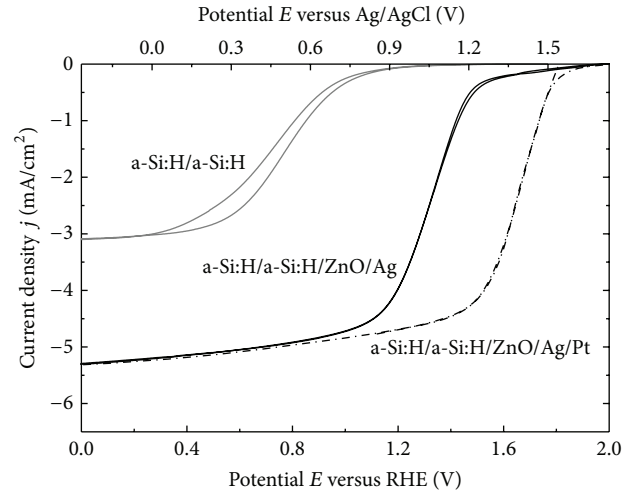


FIGURE 10: Cyclic voltammetry measurement of a-Si:H/a-Si:H photocathodes with no metallic back contact (solid grey curve), with ZnO/Ag back contact (solid black curve, photocathode C from Table 3) and with ZnO/Ag/Pt back contact (dashed curve), in 0.1 M H₂SO₄ solution (pH 1) under 100 mW/cm² illumination intensity at a scan rate of 30 mV s⁻¹.

RHE [13]. Thus, within this study photocathodes C and D are the most suitable candidates for PEC water splitting devices.

To describe the effect of different back contact catalysts, photocathode C was further investigated, as it exhibits the highest E_{onset} . Figure 10 shows the cyclic voltammograms measured for a-Si:H/a-Si:H photocathodes with no metallic back contact (solid grey curve, silicon in contact to the electrolyte), with ZnO/Ag back contact (solid black curve, photocathode C from Table 3) and with ZnO/Ag/Pt back contact (dashed curve). The low photocurrent (3.1 mA/cm² at 0 V versus RHE) of the back contact-free photocathode is caused by optical losses, due to the missing metallic back-reflector. Additionally, the injection of charge carriers into the electrolyte is kinetically limited for metal-free surfaces, resulting in high overpotentials for water reduction [24]. This is confirmed by the significant shift of E_{onset} in negative bias direction (950 mV versus RHE). Unlike the photocathodes with metallic back contacts, forward and reverse scan of the bare a-Si:H/a-Si:H photocathode are shifted, revealing a protective or passivation effect of the metallic back contact [12]. No effect on J_{RHE} is observed when a thin 50 nm layer of platinum is deposited on the ZnO/Ag back contact. Both photocathodes with metallic back contact provide 5.3 mA/cm² at 0 V versus RHE, proving that the optics of the photocathode remains mainly unaffected by the platinum layer.

However, with respect to the ZnO/Ag back contact photocathode, the photocathode with ZnO/Ag/Pt back contact shows a significant shift in E_{onset} in positive bias direction (270 mV) and is measured to be 1765 mV versus RHE. Furthermore, an impressively high E_{MPP} of 1457 mV versus RHE is exhibited by the platinumized photocathode, with a photocurrent density of 4.4 mA/cm², which accentuates both, the excellent catalytic activity of platinum as a catalyst for the hydrogen evolution reaction (HER) and its viable combination with the a-Si:H/a-Si:H/ZnO/Ag tandem device. In fact, the photocurrent density of 4.4 mA/cm² at 1457 mV versus RHE is the highest reported value at such positive potentials for a-Si:H single and tandem solar cell based photoelectrodes [13, 41–43]. Photocathodes, which can provide high photocurrents at more positive potentials, could effectively attenuate the catalytic activity requirement (i.e., reduction of overpotential losses) of the anode in a two-electrode PEC system. Taking additionally into account the nonideal illumination of the a-Si:H/a-Si:H photocathode by the halogen lamp, our result a fortiori demonstrates the capability for a direct application of the developed photocathodes in efficient and self-contained PEC devices. A prior study on amorphous tandem junction solar cell used as photocathode reported E_{onset} values of 1.35 V versus the saturated calomel electrode (SCE) along with a photocurrent

density of 2 mA/cm^2 at 0 V versus SCE [41]. A similar approach led to 1.43 V versus SCE and 3 mA/cm^2 at 0 V versus SCE [42]. Furthermore, this study reported on a tandem junction a-Si:H solar cell deposited on a crystalline silicon wafer. This triple cell concept promoted a high E_{onset} of 1.84 V versus RHE, but a rather low photocurrent density of 2.4 mA/cm^2 . The most recent work focusing on the direct application of a-Si:H solar cells as photoelectrodes was done by Lin et al. [13]. Here, single junction a-Si:H solar cells were tested as photocathodes under the irradiation by a simulated sunlight (AM 1.5 light spectrum, 100 mW/cm^2) and exhibited an E_{onset} of 0.93 V versus RHE and photocurrent densities of 6.1 and 9.4 mA/cm^2 at 0.8 and 0.7 V versus RHE, respectively.

As integrated water splitting devices require chemical-resistant electrodes, stability issues of the silicon solar cells in contact with aqueous solutions need to be addressed and are currently under investigation. Furthermore, light induced degradation plays a major role for a-Si:H based devices and has been extensively investigated [18, 43]. In the present study this was not yet a focus of our work. It should however be noticed that the important parameter V_{OC} is typically the least affected parameter upon prolonged illumination and in some cases even increases [44].

4. Conclusion

We presented the development of a-Si:H/a-Si:H based photocathodes for efficient hydrogen production. By varying the substrate temperature and SiH_4 to total gas-flow concentration during the deposition of intrinsic a-Si:H absorber layers, we demonstrated that, in the case of a-Si:H/a-Si:H tandem cells, the optical and electrical properties of the a-Si:H subcells can be tuned and provide an extended V_{OC} range in tandem devices. It was found that the V_{OC} of tandem solar cells, with efficiencies around 10%, could systematically be adjusted between 1600 mV and 1870 mV .

Furthermore, the performance of the developed tandem junction solar cells as photocathodes was demonstrated in a PEC arrangement. In particular, a-Si:H/a-Si:H photocathodes with ZnO/Ag/Pt back contact exhibited excellent onset potentials over 1760 mV versus RHE with a photocurrent density of 5.3 mA/cm^2 at 0 V versus RHE and thus fulfill the main thermodynamic requirements to generate H_2 . The presented approach exploits a strategy of an efficient and low-cost route to solar hydrogen production based on amorphous thin film silicon tandem junction solar cells at a level which is sufficient for technological use.

Conflict of Interests

The authors declare that there is no conflict of interests regarding the publication of this paper.

Acknowledgments

The authors thank J. Klomfaß, S. Tillmanns, L. Petter, W. Reetz, H. Siekmann, U. Gerhards, O. Thimm, and W. Beyer for their contributions to this work. The research is partly

financially supported by the Deutsche Forschungsgemeinschaft (DFG) Priority Programme 1613: Regeneratively Produced Fuels by Light Driven Water Splitting: Investigation of Involved Elementary Processes and Perspectives of Technologic Implementation and by the Bundesministerium für Bildung und Forschung (BMBF) in the network project: Sustainable Hydrogen (FKZ 03X3581B). J. Ziegler, B. Kaiser, and W. Jaegermann acknowledge partial financial support by the DFG Excellency Graduate School of Energy Science and Engineering (GSC 1070).

References

- [1] N. S. Lewis and D. G. Nocera, "Powering the planet: chemical challenges in solar energy utilization," *Proceedings of the National Academy of Sciences of the United States of America*, vol. 103, no. 43, pp. 15729–15735, 2006.
- [2] J. P. Holdren, "Energy and sustainability," *Science*, vol. 315, no. 5813, p. 737, 2007.
- [3] O. Khaselev and J. A. Turner, "A monolithic photovoltaic-photoelectrochemical device for hydrogen production via water splitting," *Science*, vol. 280, no. 5362, pp. 425–427, 1998.
- [4] T. G. Deutsch, C. A. Koval, and J. A. Turner, "III-V nitride epilayers for photoelectrochemical water splitting: GaPN and GaAsPN," *The Journal of Physical Chemistry B*, vol. 110, no. 50, pp. 25297–25307, 2006.
- [5] A. Heller and R. G. Vadimsky, "Efficient solar to chemical conversion: 12% efficient photoassisted electrolysis in the [p-type InP(Ru)]/HCl-KCl/Pt(Rh) cell," *Physical Review Letters*, vol. 46, no. 17, pp. 1153–1156, 1981.
- [6] J. Ziegler, D. Fertig, B. Kaiser et al., "Preparation and characterization of GaP semiconductor electrodes for photoelectrochemical water splitting," *Energy Procedia*, vol. 22, pp. 108–113, 2012.
- [7] A. Paracchino, V. Laporte, K. Sivula, M. Grätzel, and E. Thimsen, "Highly active oxide photocathode for photoelectrochemical water reduction," *Nature Materials*, vol. 10, no. 6, pp. 456–461, 2011.
- [8] J. Y. Kim, G. Magesh, D. H. Youn et al., "Single-crystalline, wormlike hematite photoanodes for efficient solar water splitting," *Nature*, vol. 3, p. 2681, 2013.
- [9] F. F. Abdi, L. Han, A. H. M. Smets, M. Zeman, B. Dam, and R. van de Krol, "Efficient solar water splitting by enhanced charge separation in a bismuth vanadate-silicon tandem photoelectrode," *Nature Communications*, vol. 4, article 3195, 2013.
- [10] D. V. Esposito, I. Levin, T. P. Moffat, and A. A. Talin, " H_2 evolution at Si-based metal-insulator-semiconductor photoelectrodes enhanced by inversion channel charge collection and H spillover," *Nature Materials*, vol. 12, no. 6, pp. 562–568, 2013.
- [11] J. R. McKone, E. L. Warren, M. J. Bierman et al., "Evaluation of Pt, Ni, and Ni-Mo electrocatalysts for hydrogen evolution on crystalline Si electrodes," *Energy and Environmental Science*, vol. 4, no. 9, pp. 3573–3583, 2011.
- [12] U. Sim, T.-Y. Yang, J. Moon et al., "N-doped monolayer graphene catalyst on silicon photocathode for hydrogen production," *Energy & Environmental Science*, vol. 6, no. 12, pp. 3658–3664, 2013.
- [13] Y. Lin, C. Battaglia, M. Boccard et al., "Amorphous Si thin film based photocathodes with high photovoltage for efficient hydrogen production," *Nano Letters*, vol. 13, no. 11, pp. 5615–5618, 2013.

- [14] L. Han, F. F. Abdi, P. Perez Rodriguez et al., "Optimization of amorphous silicon double junction solar cells for an efficient photoelectrochemical water splitting device based on a bismuth vanadate photoanode," *Physical Chemistry Chemical Physics*, vol. 16, no. 9, pp. 4220–4229, 2014.
- [15] S. Y. Reece, J. A. Hamel, K. Sung et al., "Wireless solar water splitting using silicon-based semiconductors and earth-abundant catalysts," *Science*, vol. 334, no. 6056, pp. 645–648, 2011.
- [16] E. L. Miller, R. E. Rocheleau, and S. Khan, "A hybrid multijunction photoelectrode for hydrogen production fabricated with amorphous silicon/germanium and iron oxide thin films," *International Journal of Hydrogen Energy*, vol. 29, no. 9, pp. 907–914, 2004.
- [17] A. Shah, *Thin-Film Silicon Solar Cells, Photovoltaics and Large-Area Electronics*, CRC Press, 2008.
- [18] B. Rech and H. Wagner, "Potential of amorphous silicon for solar cells," *Applied Physics A*, vol. 69, no. 2, pp. 155–167, 1999.
- [19] J. R. Bolton, S. J. Strickler, and J. S. Connolly, "Limiting and realizable efficiencies of solar photolysis of water," *Nature*, vol. 316, no. 6028, pp. 495–500, 1985.
- [20] M. F. Weber and M. J. Dignam, "Splitting water with semiconducting photoelectrodes—efficiency considerations," *International Journal of Hydrogen Energy*, vol. 11, no. 4, pp. 225–232, 1986.
- [21] A. J. Nozik, "Photoelectrochemistry: applications to solar energy conversion," *Annual Review of Physical Chemistry*, vol. 29, pp. 189–222, 1978.
- [22] L. Ley, "Photoemission and optical properties," *Topics in Applied Physics*, vol. 56, pp. 61–168, 2005.
- [23] W. Beyer and H. Wagner, "The role of hydrogen in a-Si:H—results of evolution and annealing studies," *Journal of Non-Crystalline Solids*, vol. 59–60, no. 1, pp. 161–168, 1983.
- [24] M. G. Walter, E. L. Warren, J. R. McKone et al., "Solar water splitting cells," *Chemical Reviews*, vol. 110, no. 11, pp. 6446–6473, 2010.
- [25] R. van de Krol and M. Grätzel, *Photoelectrochemical Hydrogen Production*, Springer, New York, NY, USA, 2012.
- [26] D. E. Carlson and C. R. Wronski, "Amorphous silicon solar cell," *Applied Physics Letters*, vol. 28, no. 11, pp. 671–673, 1976.
- [27] S. Guha, J. Yang, P. Nath, and M. Hack, "Enhancement of open circuit voltage in high efficiency amorphous silicon alloy solar cells," *Applied Physics Letters*, vol. 49, no. 4, pp. 218–219, 1986.
- [28] W. Böttler, V. Smirnov, J. Hüpkens, and F. Finger, "Texture-etched ZnO as a versatile base for optical back reflectors with well-designed surface morphologies for application in thin film solar cells," *Physica Status Solidi (A)*, vol. 209, no. 6, pp. 1144–1149, 2012.
- [29] N. Wyrsh, F. Finger, T. J. McMahon, and M. Vanecek, "How to reach more precise interpretation of subgap absorption spectra in terms of deep defect density in a-Si:H," *Journal of Non-Crystalline Solids*, vol. 137–138, part 1, pp. 347–350, 1991.
- [30] G. Hodes, "Photoelectrochemical cell measurements: getting the basics right," *Journal of Physical Chemistry Letters*, vol. 3, no. 9, pp. 1208–1213, 2012.
- [31] G. Ganguly and A. Matsuda, "Importance of surface processes in defect formation in a-Si:H," *Journal of Non-Crystalline Solids*, vol. 164–166, part 1, pp. 31–36, 1993.
- [32] R. A. Street, *Hydrogenated Amorphous Silicon*, Cambridge Solid State Science Series, Cambridge University Press, Cambridge, UK, 1991.
- [33] Y. Ashida, "Conference record of the 24th IEEE photovoltaic specialists conference," in *Proceedings of the IEEE 1st World Conference on Photovoltaic Energy Conversion*, vol. 1-2, 1994.
- [34] A. Matsuda, *Tetrahedrally Bonded Amorphous Semiconductors*, pp. 192–196, American Institute of Physics, 1981.
- [35] A. H. M. Smets, W. M. M. Kessels, and M. C. M. van de Sanden, "Vacancies and voids in hydrogenated amorphous silicon," *Applied Physics Letters*, vol. 82, no. 10, pp. 1547–1549, 2003.
- [36] A. H. M. Smets and M. C. M. van de Sanden, "Relation of the Si-H stretching frequency to the nanostructural Si-H bulk environment," *Physical Review B*, vol. 76, no. 7, Article ID 073202, 2007.
- [37] V. Smirnov, O. Astakhov, R. Carius, Y. Petrusenko, V. Borysenko, and F. Finger, "Variation in absorber layer defect density in amorphous and microcrystalline silicon thin film solar cells with 2MeV electron bombardment," *Japanese Journal of Applied Physics*, vol. 51, no. 2, Article ID 022301, 2012.
- [38] V. Smirnov, O. Astakhov, R. Carius et al., "Performance of p- and n-side illuminated microcrystalline silicon solar cells following 2 MeV electron bombardment," *Applied Physics Letters*, vol. 101, Article ID 143903, 2012.
- [39] S. Nakano, "High absorption-coefficient and stable a-Si for high-efficiency solar cells," in *Proceedings of the Conference Record of the 21st IEEE Photovoltaic Specialists Conference*, vol. 2, pp. 1656–1661, Kissimmee, Fla, USA, 1990.
- [40] W. E. McMahon, K. E. Emery, D. J. Friedman et al., "Fill factor as a probe of current-matching for GaInP₂/GaAs tandem cells in a concentrator system during outdoor operation," *Progress in Photovoltaics: Research and Applications*, vol. 16, no. 3, pp. 213–224, 2008.
- [41] M. Matsumura, Y. Sakai, S. Sugahara, Y. Nakato, and H. Tsubomura, "Photoelectrochemical hydrogen evolution using amorphous silicon electrodes having p-i-n or p-i-n-p-i-n junctions," *Solar Energy Materials*, vol. 13, no. 1, pp. 57–64, 1986.
- [42] Y. Sakai, S. Sugahara, M. Matsumura, Y. Nakato, and H. Tsubomura, "Photoelectrochemical water splitting by tandem type and heterojunction amorphous silicon electrodes," *Canadian Journal of Chemistry*, vol. 66, no. 8, pp. 1853–1856, 1988.
- [43] D. L. Staebler and C. R. Wronski, "Reversible conductivity changes in discharge-produced amorphous Si," *Applied Physics Letters*, vol. 31, no. 4, pp. 292–294, 1977.
- [44] V. Smirnov, A. Lambertz, S. Tillmanns, and F. Finger, "p- and n-type microcrystalline silicon oxide ($\mu\text{-SiO}_x\text{:H}$) for applications in thin film silicon tandem solar cells," *Canadian Journal of Physics*, vol. 92, pp. 932–935, 2014.